LEABHARLANN CHOLÁISTE NA TRÍONÓIDE, BAILE ÁTHA CLIATH | TRINITY COLLEGE LIBRARY DUBLIN
Ollscoil Átha Cliath | The University of Dublin

Terms and Conditions of Use of Digitised Theses from Trinity College Library Dublin

Copyright statement

All material supplied by Trinity College Library is protected by copyright (under the Copyright and Related Rights Act, 2000 as amended) and other relevant Intellectual Property Rights. By accessing and using a Digitised Thesis from Trinity College Library you acknowledge that all Intellectual Property Rights in any Works supplied are the sole and exclusive property of the copyright and/or other IPR holder. Specific copyright holders may not be explicitly identified. Use of materials from other sources within a thesis should not be construed as a claim over them.

A non-exclusive, non-transferable licence is hereby granted to those using or reproducing, in whole or in part, the material for valid purposes, providing the copyright owners are acknowledged using the normal conventions. Where specific permission to use material is required, this is identified and such permission must be sought from the copyright holder or agency cited.

Liability statement

By using a Digitised Thesis, I accept that Trinity College Dublin bears no legal responsibility for the accuracy, legality or comprehensiveness of materials contained within the thesis, and that Trinity College Dublin accepts no liability for indirect, consequential, or incidental, damages or losses arising from use of the thesis for whatever reason. Information located in a thesis may be subject to specific use constraints, details of which may not be explicitly described. It is the responsibility of potential and actual users to be aware of such constraints and to abide by them. By making use of material from a digitised thesis, you accept these copyright and disclaimer provisions. Where it is brought to the attention of Trinity College Library that there may be a breach of copyright or other restraint, it is the policy to withdraw or take down access to a thesis while the issue is being resolved.

Access Agreement

By using a Digitised Thesis from Trinity College Library you are bound by the following Terms & Conditions. Please read them carefully.

I have read and I understand the following statement: All material supplied via a Digitised Thesis from Trinity College Library is protected by copyright and other intellectual property rights, and duplication or sale of all or part of any of a thesis is not permitted, except that material may be duplicated by you for your research use or for educational purposes in electronic or print form providing the copyright owners are acknowledged using the normal conventions. You must obtain permission for any other use. Electronic or print copies may not be offered, whether for sale or otherwise to anyone. This copy has been supplied on the understanding that it is copyright material and that no quotation from the thesis may be published without proper acknowledgement.

volcano flank terraces

ON MARS

PAUL K. **BYRNE**

a dissertation submitted in partial fulfilment for the degree of Doctor of Philosophy to the University of Dublin, Trinity College

MMX

TRINITY COLLEGE
10 APR 2012
LIBRARY DUBLIN
9467

I declare that

- this thesis has not been submitted as an exercise for a degree at this or any other University;
- this is entirely my own work, except where otherwise duly acknowledged in the text; and
- I agree that the Library may lend or copy the thesis upon request.

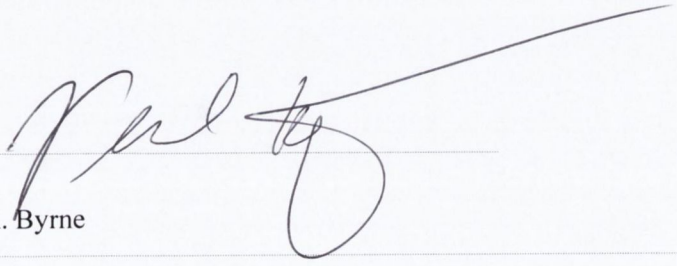

Paul K. Byrne

Flank terraces are topographically subtle, laterally extensive structures on the flanks of several large shield volcanoes on Mars. The formation of terraces has been ascribed to several mechanisms, including elastic self-loading, lithospheric flexure, gravitational spreading, magma chamber tumescence, and shallow slumping. The geometry of these structures, in terms of morphology and distribution, is poorly understood. In turn, proposed formation mechanisms have not been investigated fully. Therefore, flank terraces have yet to be integrated into the current framework of Martian volcanotectonism.

Using a combination of photogeological mapping and scaled analogue modelling techniques, this study aims to:

- characterise the nature of flank terraces
- determine the origin of these elusive structures
- establish a structural context for terraces within Martian volcano evolution

Each of these aims is addressed in a separate, self-contained chapter, with its own methodology, summary of results, discussion, and concluding remarks. These core chapters are preceded by an introductory chapter, and succeeded by an overview of the thesis as a whole and a brief set of conclusions.

nature

In the first core chapter, the nature of volcano flank terraces on Mars is characterised by three-dimensional Mars Orbiter Laser Altimeter (MOLA) topography. At least nine volcanoes on Mars are terraced — Alba Patera, Albor Tholus, Arsia Mons, Ascraeus Mons, Elysium Mons, Hecates Tholus, Olympus Mons, Pavonis Mons, and Uranius Patera — far exceeding the number reported in existing literature. Moreover, Shuttle Radar Topography Mission (SRTM) data indicate at least three terraced volcanoes on Earth: Etna (Sicily), Mauna Loa (Hawaii), and Tendürek Dagi (Turkey).

Flank terraces have a convex-upward profile in cross-section, consistent with thrust fault morphology. As convex-outward structures in plan view, they form an imbricate, "fish-scale" pattern upon each terraced volcano. Terraces are scale-invariant structures, as they are systematically expressed across a range of geometric sizes. Certain terrace parameters show a similar relationship to corresponding values for thrust faults on Earth. The geometry of flank terraces does not agree with that predicted by any extensional process, nor by magma chamber inflation or elastic self-loading. Terraces, however, may be the outward-verging structures predicted to form as a volcano's upper flanks are shortened due to flexure of the supporting lithosphere. This hypothesis serves as the focus of the second core chapter.

origin

The origin of terraces is determined by a suite of laboratory flexure experiments, using ~10^4 Pa s viscoelastic silicone gel as an analogue to the viscoelastic crust on Mars, and fine quartzose sand to simulate volcanic material. The experiments feature conical loads of sand passively sinking into deep silicone reservoirs, and examine a range of experimental parameters including cone volume, geometry, and internal layering, sand cohesion, and the presence of a brittle layer between the cone and underlying ductile layer.

Each experimental series produces the same set of characteristic features. An array of convex-upward, convex-outward structures develops on the cone flanks, arranged in an imbricate pattern about the load. A shallow, concentric trough develops at the base of the cone, accompanied by an outer zone of circumferential tension fracturing. Measured deformation indicates that the upper surface of each cone experiences a radial and concentric shortening in response to flexure, with principal stress axes orientations of σ_1 radial, σ_2 concentric, and σ_3 vertical. The convexities observed on the slopes of the model cones may correspond to flank terraces, with the annular features similar to structures surrounding several of the Tharsis volcanoes. This premise is examined further in the third core chapter.

context

A structural context for flank terraces is established in the third core chapter using High Resolution Stereo Camera (HRSC) and Context Imager (CTX) data to understanding how terraces spatially and temporally relate to other volcanotectonic features on a case study volcano, Ascraeus Mons. Ascraeus is replete with clearly visible, well-defined surface structures whose origins are well-documented, including pit craters, arcuate graben, and a summit caldera complex.

Photogeological mapping shows that terraces formed throughout most of the volcano's main shield-building phase, but likely predate large rift aprons to the NE and SW. There is evidence that flexure-induced compression of the upper edifice may have ultimately shut off magma supply to the summit, causing volcanism to switch to the lower flanks instead. Some terrace-bounding faults may also have influenced the location of subsequent structures, acting as lineaments and conduits along which a number of pit craters, troughs, and sinuous rilles formed. The formation of flank terraces due to lithospheric flexure is compatible with the provenance of other surface structures on Ascraeus Mons, suggesting that flexure has occurred, and indeed has played a dominant role in shaping the volcano.

These findings enhance the existing framework of Martian volcanotectonism, and provide a basis for understanding the developmental histories of other terraced volcanoes on Mars and beyond.

The contents of Chapters 1 and 2 have previously been published as:

- Byrne, P. K., van Wyk de Vries, B., Murray, J. B., Troll, V. R. (2009) The geometry of volcano flank terraces on Mars. *Earth and Planetary Science Letters* 281, 1-13.

A modified version of Chapter 4 has been submitted for publication, and is in review, as:

- Byrne, P. K., van Wyk de Vries, B., Murray, J. B., Troll, V. R. A volcanotectonic survey of Ascraeus Mons. *Journal of Geophysical Research—Planets.*

Whilst my co-authors assisted in the general preparation of these manuscripts, B. van Wyk de Vries contributed written material which has been directly integrated into this work, and which I duly acknowledge:

- the basis for the structural overviews of the three Terran volcanoes in Chapter 2 (sections 4.4.1, 4.4.2, and 4.4.3, pages 23, 24, and 25)
- elements of the scaling section provided for the laboratory experiments in Chapter 3 (section 2.3, page 36)
- parts of the observations of the summit caldera complex of Ascraeus Mons in Chapter 4 (section 3.1.1, page 59)

Additionally, E. Holohan provided text which helped inform the layout of the kinematic synthesis presented in Chapter 3 (section 4.3, page 46).

Other than these sections, the text in this work is entirely my own; except where otherwise stated, so too are the figures.

I owe an enormous debt of gratitude to my four thesis supervisors, without whose advice, time, and understanding this project would not have been possible. Prof. Benjamin van Wyk de Vries of Blaise Pascal Université has been an unwavering source of encouragement, motivation, insight, support (moral and financial), and, occasionally, whiskey. I have learned an enormous amount from him over the four years I have worked with him, and am a better scientist for it.

Prof. Valentin Troll, formerly of Trinity College Dublin and now at Uppsala, has been a source of inspiration since my first analogue modelling project with him in Dublin in 2003. He has been an unfailing help throughout the project, from its inception through to the predictable last-minute corrections, providing both scientific and logistical aid when needed. He too has taught me much, from the science of volcanotectonism to the art of Tsun Tzu.

Dr. John Murray has proven an ever-generous host upon my visits to his group at the Open University, and a capable guide when hunting for terraces on Etna. His help in securing HRSC data early in the project made a great many aspects of this project feasible. Finally, Dr. Ian Sanders of Trinity College has performed admirably as a surrogate supervisor, consistently finding time to help address the plethora of issues that inevitably develop towards the end of a PhD project.

A special word of thanks must go to Dr. Eoghan Holohan, this project's "Fifth Beatle". Eoghan has served as mentor, sounding board, colleague, and good friend since our first collaboration several years ago. He has remarkable patience and understanding, and has on many occasions selflessly invested more time in this student than in his own work. I hope our collaboration continues.

I thank Dr. Thomas Walter for his hospitality during my stay at GFZ Potsdam, and his help in understanding the powerful tool that is Particle Image Velocimetry. Dr. Matt Balme is thanked for his GIS mentoring and willingness to assist my efforts no matter his workload; he and his wife Anne are also wonderful hosts. Jake Bleacher and Brent Garry are thanked for introducing me to the Outpost bar at LPSC, and for their assistance and photogeological expertise during my work on Ascraeus Mons

Throughout this project I have benefited from the advice and suggestions of a great many experts in planetary science, including Drs. B. Cailleau, L. Crumpler, P. McGovern, L. Montési, J. Morgan, J. Plescia, S. Solomon, D. Williams, and D. Wyrick, and I thank them. Thanks also to Prof. J.-P. Muller and Dr. J.-R. Kim for their help in HRC data processing, and to Dr. E. Hauber and Dr. K. Gwinner for stimulating and informative discussions on mapping techniques and datasets. J. Byrne, P. Dunne, and B. Durcan are thanks for their assistance with my automatic terrace detection efforts. The comments of four anonymous reviewers, and Dr. T. Spohn in an editorial capacity, have greatly improved the quality of science in this work. Sincere thanks go to Dr. J. Walsh of the Fault Analysis Group, University College Dublin, for his help and generosity, and his efforts to correct some of my more wayward structural concepts.

I would particularly like to thank Dr. P. McGovern for acting as External Examiner for this thesis, a role that required a temporally short yet spatially long sojourn from sunny Houston to rainy Dublin, and which I enormously appreciate. Thank you, too, to Dr. Q. Crowley for his conscientious performance as Internal Examiner, and to Prof. G. Clayton for acting as Chair for my *viva voce* examination.

Several key personal in Trinity have supplied logistical support over the project's duration, including D. Burke, N. Kearney, M. Morgan, N. McGinley, and Dr. M. Duncan, for which they are thanked. Dr. J. Graham has provided the means for much of this project to proceed, and I thank him accordingly. I also thank the Trinity College Department of Geology, as well as the Trinity Trust, Graduate Studies Office, Enterprise Ireland (grant no. IC/2006/37/1138), the Owen Sheehy Skeffington Find (no. A113), the Lunar and Planetary Institute, and the American Geophysical Union for financial aid throughout this project.

On a personal note, I wish to thank Eleanor Donohue and Rachel Walters, the ladies of the NRDC office, who have been appreciably patient with my quirks and strange working habits, and who have provided good chocolate and even better conversations. Saskia van Manen and Kim Martelli are thanked for their always enjoyable company in Milton Keynes and Clermont Ferrand, respectively. My thanks go also to Sam O'Mahony-Adams (of SyFy fame), Patrick Gillen, and Heather Bryan for their hospitality abroad, whilst closer to home I appreciate the understanding of my Vitruvius band mates (find us on Facebook), Eoin Madsen and Richard Mullen.

I thank my siblings, David and Alex, and particularly my parents, Linda and Kevin, for their support and understanding over the lifetime of this project. My grandmother Gillen has also played the role of benefactor for my travel and studies, for which I am very grateful.

Finally, my most heartfelt thanks go to Aoife O'Halloran for her steadfast love, understanding, and sense of humour through this entire project, even as she is on a similar enterprise. Aoife has time and again unselfishly made herself available at a moment's notice to provide a level of support and care that I will be forever grateful for. I'm privileged to know her, and I'll be her wingman any day.

introduction 1

overview **3**

1. volcano flank terraces **4**

1.1 proposed formation mechanisms 4

2. this study **5**

2.1 rationale 5

2.2 approach 6

2.3 thesis overview 6

2.3.1 chapter 2 | nature 7

2.3.2 chapter 3 | origin 7

2.3.3 chapter 4 | context 7

2.4 nomenclature 8

nature 9

overview **11**

1. volcanoes in this study **11**

1.1 Tharsis volcanic province 11

1.1.1 Alba Patera 12

1.1.2 Arsia Mons 12

1.1.3 Ascraeus Mons 13

1.1.4 Olympus Mons 13

1.1.5 Pavonis Mons 14

1.1.6 Uranius Patera 15

1.2 Elysium volcanic province 15

1.2.1 Albor Tholus 15

1.2.2 Elysium Mons 16

1.2.3 Hecates Tholus 16

2. methodology **16**

2.1 DTM properties and preparation 17

2.2 terrace definition 17

2.3 DTM measurements 17

2.4 alternative methodology 18

3. results **19**

3.1 visibility 19

3.2 morphology 19

3.3 distribution 19

3.4 morphometric data 20

4. discussion **20**

4.1 timing 20

4.2 morphology 20

4.3 distribution 21

4.4 terraces on Earth 22
4.4.1 Etna 23
4.4.2 Mauna Loa 24
4.4.3 Tendürek Dagi 25
4.4.4 Morphometry 25
4.5 formation mechanisms of flank terraces 25
4.5.1 extensional mechanisms 26
4.5.2 compressional mechanisms 26
4.5.3 applicability to Mars and Earth 29
5. concluding remarks **29**

origin 31
o v e r v i e w **33**
1. lithospheric flexure **33**
2. methodology **34**
2.1 analogue materials 35
2.2 experimental procedure 36
2.3 scaling 36
2.4 qualitative experimental programme (QlX.) 37
2.4.1 set A: simple loading 38
2.4.2 set B: silicone inclusions 38
2.4.3 set C: cone geometry 38
2.4.4 set D: sand layer thickness 38
2.4.5 set E: plaster layer thickness 39
2.4.6 set F: basal décollement 39
2.5 quantitative experimental programme (QnX.) 39
3. results **40**
3.1 qualitative experimental programme results 40
3.1.1 set A: simple loading 40
3.1.2 set B: silicone inclusions 41
3.1.3 set C: cone geometry 41
3.1.4 set D: sand layer thickness 42
3.1.5 set E: plaster layer thickness 42
3.1.6 set F: basal décollement 43
3.2 quantitative experimental programme results 43
4. discussion **44**
4.1 simple loading and related structures 44
4.2 the effect of parameter variations 44
4.2.1 silicone inclusions 44
4.2.2 cone geometries 45
4.2.3 sand layer thicknesses 45

4.2.4 plaster layer thicknesses 45
4.2.5 basal décollement 45
4.3 kinematic synthesis 46
4.4 comparison with natural examples 47
4.4.1 flank terraces 48
4.4.2 flexural trough 48
4.4.3 concentric graben 49
4.4.4 basal scarp 49
5. concluding remarks **50**

context 53
o v e r v i e w **55**
1. Ascraeus Mons **55**
1.1 structural summary 55
2. methodology **57**
2.1 dataset properties and preparation 57
2.2 mapping 58
3. observations **58**
3.1 eruptive structures 59
3.1.1 caldera complex 59
3.1.2 sinuous rilles 60
3.1.3 lava textures 60
3.1.4 pitted terrain 61
3.1.5 vents 61
3.2 tensional structures 61
3.2.1 pit craters 61
3.2.2 SW embayment graben 62
3.2.3 NW plains graben 63
3.3 compressional structures 63
3.3.1 flank terraces 63
3.3.2 S flank thrust 63
4. discussion **64**
4.1 eruptive structures and processes 64
4.2 tensional volcanotectonism 66
4.3 compressional volcanotectonism 67
4.4 structural synthesis 68
4.4.1 initial shield building 69
4.4.2 onset of flexure 69
4.4.3 late-stage summit activity 70
4.4.4 rift apron construction 70
4.4.5 summit subsidence and surface extension 71

4.5 applicability beyond Ascraeus Mons 72
5. concluding remarks **73**

conclusions 75
o v e r v i e w 77
1. thesis summary 77
1.1 what is the geometry of flank terraces? 77
1.2 what is the causal mechanism of terrace formation? 78
1.3 what is the role of terraces within Martian volcano evolution? 78
2. limitations of the methods used 78
2.1 photogeology 78
2.2 analogue modelling 79
3. suggested further work 79
3.1 photogeology 79
3.2 analogue modelling 79

references cited 81

DVD
appendix I — terrace morphometry data
appendix I.I — Martian terrace data
appendix I.II — Terran terrace data
appendix II — experimental programmes
appendix II.I — QIX. experimental programme
appendix II.II — QnX. experimental programme

introduction

Plate 1.1. Viking images of flank terraces
Plate 1.2. Sketch maps of terraces on Olympus Mons

nature

Plate 2.1. MOLA hillshade of the Tharsis volcanic province
Plate 2.2. MOLA hillshade of the Elysium volcanic province
Plate 2.3. MOLA slope map of Olympus Mons
Plate 2.4. Schematic diagram of terrace parameters
Plate 2.5. Automatic terrace detection example
Plate 2.6. Cross-section of terrace morphology
Plate 2.7. The distribution of flank terraces on Alba Patera
Plate 2.8. The distribution of flank terraces on Albor Tholus
Plate 2.9. The distribution of flank terraces on Arsia Mons
Plate 2.10. The distribution of flank terraces on Ascraeus Mons
Plate 2.11. The distribution of flank terraces on Elysium Mons
Plate 2.12. The distribution of flank terraces on Hecates Tholus
Plate 2.13. The distribution of flank terraces on Olympus Mons
Plate 2.14. The distribution of flank terraces on Pavonis Mons
Plate 2.15. The distribution of flank terraces on Uranius Patera
Plate 2.16. Analysis of key terrace morphometric data
Plate 2.17. The distribution of flank terraces on Etna (Sicily)
Plate 2.18. Terrace-like structure on the SW flank of Etna
Plate 2.19. The distribution of flank terraces on Mauna Loa (Hawaii)
Plate 2.20. Ribbon-like flows on the NW flank of Mauna Loa
Plate 2.21. Photograph of Tendürek Dagi stratovolcano
Plate 2.22. The distribution of flank terraces on Tendürek Dagi (Turkey)
Plate 2.23. The geometry of proposed structures

origin

Plate 3.1. Cartoon illustration of lithospheric flexure
Plate 3.2 Schematic of the simple loading setup
Plate 3.3 Variations in the experimental setup
Plate 3.4 QIX. set A: simple loading results
Plate 3.5 QIX set B: silicone inclusions
Plate 3.6 QIX set C: cone geometry
Plate 3.7 QIX set D: sand layer thickness
Plate 3.8 QIX set E: plaster layer thickness
Plate 3.9 QIX set F: basal décollement
Plate 3.10 Kinematic synthesis cartoon
Plate 3.11 Geometric similarity between terraces

Plate 3.12 Arcuate features around several volcanoes
Plate 3.13 Morphological similarity between Olympus Mons and experiment
Plate 3.14 Comparison of pancake dome morphology and experiment

context

Plate 4.1 MOLA hillshade of Ascraeus Mons
Plate 4.2 Principal surface structures on Ascraeus Mons
Plate 4.3 HRSC and CTX Photomosaic
Plate 4.4 All structures mapped on Ascraeus Mons
Plate 4.5 HRSC summit caldera mosaic and sketch
Plate 4.6 Sinuous rille image and sketch
Plate 4.7 Contrasting flank terrace surface texture
Plate 4.8 Pitted terrain on the SW embayment
Plate 4.9 Parasitic vent image and sketch
Plate 4.10 Pit crater structures image and sketch
Plate 4.11 NW-trending graben image and sketch
Plate 4.12 Load-concentric graben image and sketch
Plate 4.13 Terrace boundary image and sketch
Plate 4.14 S flank thrust system image and sketch

nature

Table 2.1. Morphometric data for the Martian study volcanoes
Table 2.2. Terrace morphometric data for the Martian volcanoes
Table 2.3. Terrace morphometric data for the Terran volcanoes

origin

Table 3.1. Scaling parameters
Table 3.2. Qualitative experimental programme
Table 3.3. Quantitative experimental programme
Table 3.4. Measurements taken in the QnX. set
Table 3.5. Experimental results for QIX. set A
Table 3.6. Experimental results for QIX. set B
Table 3.7. Experimental results for QIX. set C
Table 3.8. Experimental results for QIX. set D
Table 3.9. Experimental results for QIX. set E
Table 3.10. Experimental results for QIX. set F
Table 3.11. Experimental results from QnX.

context

Table 4.1. HRSC and CTX image properties

For I dipt into the future, far as human eye could see;
Saw the Vision of the world, and all the wonder that would be.

Alfred Lord Tennyson

introduction

nature | origin | context

conclusions

overview

The Red Planet has long fascinated humankind. Its crimson colour, changes in brightness, and apparently aberrant behaviour in the night sky suggested an erratic, malevolent celestial deity. The Babylonians named it Nergal after their god of fire and destruction, the Chinese called it the "fire star", and the Romans gave the planet its enduring name in honour of their war god, Mars.

The invention of the telescope in 1608 enabled first Galileo and then a host of later astronomers to investigate Mars, culminating in the 1870s with the famous Schiaparelli maps which detailed long channels across the surface of the planet. Subsequent observations led Lowell to propose that life once existed on Mars, and although continued examination suggested otherwise, interest in the planet continued to grow, stimulating a wealth of work both scientific and literary — H. G. Wells' *War of the Worlds* being a notable contribution.

Exploration of Mars from space began in earnest with NASA's Mariner 4 mission which, in 1965, returned the first remotely-sensed images of the planet [*Leighton et al.*, 1965]. The highly successful Mariner 9 mission in 1971 was the first to orbit the planet, and over the course of a year photographed 85% of the Martian surface [*Masursky et al.*, 1972]. This mission was one of superlatives: amongst its chief accomplishments were the discoveries of the largest canyon network [*Masson et al.*, 1977] and the biggest volcanoes [*Masursky*, 1974] in the known Solar System. Data returned from its camera also allowed the production of the first planet-wide geological map of Mars, as well as the establishment of the Noachian-Hesperian-Amazonian Martian time-stratigraphic system [*Scott and Carr*, 1978]. Moreover, Mariner 9 data provided evidence of fluvial channels on Mars, hinting at a varied climatic history for a planet then thought to be long-inert [*Carr*, 1974].

Later NASA missions provided further information on the volcanoes of Mars. The Viking orbiters that circled the planet in 1976 imaged the planet surface in unprecedented detail. The use of high-resolution Viking data led to the detection of a much greater number of edifices than the 20 mapped by Mariner 9 [*Greeley et al.*, 1977] as well as the recognition of a range of volcanic products across Mars [*Carr et al.*, 1977], and a model for the eruptive histories of the Tharsis Montes [*Crumpler and Aubele*, 1978]. The 1996 Mars Global Surveyor mission returned data that was used to compose a three-dimensional Digital Topographic Model (DTM) of the entire surface of Mars [*Albee et al.*, 2001; *Smith et al.*, 2001], delivering detailed, quantitative data on the morphometry of Martian volcanoes for the first time [*Plescia*, 2004]. Missions launched since 2001 have continued to supply invaluable volcanological data for Mars: the Mars Odyssey and Mars Reconnaissance Orbiter missions have placed constraints on the dynamics of lava flow emplacements [*Mouginis-Mark and Christensen*, 2005; *Mouginis-Mark and Rowland*, 2008], and

Elements of this chapter have previously been published as introductory material in Byrne, P. K., van Wyk de Vries, B., Murray, J. B., Troll, V. R. (2009) The geometry of volcano flank terraces on Mars. *Earth and Planetary Science Letters* 281, 1-13.

the ESA's Mars Express spacecraft has helped define a previously unrecognised volcanic province surrounding the Hellas Impact Basin [*Williams et al.*, 2007].

Thus, space-borne observation of Mars has facilitated a much greater understanding of the nature and history of Martian volcanism, mantle dynamics, and the thermal evolution of the planet than was possible from Earth-based examination alone. Nonetheless, whilst many volcanic structures on Mars have been described and their formation processes understood through comparison with similar features on Earth [*Wilson and Head*, 1994; *Bleacher et al.*, 2007], an enigmatic set of structures remains for which no analogue has yet been recognised — volcano flank terraces.

1. volcano flank terraces

Volcano flank terraces are topographically subtle, laterally extensive bulge-like structures that occur on the slopes of large Martian shield volcanoes. Terraces were first noted by *Carr et al.* [1977] on Mariner 9 images of the upper flanks of Olympus Mons (**Plate 1.1a**), and were later described more quantitatively by *Morris* [1981]. *Thomas et al.* [1990] then reported terraces on the flanks of Arsia, Pavonis, and Ascraeus Montes, using Viking obiter data (**Plate 1.1b-d**). Early works presented sketch maps of terraces on Olympus Mons, drawn from Viking images, and characterised these structures as long, sinuous traces (**Plate 1.2**).

1.1 proposed formation mechanisms

Whilst *Carr et al.* [1977] included terraces in an overview of salient tectonic structures on Olympus Mons, they did not propose an origin for these flank structures. *Morris* [1981] interpreted terraces on Olympus Mons as having formed from high-angle reverse faults, in response to subsidence of the edifice into its central vent or magma chamber.

In the first comprehensive terrace study, *Thomas et al.* [1990] related the convex terrace profile to an origin due to thrust faulting. Using a finite element model for elastic stresses, they concluded that volcano self-loading — the effect of a volcano's mass upon its own strata — generates compressive flank stresses that exceed the yield strength of basalt, leading to radial thrusting. *McGovern and Solomon* [1993] also regarded flank terraces as compressional structures. Again using finite element models, they assessed the contribution of lithospheric flexure to edifice stresses, and how flexure affects strain geometries. Investigating both incremental and instantaneous edifice construction, their models predicted that where a volcano is welded to a flexing lithosphere, early lava units would undergo thrusting due to compression. Later units were less affected, however, and non-welded volcanoes experience no radial flank thrusting at all. As their forecasts for other tectonic structures (e.g. concentric gräben) better correlated to basally detached edifices, *McGovern and Solomon* [1993] ultimately favoured a non-welded model of

volcano development, in contrast to that required for flank thrusting. (Later studies, however, have shown that spatial variations in basal friction can result in an edifice being both welded to and detached from the substrate at different places, e.g. at Olympus Mons [*McGovern and Morgan*, 2009]).

Citing the simple physical models of *Marti et al.* [1994], *Crumpler et al.* [1996] argued that magma chamber growth might steepen the upper flanks of a volcano, through uplift of overlying material along inward-dipping thrusts. These workers suggested that terraces might therefore be folds over blind thrust faults that accommodate magma chamber inflation.

In contrast to previous studies, *Cipa et al.* [1996] preferred an extensional origin for flank terraces, suggesting they are bounded by outward-dipping normal faults. *Montési* [1999, 2000] acknowledged that terraces might be either compressional or extensional in origin, but regarded flank terraces and concentric gräben on the Tharsis Montes as mutually exclusive structures. Discounting gravitational spreading as a formation mechanism for the gräben, *Montési* [2000] instead proposed that flank stress relaxation due to external surface loads emplaced around the volcanoes' bases leads to terrace formation, agreeing with the extensional origin proposed by *Cipa et al.* [1996].

In a discrete element modelling study of gravitational deformation within volcanoes, *Morgan and McGovern* [2005] suggested that, as folds over low-angle thrusts, terraces might represent the toes of shallow gravitational slumps that formed in response to volcano spreading. More recently, these authors have suggested that Olympus Mons has undergone spreading, and resolve the apparent contradiction of extensional distal structures and compressional circum-summit terraces by means of lateral differences in basal friction, though their work does not explicitly address terrace formation [*McGovern and Morgan*, 2009].

2. this study

2.1 rationale

There is thus no consensus as to what type of structure a flank terrace is, much less its mechanism of formation. Most previous work on terraces has been based on remotely sensed photogeological images, yet due to their low relief and large spatial extent, flank terraces are not easily visible in images with sub-optimal lighting geometries [*Thomas et al.*, 1990]. Terrace geometry, as a function of morphology and distribution, can therefore not be determined fully from images alone, and thus remains to be quantified.

Moreover, the geometry of tectonic structures being primarily a result of formation requires terrace geometry to be defined in order to establish the nature of these structures and propose a formation mechanism. Very few studies experimentally address the processes that may form

terraces such as self-loading or volcano spreading, and almost none simulates lithospheric flexure (though *Williams and Zuber* experimentally investigated the effects of incremental loading a brittle plate [1995]). Accordingly, little empirical data exist to support or refute terrace formation hypotheses.

Finally, volcanotectonic structures, particularly on the Tharsis Montes, have served as a framework for much of our understanding of volcanism on Mars [*Crumpler and Aubele*, 1978; *Crumpler et al.*, 1996; *Scott and Wilson*, 1999, 2000; *Wyrick et al.*, 2004; *Bleacher et al.*, 2007], but the difficulty in analysing flank terraces means they feature little in this understanding, or in studies where terrace formation contradicts that of other, more obvious structures [e.g. *McGovern and Solomon*, 1993; *Montési*, 2000].

Consequently, the need exists to review the volcanotectonic development of Martian volcanoes with respect to the nature and origin of all endogenic surface structures, including terraces, in the context of a single, unifying paradigm.

2.2 approach

The problem, therefore, consists of three distinct yet related questions, concerning the nature, origin, and context of volcano flank terraces, which form the basis of this study:

- nature — what is the geometry of flank terraces?
- origin — what is the causal mechanism of terrace formation?
- context — what is the role of terraces within Martian volcano evolution?

Three-dimensional DTM data offer a means with which to establish the nature of terraces; DTMs are not affected by lighting conditions to the same degree as two-dimensional images, and so provide a superior data set with which to study flank terrace geometry. Analogue modelling techniques have a proven heritage when applied to volcanotectonic problems, and can be eminently useful when investigating the terrace origin question. Finally, high-resolution mapping of the surface structures of a terraced case study volcano could help in determining the part of terraces in Martian volcanotectonism.

2.3 thesis overview

This work consists of five chapters: three core chapters preceded by this introductory chapter and succeeded by a brief conclusions chapter. In this first chapter, I outline flank terraces, previous work on these structures, and the motivation behind this work. Each core chapter focuses on one of the three aspects of volcano flank terraces outlined above; these chapters are detailed in the following section. In the final chapter, I present an overview of this study, its chief conclusions,

and an outlook on how this work contributes to our understanding of volcanic systems on the terrestrial planets.

I provide two appendices in digital format on the accompanying Digital Versatile Disc (DVD). The first details the terrace morphometry data discussed in Chapter 2, whilst the second appendix catalogues the two experimental programmes of Chapter 3. The directory hierarchy on the DVD is detailed in this document's Table of Contents, and as a separate file on the disc.

For clarity, the figures and tables in this study are presented (in that order) as separate plates at the end of their relevant Chapters. Where attention is drawn to multiple features in a figure, a numbering system subordinate to the figure number is used: thus, **Plate 3.1: 1** refers to the first element of Plate 3.1, &c.

2.3.1 nature | chapter 2

In this chapter, I describe flank terrace morphology and distribution using DTM data and Geographical Information System (GIS) methods. I characterise the geometry of these structures on the recognised terraced volcanoes Olympus, Ascraeus, Pavonis, and Arsia Montes, Elysium Mons, and Hecates Tholus; as well as three other shields not previously reported as terraced: Alba Patera, Albor Tholus, and Uranius Patera. I also present evidence for terracing on three volcanoes on Earth, where flank terraces have not been reported before: Etna (Sicily), Mauna Loa (Hawaii), and Tendürek Dagi (Turkey). I then appraise the validity of existing formation hypotheses by comparing predicted structural geometries with those observed on Mars, and favour lithospheric flexure as the leading candidate mechanism for terrace formation.

2.3.2 origin | chapter 3

Here, I investigate the formation and development of flank terraces using scaled analogue models of lithospheric flexure. In the first of two experimental programmes I define a characteristic set of load-induced structures, before varying key experimental parameters to examine qualitatively the effects of flexure upon changes in cone morphology, internal layering, and crustal heterogeneity. In the second programme, I report quantitative data on the strain amounts and timing of deformation within a representative set of experiments. Next, I discuss the likely formation of each of a set of characteristic flexure-induced structures, and present a kinematic synthesis of the effects of flexure upon a conical load, before comparing the structures formed in the laboratory with natural examples on Mars.

2.3.3 context | chapter 4

In chapter 4, I examine terraces within the framework of Martian volcanotectonism using Ascraeus Mons as a case study. Ascraeus has an array of prominent structural and morphological features,

including a summit caldera complex, pit craters, sinuous rilles, terraces, and large embayments on the NE and SW flanks. Using DTM and newly available, high-resolution photogeological data of Ascraeus Mons within a GIS, I quantify the number, distribution, and spatial relationships of the volcano's surface structures through detailed mapping. I review these structures' proposed formation mechanisms, to determine if their development is consistent with a paradigm of lithospheric flexure as suggested by the earlier terrace observations, and the analogue modelling results. Finally, I propose a detailed volcanotectonic development sequence for Ascraeus Mons specifically, and, through inference, for large shield volcanoes on Mars in general.

2.4 nomenclature

The terms "flank terrace" and "terrace" are used synonymously throughout this work to refer to the convex structures under discussion. It should be understood, however, that I regard "volcano flank terrace" as the full and correct term for these structures, so as to differentiate them from other geomorphological features that are also referred to as terraces on Mars — specifically caldera terraces [*Roche et al.*, 2001; *Walter and Troll*, 2001] and fluvial terraces [*Kraal et al.* 2008] — but which bear no other relation to the structures considered here. Additionally, I use the adjective "Terran" rather than "terrestrial" when referring to geological features on Earth. Flank terraces may occur on edifices located on other rocky, differentiated planets beyond Earth and Mars (e.g. Venus, Mercury) to which the term "terrestrial" has been applied [e.g. *Head and Solomon*, 1981], but which do not form the focus of this study.

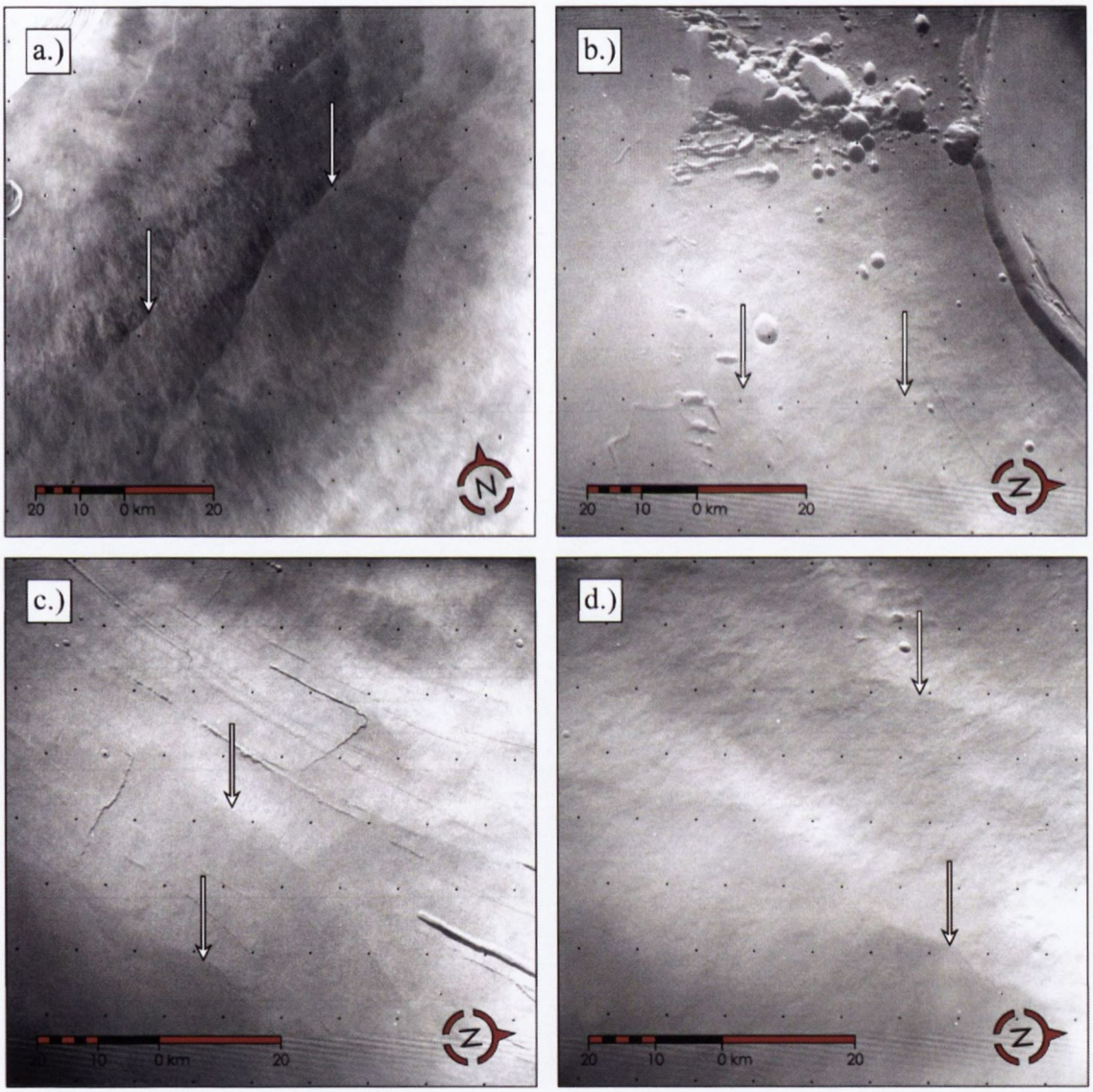

Plate 1.1. Excerpts of Viking orbiter data used in previous terrace studies [i.e. *Carr et al.*, 1977; *Thomas et al.*, 1990]. Readily visible terrace traces are highlighted (heads of white arrows). The moderate resolution and suboptimal lighting conditions of these data hide the extent and complexity of terrace geometries. **a.)** The SE flank of Olympus Mons (frame 046B32); **b.)** the S flank of Arsia Mons (frame 210A45); **c.)** the SE flank of Pavonis Mons (frame 210A37); and **d.)** the SE flank of Ascraeus Mons (frame 210A15).

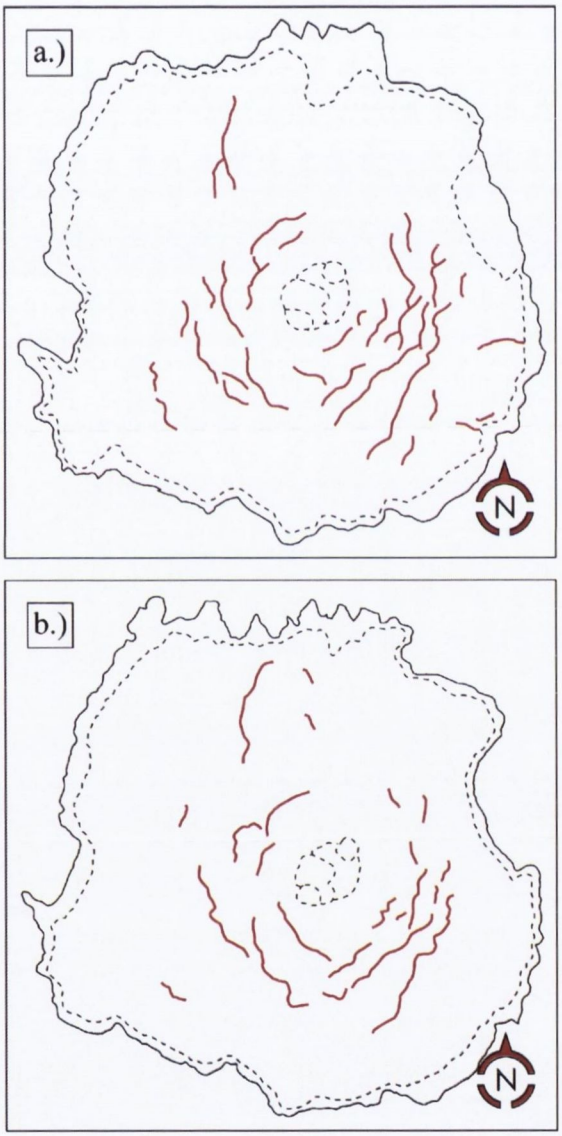

Plate 1.2. Sketch maps of terrace traces on Olympus Mons, derived from photogeological data, after **a.)** Fig. 2 of *Morris* [1981] and **b.)** Fig. 2 of *Thomas et al.* [1990]. The base of the volcano is marked with a solid light line. The top of the basal scarp, and the caldera complex, are marked with dashed lines. The sinuous terrace traces identified by these authors are indicated with heavier, red lines.

introduction

nature | origin | context

conclusions

2 On the morphology and distribution of flank terraces on Mars using photogeological and Geographical Information Systems methods.

overview

Flank terraces are subtle, expansive structures on the slopes of many large Martian shield volcanoes. Several terrace formation hypotheses, including self-loading, lithospheric flexure, magma chamber tumescence, volcano spreading, and shallow gravitational slumping, have been suggested. Terraces are not readily visible on photogeological data; consequently, terrace geometry has not yet been comprehensively described, so terrace provenance is poorly understood.

Three-dimensional topographic data has helped characterise the geometry of these elusive structures, with a view to understanding better the origin of flank terraces, and ultimately how they relate to the tectonic evolution of volcanoes on Mars. Terraces have a broad, convex-upward profile in section, and a systematic "fish-scale" imbricate stacking pattern in plan. They are visible at all elevations, on at least nine disparate Martian volcanoes. Terrace-like features also occur on at least three shield volcanoes on Earth, an observation not recorded before. Analysis of a suite of morphometric parameters for flank terraces showed that they are scale-invariant, with similar proportions to thrust faults on Earth.

Of the formation processes proposed so far, only lithospheric flexure can fully account for the morphology, distribution, and timing of terraces. As a volcano flexes into the lithosphere beneath it, its upper surface will experience a net reduction in area, resulting in the formation of convex-outward thrusts. I contend that these structures correspond to volcano flank terraces.

1. volcanoes in this study

Of the 22 large volcanic edifices on Mars [*Crumpler et al.*, 1996; *Plescia*, 2004], nine volcanoes appear terraced, and are the focus of this study. These volcanoes are located in the Tharsis and Elysium volcanic provinces (none is located in the Circum-Hellas Volcanic Province, recently described by *Williams et al.* [2009]). Key morphometric data for these volcanoes are given in **Table 2.1**. *Zimbleman and Edgett* [1992] describe the morphologies and associated landforms of the Tharsis Montes in detail, whilst *Mouginis-Mark et al.* [1984] review the geology of the Elysium Planitia volcanoes. The primary structural and morphological features of each volcano in this study are described below, but for an overview of all significant volcanic landforms on Mars, the reader is directed to *Hodges and Moore* [1994] and *Plescia* [2004]. Note that a more detailed structural summary of Ascraeus Mons is provided in Chapter 4, section 1.1 (page 55).

1.1 Tharsis volcanic province

The Tharsis Rise is an expansive plateau that straddles the western hemisphere of Mars, and is the location of some of the planet's most recent and extensive volcanism [*Hodges and Moore*, 1994;

Elements of this chapter have previously been published in largely unedited form in Byrne, P. K., van Wyk de Vries, B., Murray, J. B., Troll, V. R. (2009) The geometry of volcano flank terraces on Mars. *Earth and Planetary Science Letters* 281, 1-13.

Lowry and Zhong, 2003] (**Plate 2.1**). The youngest and largest volcanic centres on Mars occur in this province [*Plescia and Saunders*, 1979; *Crumpler et al.*, 1996]. It is host to twelve large shield volcanoes, and swarms of monogenetic cones [*Hughes et al.*, 2008]. Six of those major shields are terraced: Alba Patera, Arsia, Ascraeus, Olympus, and Pavonis Montes, and Uranius Patera.

1.1.1 Alba Patera

Located to the north of the Tharsis Rise (**Plate 2.1: 1**), Alba Patera is the broadest volcanic edifice on Mars [*Carr et al.*, 1977; *Crumpler et al.*, 1996]. The volcano consists of an older, lower construct topped by a summit plateau, whose western flank is topographically higher than the eastern one. A younger shield lies upon the plateau, offset to the SW; the younger shield has a caldera complex with several nested calderas, and is characterised by radiating lava flows and dendritic valleys [*Plescia*, 2004].

Almost all tectonic features associated with Alba Patera are extensional [*McGovern et al.*, 2001]: the shield is flanked by the predominantly N-S Tantalus (E, S) and Alba Fossae (W, N) gräben systems [*Cailleau et al.*, 2003], which postdate the summit, curving around it to form a distinctive "wristwatch" pattern [*van Wyk de Vries and Matela*, 1998]. The Fossae may have formed in response to lithospheric flexure [*Comer et al.*, 1985], sub- and intralithospheric loading [*McGovern et al.*, 2001], or local subsidence coupled with regional extension [*Cailleau et al.*, 2003]. Crater counting has indicated that the lava flows which form the bulk of the edifice are Hesperian (3.5 to 1.8 Ga) to early Amazonian (1.8 Ga to present) in age [*Crumpler et al.*, 1996].

1.1.2 Arsia Mons

Arsia Mons is the southernmost, and oldest, of the three Tharsis Montes, which are aligned on a N40°E trend along the Tharsis rise [*Plescia and Saunders*, 1979; *Hodges and Moore*, 1994; *Zimbleman and Edgett*, 1992; *Plescia*, 2004] (**Plate 2.1: 2**). The volcano's summit is characterised by the single largest caldera on Mars [*Crumpler et al.*, 1996] and associated circumferential gräben [*Crumpler and Aubele*, 1978]; these gräben and faults are more numerous on the W flank, possibly due to the effect of the regional Tharsis topography [*McGovern and Solomon*, 1993]. There is a line of nine small, secondary shields, running across the caldera floor, connecting the entrants on the NE and SW flanks [*Carr et al.*, 1977; *Plescia*, 2004].

Discrete flows originate at the summit, but most later activity came from the coalescence of pits that produced embayments or entrants high on the NE and SW flanks [*Crumpler and Aubele*, 1978; *Mouginis-Mark et al.*, 1982] aligned with the Tharsis rise [*Hodges and Moore*, 1994]. This activity formed large, asymmetric, late-stage lava aprons which extend from the shield to the NE and SW, burying the main flanks [*Plescia*, 2004]. Aureole deposits, distally striated, extend from the desiccated NW flank of the volcano, and are possibly landslide-derived [*Carr et al.*, 1977;

Zimbleman and Edgett, 1992], or are glacial recessional moraines [*Hodges and Moore*, 1979] that show evidence of volcano-ice interaction [*Parsons and Head*, 2005; *Kadish et al.*, 2008]. The proximal ridged terrain on the NW flanks could also have formed as deposits from water-rich sediment rapidly released from inside the volcano [*Morris et al.*, 2003].

Crumpler and Aubele [1978] suggested a developmental sequence for Arsia Mons, based on a combination of crater counting and structural superposition relationships, involving first a main shield-building phase, then the formation of the summit caldera and flank entrants, and finally the extensive NE and SW lava aprons. Applying their system to the other two Tharsis Montes, *Crumpler and Aubele* concluded that Arsia Mons is the oldest of the three. This sequence is described in more detail in Chapter 4, section 1.1 (page 55), and discussed in Chapter 4, section 4.5 (page 72).

1.1.3 Ascraeus Mons

The tallest and northernmost of the Tharsis Montes (**Plate 2.1: 3**), Ascraeus shares the convex-upward morphology, summit plateau, and NE and SW lava "rift aprons" of its counterparts [*Hodges and Moore*, 1994]. The caldera complex hosts between eight [*Scott and Wilson*, 2000] and eleven discrete collapse events [*Mouginis-Mark and Christensen*, 2005].

Pit crater chains and sinuous rilles, whilst present on Arsia and Pavonis, are much more prevalent on Ascraeus Mons, and coalesce into large entrants midway up the S and NE flanks [*Zimbleman and Edgett*, 1992]. Sheet lavas sourced from these entrants form the rift aprons, with the NE apron larger than that to the SW [*Plescia*, 2004]. Aureole deposits also occur at the N base of Ascraeus, and while they are much more areally restricted relative to Pavonis and Arsia [*Zimbleman and Edgett*, 1992], they may share a common hydrological or glacial origin [*Morris et al.*, 2003; *Parsons and Head*, 2005; *Kadish et al.*, 2008]. All deposits occur on the topographic downslope of the Tharsis Rise, similar to those to the NW of Arsia Mons.

Whilst apron lava eruptions temporally overlap across the Tharsis Montes, shield construction of Arsia and then Pavonis Mons predate that of Ascraeus [*Crumpler and Aubele*, 1978].

1.1.4 Olympus Mons

Olympus Mons is the tallest volcano in the solar system [*Wu et al.*, 1984; *Thomas et al.* 1990; *Plescia*, 2004], and towers above the NW flank of the Tharsis-Syria upland [*Carr et al.*, 1977] (**Plate 2.1: 4**). Long recognised as an albedo feature, the volcano was originally called Nix Olympica ("Snows of Olympus") prior to being renamed after the Mariner 9 mission [*Masursky et al.*, 1972].

The shield can be divided into three physiographic subdivisions: the summit caldera, terraced upper flanks, and lower flanks [*Carr et al.*, 1977]. The caldera complex is defined by six calderas

[*Zuber and Mouginis-Mark*, 1992] which broadly trend along a NE-SW orientation, and is slightly offset to the SE [*Crumpler et al.* 1996]; the underlying magma chambers are thought to be situated within the edifice, above the basal plains [*Thomas et al.*, 1990]. The upper flanks are characteristically terraced, with thin, narrow basaltic lava flows appearing to originate at terrace boundaries [*Hodges and Moore*, 1994], whilst the lower flanks are covered in leveed lava channels, radial ridges, and lava fans, suggestive of a concentration of volcanic vents on the upper flanks [*Carr et al.*, 1977].

An escarpment surrounds much of the shield base, rising to between six and eight km in places, but subdued along the NE and SW margins by lava flows [*Carr et al.*, 1977]. The scarp may have been formed by normal faulting [*Morris and Dwornik*, 1978; *McGovern and Morgan*, 2005, 2009], thrust faulting [*Morris*, 1981], erosion of material underlying the shield [*King and Riehle*, 1974; *Head et al.*, 1976], modification of a deposit emplaced before late-stage shield construction [*Tanaka*, 1981], mass movement due to gravity spreading [*Francis and Wadge*, 1983], ice lubrication [*Tanaka*, 1985], high pore fluid pressure [*McGovern et al.*, 2004], or a suglacial eruption [*Hodges and Moore*, 1979].

Beyond the escarpment lie aureole deposits, downslope from the Tharsis Rise [*McGovern and Solomon*, 1993], which are particularly prominent to the NW [*Head*, 1996]. While the nature of these deposits is contentious, they are generally regarded as being causally related to the basal scarp [*Carr et al.*, 1977]. Proposed formation mechanisms include catastrophic movements [*Lopes et al.*, 1980; *McGovern and Morgan*, 2005; 2009], gravity spreading [*Francis and Wadge*, 1983; *Tanaka*, 1985], gravity-induced thrusting [*Harris*, 1977], erosion of sub-glacial eruptives [*Hodges and Moore*, 1979], or ash-flow deposition [*Morris*, 1982].

Relative age dating suggest the upper flanks surfaces are the oldest part of the shield, followed by the lower flanks, with the basal plains the youngest [*Carr et al.* 1977]; late Amazonian in age, Olympus Mons is one of the youngest volcanoes on Mars [*Plescia and Saunders*, 1979; *Crumpler et al.*, 1996].

1.1.5 Pavonis Mons

The middle of the three aligned Tharsis shields (**Plate 2.1: 5**), Pavonis Mons is a broadly symmetric volcano with a summit characterised by a broad, concave depression bounded by a circular rim and radial mare-type wrinkle ridges [*Zimbleman and Edgett*, 1992; *Crumpler et al.*, 1996; *Plescia*, 2004]. A smaller but deeper caldera is offset to the SW of the larger, earlier depression [*Hodges and Moore*, 1994].

Structures on this volcano's flanks are similar to those on Arsia and Ascraeus Montes, including SW-NE aligned embayments, extensive lava aprons on the NE and SW flanks, and lobate aureole deposits to the NW [*Carr et al.*, 1977; *Zimbleman and Edgett*, 1992; *Hodges and Moore*, 1994].

Pronounced, deep concentric gräben crosscut the N flank [*Plescia*, 2004], and arcuate gräben and fractures are evenly distributed across the E and W flanks [*Crumpler et al.*, 1996].

The main shield of Pavonis Mons is younger than that of Arsia, but the latter's NE lava apron overlaps the SW flow of Pavonis [*Hodges and Moore*, 1994]. Additionally, Pavonis' SW lava apron extends around the E flank to overlie its NE apron [*Plescia*, 2004]. As with the other large Montes, the main shield-building phase predates the formation of the lava aprons [*Crumpler and Aubele*, 1978; *Plescia*, 2004].

1.1.6 Uranius Patera

This low basaltic shield is located in the NE Tharsis region, to the immediate east of Uranius Tholus and Ceraunius Tholus [*Crumpler et al.* 1996; *Plescia*, 2000] (**Plate 2.1: 6**). The volcano is elongated NE-SW [*Hodges and Moore*, 1994], and is characterised by radial lava flows, subsidiary flank vents, and minor faulting. Crater counts date the flanks as Late Hesperian in age [*Plescia*, 2000]. Uranius Patera appears to have experienced several stages of growth [*Plescia*, 2004], but construction of the edifice may have been relatively fast: *Plescia* [2000] suggests as little as ca. 10^5 years. The summit caldera complex consists of one large depression, which has coalesced from several smaller calderas aligned approximately parallel to the Tempe Fossae faults to the NE, and is located off-axis relative to the flanks [*Hodges and Moore*, 1994].

1.2 Elysium volcanic province

Elysium Planitia is the second-largest volcanic province on Mars [*Mouginis-Mark et al.*, 1984], and is characterised by a broad regional high with a relatively flat summit plateau [*Plescia*, 2004] (**Plate 2.2**). Three individual volcanoes occur in this region — Albor Tholus, Elysium Mons, and Hecates Tholus — and all three are terraced.

1.2.1 Albor Tholus

Albor Tholus is located SE of Elysium Mons (**Plate 2.2: 1**), on the Elysium Planitia plateau, and has a broadly convex shape [*Plescia*, 2004]. The edifice has a radial, hummocky surface texture with distinct channelised lava flows [*Crumpler et al.*, 1996], and its lower flanks are partially buried by lavas from Elysium Mons [*Mouginis-Mark et al.*, 1984]. There is an annular trough to the N and W of the volcano [*Plescia*, 2004], whilst the nearby Albor Fossae gräben cut the SE flank close to the summit [*Mouginis-Mark et al.*, 1984]; these gräben may be circumferential to Elysium Mons rather than Albor [*Plescia*, 2007]. The summit caldera complex contains two coalesced calderas, and the area immediately surrounding the complex is surrounded by smooth material, possibly late stage ash flows, or related late eruptives [*Crumpler et al.*, 1996]. *Hodges and Moore* [1994] report that this diminutive volcano is Noachian (4.6 Ga to 3.5 Ga) to Hesperian in age.

1.2.2 Elysium Mons

This volcano is the largest of three on the central Elysium Planitia [*Plescia*, 2004] (**Plate 2.2: 2**). Its flanks are channelised with pit craters, rilles, and ridges, though the E flank is morphologically subdued [*Mouginis-Mark et al.*, 1984], whilst the NW flank shows erosional scarring which may be due to volcano-ground ice interactions [*Mouginis-Mark et al.*, 1982].

The single, circular summit caldera is breached to the N by channels that grade into pit chains further down the NE and SW slopes [*Crumpler et al.*, 1996]. The distal margins of Elysium Mons are obscured by extensive lava flows [*Plescia*, 2007]; beyond, concentric gräben circle the volcano [*Mouginis-Mark et al.*, 1984], possibly in response to lithospheric loading [*Hall et al.*, 1983].

The overall shallow slopes and long lava channels [*Plescia*, 2004] of this volcano suggest it is composed of low-viscosity lavas, though the steeper upper slopes may indicate a change in eruptive style and chemistry [*Blasius and Cutts*, 1981]. Elysium is late Hesperian to early Amazonian in age, and is the oldest of the three central Planitia volcanoes; its latest activity embays both Hecates and Albor Tholi [*Hodges and Moore*, 1994].

1.2.3 Hecates Tholus

The domelike shape of Hecates Tholus is situated to the NE of Elysium Mons (**Plate 2.2: 3**), and as it predates Elysium Mons' eruptives, is likely to be Hesperian in age [*Hodges and Moore*, 1994]. A subtle fracture set circles the summit caldera complex [*Crumpler et al.*, 1996], which itself consists of between three and five nested calderas [*Mouginis-Mark et al.*, 1982; *Plescia*, 2007]. Both the caldera complex and the entire edifice is slightly elongate NW-SE, indicating that the regional slope across Elysium Planitia may have influenced the construction of the volcano [*de Pablo et al.*, 2006].

Like basaltic shields on Earth, the flanks are covered with lava flows and channels, linear ridges, and pit chains [e.g. *Plescia*, 2007]. A material that has been reported as a pyroclastic [*Mouginis-Mark et al.*, 1984; *Gregg and Williams*, 1993] or aeolian deposit mantles the lower flanks [*Plescia*, 2004]. *Helbert et al.* [2005] suggest ice may exist within the upper few metres of the volcano's surface. A large caldera on the lower NW flank of Hecates, created by an explosive basaltic eruption, may be filled with glacial deposits [*Hauber et al.*, 2005].

2. methodology

The procedure for this work involved derivation mapping products from three-dimensional Digital Topographic Model (DTM) data, and examining them within a Geographical Information System (GIS). I defined the representative terrace pattern from these data products, identified individual terraces, and then measured a set of terrace parameters for analysis.

2.1 DTM properties and preparation

The principal DTM used in this study is the publicly available USGS 128 pixel-per-degree equatorial Mars Orbiter Laser Altimeter (MOLA) gridded dataset, collected by the Mars Global Surveyor spacecraft during its primary mission phase [*Zuber et al.*, 1992; *Smith et al.*, 2001]. The dataset has topographic coverage of Mars between 88° N and 88° S, an innate equidistant cylindrical projection, and a mean ground resolution of approximately 460 m.

Twenty-two large volcanoes on Mars were examined: Alba Patera; Albor Tholus; Amphitrites Patera; Apollinaris Patera; Arsia Mons; Ascraeus Mons; Biblis Patera; Ceraunius Tholus; Elysium Mons; Hadriaca Patera; Hecates Tholus; Jovis Tholus; Mereo Patera; Nili Patera; Olympus Mons; Pavonis Mons; Peneus Patera; Tharsis Tholus; Tyrrhena Patera; Ulysses Patera; Uranius Patera; and Uranius Tholus.

Each volcano was extracted from the MOLA dataset using ESRI ArcMap 9.1, and placed within its own GIS. The edifice was then displayed with a sinusoidal, orthographic projection, defined with a central meridian specific to its location. The equal-area sinusoidal projection preserves area, and minimises distortion across areas of large spatial extent; this is especially useful for displaying volcanoes not close to the equator (e.g. Alba Patera and Hecates Tholus).

The Spatial Analyst extension in ArcMap was then used to generate slope maps of each edifice. A slope map is the product of calculating the rate of maximum change in elevation from each cell in a surface, and is therefore useful for identifying subtle features, or determining regional slopes. All slope maps were assigned the same colour stretch; steeper slopes have darker colours. In each case, slopes were automatically classified into fifteen bins. This number of divisions was chosen to ensure both large-scale and subtle trends in slope were visible, to enable the detection of as many terraces as possible.

2.2 terrace definition

Thomas et al. [1990] described terraces on Olympus Mons as having a sharp break in slope at their base, and gentle convex topographic profiles. On a slope map of Olympus, a terrace thus appears as a generally planar area bounded by steeper slopes further from the volcano centre, that then terminate against lower, flat terrain (**Plate 2.3**). I used this definition as the basis for identifying flank terraces on this and other edifices: by then marking the boundary between steeper slopes and the following flatter terrain, individual terrace traces were delineated.

2.3 DTM measurements

To characterise flank terraces as quantitatively as possible, and for meaningful comparison between volcanoes, I measured a set of parameters from each terrace map that describes both terrace morphology (lengths and gradient), and distribution (in terms of elevation and position) (**Plate 2.4**).

ArcMap's Editor functions were used to manually delineate terraces, and obtain these parameters from the sketch maps. A terrace boundary was included only where it was clear; structures that resemble terraces but remain equivocal at the resolutions of the datasets were ignored. All discrete bounding traces were then counted for every edifice, giving the total number of terraces for each volcano.

Measurements of terrace traces provided a bounding (arc) length value for each terrace (**Plate 2.4a: 1**), whilst a circumferential (to the volcano) length value was obtained by measuring the straight-line distance between the ends of a terrace boundary (**Plate 2.4a: 2**). Values for radial (to the volcano) length (**Plate 2.4a: 3**) and vertical height (**Plate 2.4a: 4**) were calculated from the horizontal and vertical differences, respectively, between the midpoints of a terrace bounding edge and the line joining its ends. The slope of a line joining these two points served as the gradient value for a terrace (**Plate 2.4a: 5**), and was compared with those of other terraces, and with that of the flank upon which it sits. Average terrace lengths and gradients for each shield were also calculated. As a single terrace can occupy a range of elevations, a specific elevation value was attained for each terrace by measuring the elevation at the midpoint of its bounding edge (**Plate 2.4a: 6**). The range of elevations at which terraces occur on each volcano was then plotted as a percentage of edifice height (**Plate 2.4b**).

2.4 alternative methodology

Prior to manually delineating flank terraces from slope maps, I investigated an alternative method involving automatic edge-detection. This approach sought to identify terraces by examining a derivative surface of a volcano, and identifying points on this surface where one terrace ended and another began: joining these points in plan-view would produce a terrace map.

I used OriginLab® OriginPro 7.5 data analysis and graphing software to derive the Laplacian function from the baseline MOLA data for a study volcano, Ascraeus Mons. The Laplacian function of a surface is a measure of that surface's curvature; as a two-dimensional analogue to the second derivative of a curve, it characterises the rate of change of the slope of the surface. Areas on the volcano with the largest Laplacian values would be those where the slope changes suddenly, corresponding to where one terraces meets another.

This method required specifying upper and lower threshold values within which a feature could be considered a terrace. Establishing these values was difficult due to the level of noise in the MOLA data, however, and it became necessary to visually identify terraces on a slope map and then mark those points on the Laplacian surface. Even small perturbations, e.g. real surface textures or interpolation artefacts, would return large Laplacian values if the rate of change of slope were high. A fast Fourier transform (FFT) algorithm was applied to the data, to reduce the noisiness of the MOLA surface by ignoring short-wavelength features in favour of larger, broader structures.

This process only served to highlight the most obvious terrace edges, however, and could not help distinguish other, more subtle candidate boundaries.

Ultimately, this method was abandoned in favour of manual terrace mapping. Though the technique showed some promise (**Plate 2.5**), the mapping results did not warrant the time invested in it. Some of the more prominent terrace boundaries on Ascraeus Mons were identified, but differentiating a terrace edge from noise proved too difficult to produce a reliable map from which quantitative data could be obtained. Additionally, the threshold values specific to Ascraeus would not necessarily be applicable to other volcanoes in this study, and would require significant recalibration in each case.

3. results

3.1 visibility

Flank terraces on Mars remain detectable on slope maps, despite their subtle topography, irrespective of the ages of the shields upon which they occur [cf. *Neukum et al.*, 2004]. Some late-stage eruptives have obscured or tempered terrace traces in places, indicating that terrace development was, at least in part, contemporaneous with flank volcanism [*Thomas et al.*, 1990]. The general terrace morphology is still present, however, even where partly covered by later lava flows.

3.2 morphology

MOLA transects across Olympus Mons confirm that the terrace profile is characterised by a broad, convex-upward form, with a near-flat upper surface whose slope increases towards the terrace base, as reported by *Thomas et al.* [1990], forming a characteristic rounded "nose" (**Plate 2.6**). DTM-derived slope maps provide a clear insight into terrace plan-view morphology, and show that terrace bases are delineated by convex-outward arcuate traces, and are generally not laterally continuous. Terraces are configured in an overlapping manner, wherein the upper portion of one terrace is superposed upon a topographically lower, adjoining terrace. This imbricate arrangement forms a distinctive "fish-scale" stacking pattern in plan (e.g. **Plate 2.7**). Where terraces occur close together, many bounding traces terminate at the midpoint of a topographically higher terrace.

3.3 distribution

Whilst the fish scale-stacking pattern is systematically manifest upon every terraced volcano, the number, size, location, and consequently plan view distributions of terraces on each shield vary considerably. MOLA slope maps, and the derived terrace sketch maps, are provided here for all volcanoes on Mars (**Plates 2.7–2.15**).

3.4 morphometric data

The key geometrical parameters described in section 2.3 were measured for each Martian terrace in the study (1,279 in total); average values per volcano are presented in **Table 2.2**. The entire dataset for every volcano in this work is tabulated in **Appendix I.I**.

4. discussion

4.1 timing

That terraces are still evident on Mars today suggests either they are late-stage structures, or they form continually. They may reflect a single phase of deformation, or the latest increment of strain in an ongoing process. If the former applies, terraces develop upon some of the last units to be emplaced, towards the end of the main shield-building phase. If terraces are recurring structures, their bounding faults may serve to accommodate shape change in a volcano throughout its lifetime.

4.2 morphology

Normal faults tend to manifest as abrupt changes in slope, and where accommodating extension on a volcano, occur as concave-outward structures in plan [*van Wyk de Vries and Borgia*, 1996]. Thrusts are characterised by lobate leading edges, often with a convex-outward plan configuration [*Twiss and Moores*, 1992, p. 96–112]. The convex-upward terrace profile is thus consistent with thrust fault morphology in a compressive stress regime, and is unlike that produced by normal faulting due to extension. The upper flat area of a terrace probably corresponds to the culmination of a thrust anticline, and may be further flattened by sediment accumulation [*Borgia and van Wyk de Vries*, 2003].

Terrace traces often terminate close to the midpoints of adjoining terraces, possibly due to geometric coherence [*Walsh and Watterson*, 1991], whereby strain is accommodated across several structures in a single fault system. This relationship between terrace traces, and the fish-scale pattern in general, is suggestive of a systematic method of flank terrace formation. Moreover, as the same pattern appears on each terraced volcano, the mechanism of terrace formation must also be similar for every such shield. Key terrace morphology parameters for Mars are graphed in **Plate 2.16**, and are discussed below.

Maximum displacement along a thrust fault usually occurs normal to the midpoint of a chord joining its ends (the bow-and-arrow rule). A log-log plot of strike (chord) length versus maximum horizontal displacement for thrusts on Earth yields a linear relationship [*Elliot*, 1976]. As the displacement of a thrust fault is proportional to the amplitude of its surface expression (e.g. a fault propagation fold or fault scarp), I use terrace radial length as a rough proxy for horizontal fault displacement. When plotted against terrace circumferential (chord) length, then, the data describe a

linear relationship, follow a power law function, and are scale-invariant (**Plate 2.16a**). That they behave similarly to known tectonic structures on Earth further supports the possibility that flank terraces are the surface expressions of thrust faults. If so, their low amplitude morphology represents shortening on the flanks of only a small order (perhaps less than 10% but this value remains to be quantified).

A linear plot of terrace bounding length versus circumferential, radial, and vertical length values indicates that terrace proportionality is also scale invariant: that is, the relative ratios of each of these parameters remain the same across all scales (**Plate 2.16b**). Therefore, whilst terrace size may vary between volcanoes, and even across a single edifice, flank terrace shape as described by these parameters remains the same. Terrace size may differ upon and between volcanoes due to a range of factors (see 4.3).

The ease with which a terrace can be seen in images is a function of its slope — specifically, the gradient of its leading edge. Terrace formation may change the slope of the flank of the volcano on which it occurs. The average volcano slope may increase or decrease depending on the ratio of flat to steep areas on a terrace population, which in turn is contingent on the formation process. Comparing the average slope value for each Martian volcano, adopted from *Plescia* [2004] and representative of the overall shape of the shield, with the average slope of all terraces on that volcano, produces a correlation (**Plate 2.16c**).

Qualitatively, steeper, more prominent terraces occur on volcanoes with steeper average flank values, e.g. Ascraeus Mons (**Table 2.2**). Terrace prominence is also greater on volcanoes with nested caldera complexes (e.g. Olympus and Ascraeus Montes). Terrace slopes may thus reflect the gradients of the flanks upon which they form. They might also be steepened if flank slopes increase, e.g. due to buttressing by regional topography [*McGovern and Morgan*, 2005]. Alternatively, volcano flanks may be steepened by the reactivation of terrace bounding faults. There is currently insufficient evidence at this point, therefore, to explain the link between average terrace and average flank slopes; here I simply report that there is a correlation.

4.3 distribution

Flank terraces occur at all elevations on a volcano, and are not restricted to the upper flanks as previously reported [*Thomas et al.*, 1990; *McGovern and Solomon*, 1993]. For example, terraces on Olympus Mons extend from the summit to the top of the basal scarp; on Ascraeus Mons, they continue to the base of the volcano (**Table 2.2**). Therefore, as terraces are present across a range of flank elevations on all volcanoes studied, so too are the conditions responsible for terrace formation, whatever their nature.

Some volcanoes display an axisymmetric distribution of terraces (e.g. Elysium Mons), whilst others show a high degree of asymmetric terracing (e.g. Uranius Patera) (see **Plates 2.11** and **2.15**,

respectively). Differences in internal architecture, volcano geometry, internal and regional-scale stresses, and basal friction could account for the variation in terrace distribution on the studied edifices, e.g. Olympus Mons [*McGovern and Morgan*, 2009], and for the range of terrace sizes observed.

Other factors can affect how and where terraces occur on Mars. Aeolian or mass-wasting processes might erode terrace traces, leaving some areas devoid of these structures, e.g. the NW flank of Arsia Mons. The erosional morphologies of the highland paterae [*Crown and Greeley*, 1993] are consistent with an absence of terraces on these volcanoes. DTM data quality also influences the location and number of terraces I can report. MOLA interpolation artefacts occur on the W and E flanks of Albor Tholus, which in turn do not appear terraced.

Additionally, terrace-like structures below MOLA resolution have been ignored. It is likely, therefore, that the total number of terraces on Mars presented herein is under-representative of the actual number. It is also likely that the total number of terraced volcanoes on Mars is greater than that provided here, and so should be treated as a minimum. Smaller shields such as Apollinaris Patera, Biblis Patera, Ceraunius Tholus, Jovis Tholus, Tharsis Tholus, Ulysses Patera, and Uranius Tholus could also be terraced, though high-resolution DTM data is required to test this.

4.4 terraces on Earth

What of terraces on other terrestrial planets? Topographical data exist for very few volcanic planets, inhibiting the accurate identification of terraces on other worlds (e.g. the Magellan synthetic aperture radar dataset for Venus [*Saunders and Pettengill*, 1991] lacks the resolution to identify flank terraces). Terrace formation could be hampered by the lack of true volcanic edifices on the Moon [*Head and Wilson*, 1991] and Mercury [*Head et al.*, 2009]. Moreover, sustained volcanism like that on Io [e.g. *Williams et al.*, 2007] would serve to obscure terraces.

Similar considerations apply to volcanoes on Earth. Vegetation, anthropological activity, increased rates of erosion and ongoing volcanism, the difficulty in seeing these structures in the field, and a lack of previous recognition of flank terraces may have precluded the identification of terraced volcanoes on this planet. However, thrust faults in the lava pile of the Palaeogene Mull volcano (Scotland) have produced anticlines and pop-up structures that may be analogous to flank terraces [*Mathieu and van Wyk de Vries*, 2009], whilst thrusting on the lower flanks of Concepción volcano (Nicaragua) might be the equivalent of terraces formed during the volcano's early flexure and compressive phase [*Borgia and van Wyk de Vries*, 2003].

To investigate whether terrace-like structures occur on Earth (for which DTM data is readily available), I extended this work to include large Terran shield volcanoes, using the Shuttle Radar Topography Mission (SRTM) DTM dataset [*Farr et al.*, 2007] and the methods described in

section 2.1. This dataset has topographic coverage of Earth between 60° N and 54° S, and a ground resolution of three arc-seconds (approximately 90 m).

Thirty shields on Earth were inspected: Alayta and Zukwala (Ethiopia); Aoba (Vanuatu); Ararat (Turkey); Arenal (Costa Rica); Bioko Island (Gulf of Guinea); Casita, Cosiguina, Mombacho, and Telica (Nicaragua); Etna (Sicily); Alcedo, Cerro Azul, Darwin, Fernandina, San Cristobal, Santa Cruz, Santiago, Sierra Negra, and Wolf (the Galapagos); Halla (South Korea); Karthala (Comoros); Kilimanjaro (Tanzania); Mauna Loa (Hawaii); Mount Cameroon (Cameroon); Piton de la Fournaise (La Réunion); Salina (Italy); Tarso Tousside (Chad); Tendürek Dagi (Turkey); and Tenerife (Canary Islands). This selection represents a broad range of ages, geometries, and locations of volcanoes for which SRTM data quality was sufficient for slope map analysis.

Three Terran edifices — Etna, Mauna Loa, and Tendürek Dagi — display terrace-like structures that do not have a clear volcano-constructional origin, yet have a convex-upward, convex-outward morphology and are distributed in a fish-scale imbricate pattern, similar to flank terraces on Mars. These terrace structures, which number 334 in total, are located in areas where flank-parallel compression may occur, but not in areas where extension is dominant. SRTM-derived slope and sketch maps follow (**Plates 2.17, 2.19,** and **2.21**), with an overview of each terraced Terran volcano as a context for these structures.

4.4.1 Etna

Etna volcano, Sicily, is a large lava shield with a central caldera-vent complex and N-S orientated main rift zones [*Chester et al.*, 1985]. Spreading structures upon the E side of the volcano indicate that this flank is moving laterally eastwards into the Ionian Sea [*Borgia et al.*, 1992]. Etna is located in a N-S zone of regional contraction, and large-scale compressional features are observed at its southern foot [*Branquet and van Wyk de Vries*, 2001]. Because of its large mass, its situation on ductile substrata, and because it is little eroded, Etna is a suitable site to search for structures whose morphology matches that of flank terraces.

SRTM slope maps of Etna show arcuate, terrace-like features on the lower N flank, from the NW to the NW, and on the SW flank. These features have a primary E-W orientation (**Plate 2.17**) and an average circumferential length of 1.8 km. These structures were visited in the field, but are extensively farmed and feature significant vegetation coverage (**Plate 2.18**). The convex-upward terrace shape is clearly visible, thus confirming the DTM observations, but any associated deformation proved impossible to identify conclusively on the ground. The lava flows are significantly autobreciated and cut by many cooling fractures. For this reason I suggest that the strain during terrace formation would be accommodated by the movement of pre-existing fractures, and would thus be very difficult to detect at outcrop unless the strain amount were high. Strain localisation might develop some discrete structures, however. The thrust reported by *Borgia et al.*

[1992] is located in the southern zone of likely terraces, and may in fact be the first reported field example of a terrace-forming thrust fault.

Geological maps of the volcano, field inspection, and Google Earth™ images were also used to assess the relationship of the terrace-like structures with known eruptive features. The terraces are wider than any lava flow or eruptive structure (cones and aligned vents) on the volcano. In addition, eruptive constructs (e.g. cones, fissures, and lava flows) are aligned down-slope, whereas the terraces are arranged cross-slope. There is no clear spatial relationship between the terrace features and the observed constructional landforms, so whilst it is possible that the terraces have some obscure constructional origin from successive lava flows, they do not match any known eruptive morphology. They are distributed normal to the N-S direction of regional contraction, which has probably created the southern Catania anticline [*Branquet and van Wyk de Vries*, 2001]. These terraces are absent from the spreading E flank of the volcano, but their position and orientation is consistent with a N-S tectonic shortening of Etna.

4.4.2 Mauna Loa

The big island of Hawaii is dominated by the Mauna Loa and Kīlauea volcanoes. The surfaces of these volcanoes are not heavily eroded, and as the entire island is undergoing large-scale flexural sagging (e.g. *Thurber and Gripp*, 1988], Hawaii is also a suitable candidate site for terraces.

An array of terrace-like features is distributed over a wide area to the NW of the summit caldera on Mauna Loa (**Plate 2.19**). These features extend from near the summit to the base of the subaerial edifice, which abuts Hualālai and Mauna Kea. They have an average circumferential width of 1.9 km. DigitalGlobe images, visible via Google Earth™, reveals a 0.1-km scale undulating surface of long, ribbon-like ʻaʻā and pāhoehoe lava flows (**Plate 2.20**), that can also be seen on the geological maps of the volcano. Some eruption sites show branching fans, with central pāhoehoe and external ʻaʻā zones, and an axial cone. The lava features form small, convex-upslope topographic rises that, whilst clearly visible on satellite images, are below the resolution of 90 m SRTM data. In contrast, the terrace-like structures are far wider and broader than the lava features. They occur on a sector buttressed by Hualālai to the NW, but not on rift zones of the mobile, extending SE flank that abuts Kīlauea. These features are therefore located in a zone where slope-parallel compression is possible. In view of the flexure of the island, these terraces are perhaps coupled with local sinking of the dense complex below the summit [*Walker*, 1992].

Again, a constructional history for these structures involving superposition of many flows cannot be disregarded, but they appear to have the same general morphology and distribution as Martian flank terraces and those on Etna. The terrace-like features on Mauna Loa are generally restricted to the upper flanks. Morgan and McGovern suggest that extensive gravitational spreading has occurred on both Hawaii and Olympus Mons [*Morgan and McGovern*, 2005]. Whilst the bases

of the volcanoes might have experienced outward spreading, the upper flanks may be still compressed under the relative contraction induced by flexural sinking. Such a central compressional situation was suggested by *McGovern and Solomon* [1993] and *Borgia* [1994], and shown to be possible by *van Wyk de Vries and Matela* [1998]. In addition, the possible buttressing effect by Hualālai on Mauna Loa is similar to that proposed for the SE sector of Olympus Mons by the neighbouring Tharsis Rise [*McGovern and Morgan*, 2005]. The terraces on both volcanoes are thus found in similar volcanotectonic contexts.

4.4.3 Tendürek Dagi

This remote shield volcano, located in eastern Turkey, has a circular shape in plan view. Satellite images show that the volcano is built of successive, superimposed lava fields. The volcano has a fresh, little-eroded morphology, a large mass, and stands on sedimentary strata (**Plate 2.21**). On the SRTM slope maps terrace-like structures are arranged in a generally concentric pattern about the edifice, and have an average circumferential length of 1.5 km (**Plate 2.22**). Lava flow lobes are also visible in the DTM data, but have distinctive steep fronts and sides. This flow morphology is much longer and narrower than that of the terrace-like features, which, like before, do not correlate to any of the observed lava flows on imagery. Tendürek Dagi is an inaccessible volcano blighted by minefields, and thus is not easy to visit. This remote sensing work, however, has shown the presence of terrace-like structures that closely correspond morphologically and spatially to those observed on the Martian volcanoes in this study.

4.4.4 morphometry

These Terran terraces were measured according to the method described in section 2.3. Morphometric data for these structures are given in **Table 2.3** and in **Appendix I.II**. Aside from a morphological similarity, these features correlate strongly with Martian terrace morphometry (section 4.2): radial versus chord length values for Earth plot in the same fashion as Martian values, following a linear power law function (see **Plate 2.16a**), whilst the relative ratios of length values for the Terran structures are also maintained across all scales (see **Plate 2.16b**). I propose, therefore, that they are possible Terran flank terraces, equivalent to those on Mars.

4.5 formation mechanisms of flank terraces

Several mechanisms, both extensional and compressional, have been suggested for flank terrace formation. Each of these processes produces a characteristic set of structures (**Plate 2.23**) whose geometry can be compared to that of flank terraces. Here I review these mechanisms with regard to the observations of Martian terraces discussed above.

4.5.1 extensional mechanisms

Cipa et al. [1996] regarded terraces as concave-outward structures, bounded by outward verging normal faults accommodating volcano spreading. The interpretation of concentric dyke swarms on Arsia and Pavonis Montes led *Montési* [2000] to suggest that these volcanoes underwent a separate evolutionary path to Ascraeus and Olympus Montes, which are described as terraced due to flank relaxation. Whilst concentric gräben are not readily apparent on Olympus or Ascraeus Montes, MOLA data indicate that all four volcanoes are terraced, and so the mechanism of terrace formation must apply to each Tharsis Mons and cannot be exclusive to edifices with concentric gräben development. Furthermore, gravitational spreading of a volcano due to a weak substrate or underlying décollement will be apparent as an increase in basal diameter, accommodated by the development of radially orientated, concave-upward "leaf" gräben [*van Bemmelen*, 1949; *Borgia*, 1994]. These structures are evident on Maderas volcano, Nicaragua, which is spreading upon lacustrine and marine sediments [*van Wyk de Vries and Borgia*, 1996] (**Plate 2.23a**). DTM data, however, show that Martian volcano terraces have a convex-upward, convex-outward morphology, which differs significantly from that predicted to occur due to volcano spreading.

Morgan and McGovern [2005] and *McGovern and Morgan* [2009] interpreted Olympus Mons' concave lower flanks and extensive aureole deposits as evidence for spreading of the edifice upon a central low-strength décollement (**Plate 2.23c**), though these authors described a scenario in which a single volcano may locally experience both spreading and flexure (e.g. Olympus Mons, due to variations in basal friction beneath the volcano), a situation that also allows thrusting to account for flank terraces. Their view, therefore, considered both extensional and compressional mechanisms as agents of terrace formation, but is included in this section as they discuss the possible role of extension in the development of terraces.

In both *Morgan and McGovern* [2005] and *McGovern and Morgan* [2009], these authors proposed that some terraces were the toes of shallow slumps mobilised during spreading, although slumping should result in subtle concave-outward head scarps, features that are not evident on this volcano or any other terraced shield. Some scarps could have been obscured by later volcanism, but there is no record of these structures even where terraces approach summit elevations on shields with a record of flank eruptions, e.g. Elysium Mons. Additionally, whilst low-competency substrata such as phyllosilicate minerals [*McGovern and Morgan*, 2008; 2009] may account for extensional structures at the base of Olympus Mons, its terraces are geometrically similar to those on other terraced volcanoes (**Table 2.2**), most of which show no signs of distal extension at all.

4.5.2 compressional mechanisms

As *Thomas et al.* [1990] did not provide a mechanical definition of self-loading, I take it to mean the equilibration of a volcano's geometry under gravity, whilst the summit elevation decreases and

the basal diameter remains fixed or decreases (were the base free to increase in diameter, volcano spreading would occur, accompanied by extension of the upper flanks). *Thomas* and co-authors did not consider viscoelastic stresses in their models beyond its elastic response to the applied loads, and so the behaviour of the underlying crust was not examined. Assuming then that a volcano's base does not significantly sag into the underlying crust, and that loading is restricted solely to the edifice, the volcano's volume must be conserved. Its shape will therefore evolve from conical to increasingly domical. This shape change may result in the formation of radially oriented extensional structures, which are not a commonly recognised feature of large Martian shields [e.g. *Crumpler and Aubele*, 1978, *Hodges and Moore*, 1994, *Plescia*, 2004].

Additionally, *Thomas et al.* [1990] suggested that a filled, high-level magma chamber within Olympus Mons, present throughout the duration of terrace formation, localised loading-induced compressive stresses at elevations that agree with their observed positions of terraces high upon the volcano's flanks. DTM data show that terraces are not restricted to the upper flank of Olympus, however, nor are they localised so on any other terraced edifice.

Marti et al. [1994] showed that magma chamber growth results in the formation of a dome above the chamber, accommodated by inward-dipping concentric reverse faults. *Crumpler et al.* [1996] suggested that the cumulative effects of such chamber tumescence could result in the steepening of volcano flanks, and possibly in the formation of terraces. Terrace morphology does not support this hypothesis, however. Whilst the concentric faults of *Marti et al.* [1994] bounded a convex-upward structure, they did not form an intersecting fish-scale pattern like those of terrace bounding faults: therefore, the domical structure so formed does not resemble flank terraces (**Plate 2.23b**). Additionally, with continued inflation the dome's upper surface developed a polygonal network of fractures, evidence for which is lacking on the upper flanks of terraced Martian shields. These polygonal fracture patterns, coupled with radial fractures, also developed in experiments conducted by *Walter and Troll* [2001] and *Troll et al.* [2002], who modelled chamber tumescence beneath both a flat surface and cones of varying geometries. *Marti et al.* [1994] and *Walter and Troll* [2001] concluded that upon evacuation of the magma chamber these faults could invert their sense of throw, becoming normal ring faults. This activity could potentially serve to offset the effects of cumulative magma chamber tumescence and any associated structures.

The compressional stresses associated with magma chamber inflation manifest circumferentially about the chamber [*Marti et al.*, 1994], yet several of the terraced Martian shields bear no evidence of terracing on certain sectors, e.g. to the SW of Hecates Tholus, and on the E flank of Uranius Patera. This may be due to the localisation of stresses within these volcanoes (see 4.3.2). Conversely, these perceived preferential zones of terracing may be due to other factors (see 4.4). In addition, whilst tumescence produces uplift above an inflating chamber, terraces occur at flank elevations close to or at the base of the cone on several volcanoes, e.g. Ascraeus Mons and Hecates

Tholus (**Table 2.2**). These structures are thus below any shallow magma chamber responsible for caldera formation, assuming shallow chambers are located at neutral buoyancy zones within the edifice [e.g. *Zuber and Mouginis-Mark*, 1992; *Wilson & Head*, 1994].

A large volcanic load can induce flexure of the underlying lithosphere, and can in turn affect the stress fields within the edifice. The presence of circumferential gräben and flexural troughs about some of the largest Martian shields indicates that lithospheric flexure has indeed occurred [*Comer et al.*, 1985; *Zuber et al.*, 1993]. Flexure may produce wholly compressive structures that match terrace geometry well, in response to the horizontal compression of an edifice. The development of a flexural depression beneath a volcano might serve to reduce its elevation, whilst a proximal flexural bulge may prevent the basal diameter from increasing (though this effect could be negated as the bulge migrates outward as the edifice grows [*McGovern and Solomon*, 1997]). The volcano enters a state of stress where σ_1 is radial, σ_2 concentric, and σ_3 vertical [*McGovern and Solomon*, 1993; *van Wyk de Vries and Matela*, 1998]. Strain is apparent in this case as a net reduction in surface area, accommodated by outward verging circumferential thrusts [*McGovern and Solomon*, 1993, and allowed for by *Morgan and McGovern*, 2005]. I consider these structures to correspond to flank terraces (**Plate 2.23d**). As the entire edifice is likely to experience the effects of flexure, these structures may form across a wide range of elevations, similar to observations on Mars and Earth.

Furthermore, whilst certain extensional structures do exist on the flanks of several large Martian shields [*Hodges and Moore*, 1994], flexure does not require the formation of radially oriented tension fractures, structures that are predicted by other formation mechanism hypotheses but are conspicuously absent on terraced volcanoes. *McGovern and Solomon* [1993] modelled instantaneous and incremental emplacement of volcanic loads welded to an elastic lithosphere, and found that both situations generated circumferentially oriented thrusts. Latter-stage units emplaced incrementally in their models did not experience compressional failure. Terraces are visible today, however, long after the volcano construction phase has presumably finished. This suggests that terraces are not in fact produced during the emplacement of discrete lava flows, as horizontal compressive stresses decrease with each successive load increment [*McGovern and Solomon*, 1993]. In addition, later volcanism could completely obscure earlier terrace traces, were they to be formed. Instead, terracing must occur, at least in some cases, after most volcanism has taken place and can thus be a late-stage event. This scenario may be similar to the *McGovern and Solomon* model of an instantaneously emplacement load, where formation of a volcano is rapid relative to the time required for the lithosphere to flex. A short main shield-building phase for Martian volcanoes is possible, if eruption/effusion rates were sufficiently high [e.g. *Plescia*, 2000].

4.5.3 applicability to Mars and Earth

Elastic self-loading, whilst likely to occur in large volcanoes on Mars and Earth, does not adequately account for the morphology and distribution of flank terraces. Additionally, *Thomas et al.* [1990] invoke a specific magma chamber condition for Olympus Mons to account for their perceived distribution of terraces that may not be applicable for other terraced edifices on either planet. Magma chamber tumescence does not generate convexities matching the fish-scale terrace-stacking pattern, but does produce radial fractures that are not observed; moreover, this mechanism cannot account for the elevations and distributions of terraces upon many of the studied shields. Volcano spreading and gravitational slumping produce negative-relief flank structures that do not match the characteristic convex-upward terrace profile. Neither slump scarps nor radial gräben are spatially coincident with flank terraces on any of the Martian or Terran study volcanoes.

However, lithospheric flexure can produce structures that, as surface expressions of shallow faults formed as a volcano's surface area decreases, match the compressional geometry of flank terraces. Flexure could also account for the development of terraces late in an edifice's active lifetime, and may be common to all volcanoes discussed herein by virtue of their large masses inducing flexure. Indeed, there is evidence that flexure has occurred underneath many of the large volcanoes on Mars and Earth [e.g. *Comer et al.*, 1985; *Walcott*, 1970]. If terraces develop in response to a net reduction in volcano surface area, however, flexure may not be the only mechanism capable of generating these structures. Regional tectonism (e.g. across Etna) or topographic buttressing (e.g. on the SE flanks of Olympus Mons and Mauna Loa) may also serve to constrict the upper surface of a volcano as effectively as lithospheric flexure, also leading to the formation of flank terraces.

5. concluding remarks

The MOLA dataset has proven useful in identifying flank terraces on at least nine Martian shield volcanoes, and comprehensively establishing terrace geometry. The convex-upward, convex-outward terrace morphology resembles that of thrust faults on Earth, whilst the ubiquitous, imbricate fish-scale terrace distribution pattern suggests a systematic process of formation for these structures. The scale-invariant nature of terraces is a property common to tectonic structures.

Their presence on shields that differ in size, location, and age across Mars implies that they are a fundamental volcanotectonic structure, and form due to a process that can apply to all nine volcanoes; the discovery of flank terraces on at least three Terran shields further reinforces this conclusion. Comparing these observations of terrace geometry with those predicted by existing formation hypotheses, lithospheric flexure appears to be the primary agent responsible for flank terrace formation.

I conclude, therefore, that flank terraces are fundamental volcanotectonic structures, that they are not restricted to Mars, and that they are the surface expressions of thrust faults, probably formed by lithospheric flexure. Experimental modelling is required to verify this origin hypothesis for flank terraces, and is the focus of Chapter 3.

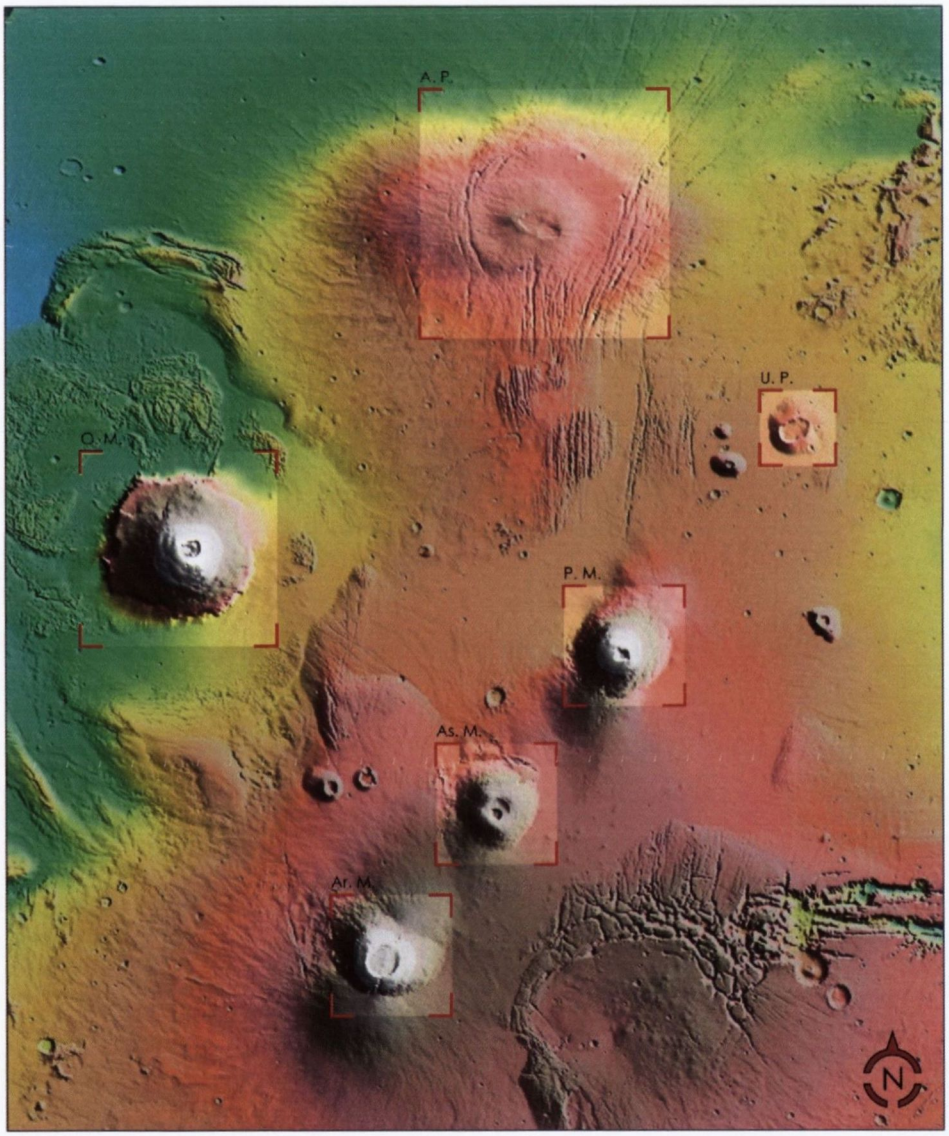

Plate 2.1. A MOLA hillshade of the Tharsis Volcanic Province on Mars. Colours correspond to elevation; the warmer colours indicate higher terrain, the cooler colours *vice versa*. Though home to twelve large shield volcanoes, six are the focus of this work, and these volcanoes are identified as such: A. P. Alba Patera; Ar. M. Arsia Mons; As. M. Ascraeus Mons; O. M. Olympus Mons; P. M. Pavonis Mons; and U. P. Uranius Patera. Scale varies across the image, which has an equidistant projection. Image credit: JPL/NASA.

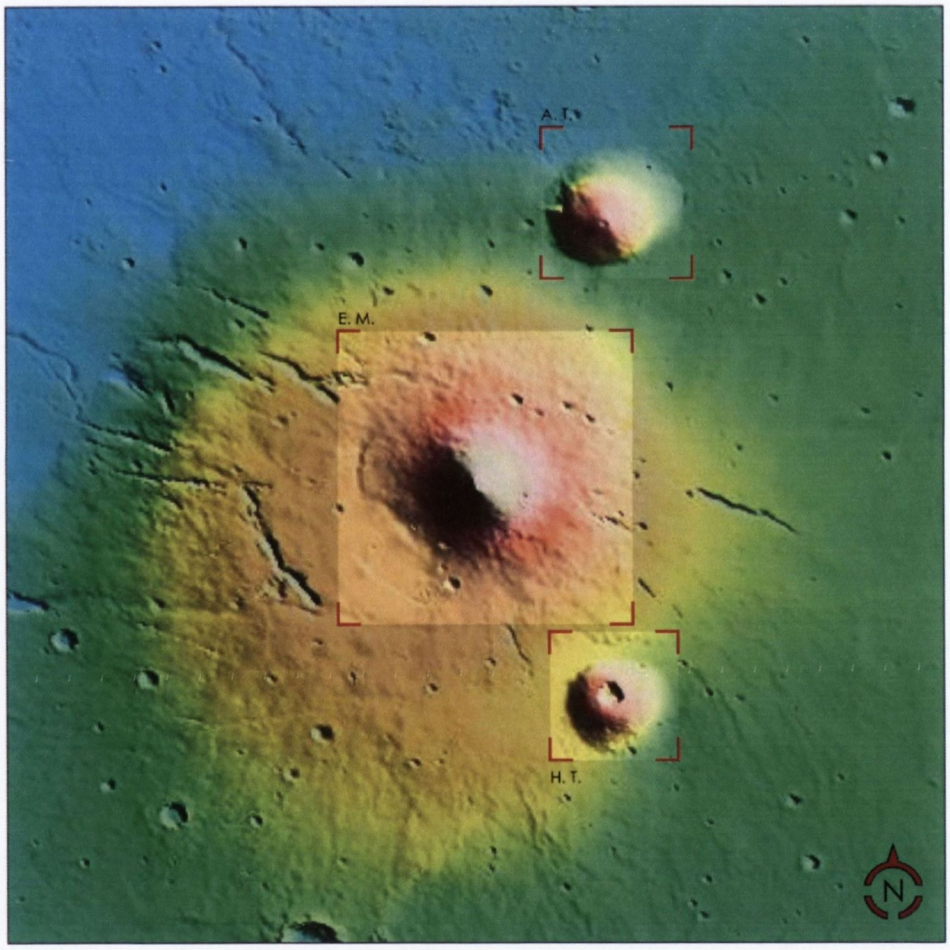

Plate 2.2. MOLA hillshade of the Elysium Volcanic Province on Mars. Colours are as described for Fig. 1. The three volcanoes under consideration here are: A. T. Albor Tholus; E. M. Elysium Mons; and H. T. Hecates Tholus. Scale varies across the image, which has an equidistant projection. Image credit: JPL/NASA.

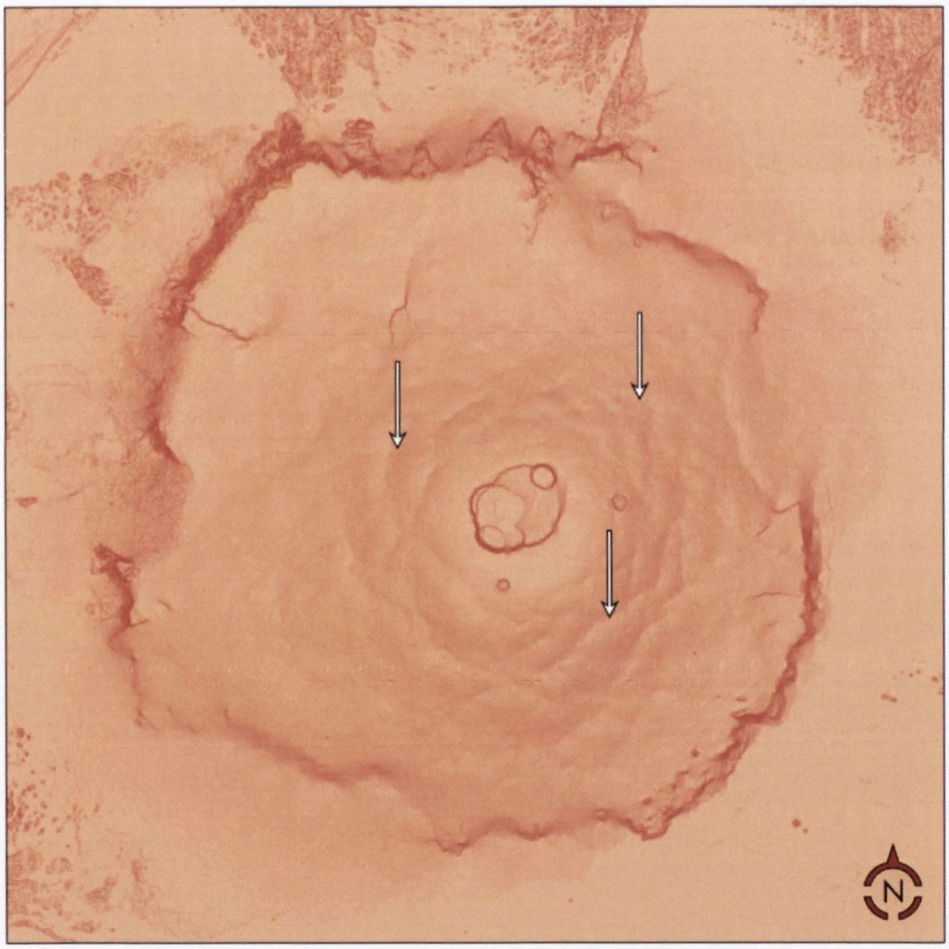

Plate 2.3. MOLA-derived slope map of Olympus Mons. Slopes are classified into fifteen bins, and colours darken with increasing gradients. The steep basal scarp thus appears dark, whilst the summit plateau is light coloured. The pattern of arcuate areas of darker colour juxtaposed against zones of lighter colour denotes the flank terraces upon Olympus (examples at head of white arrows).

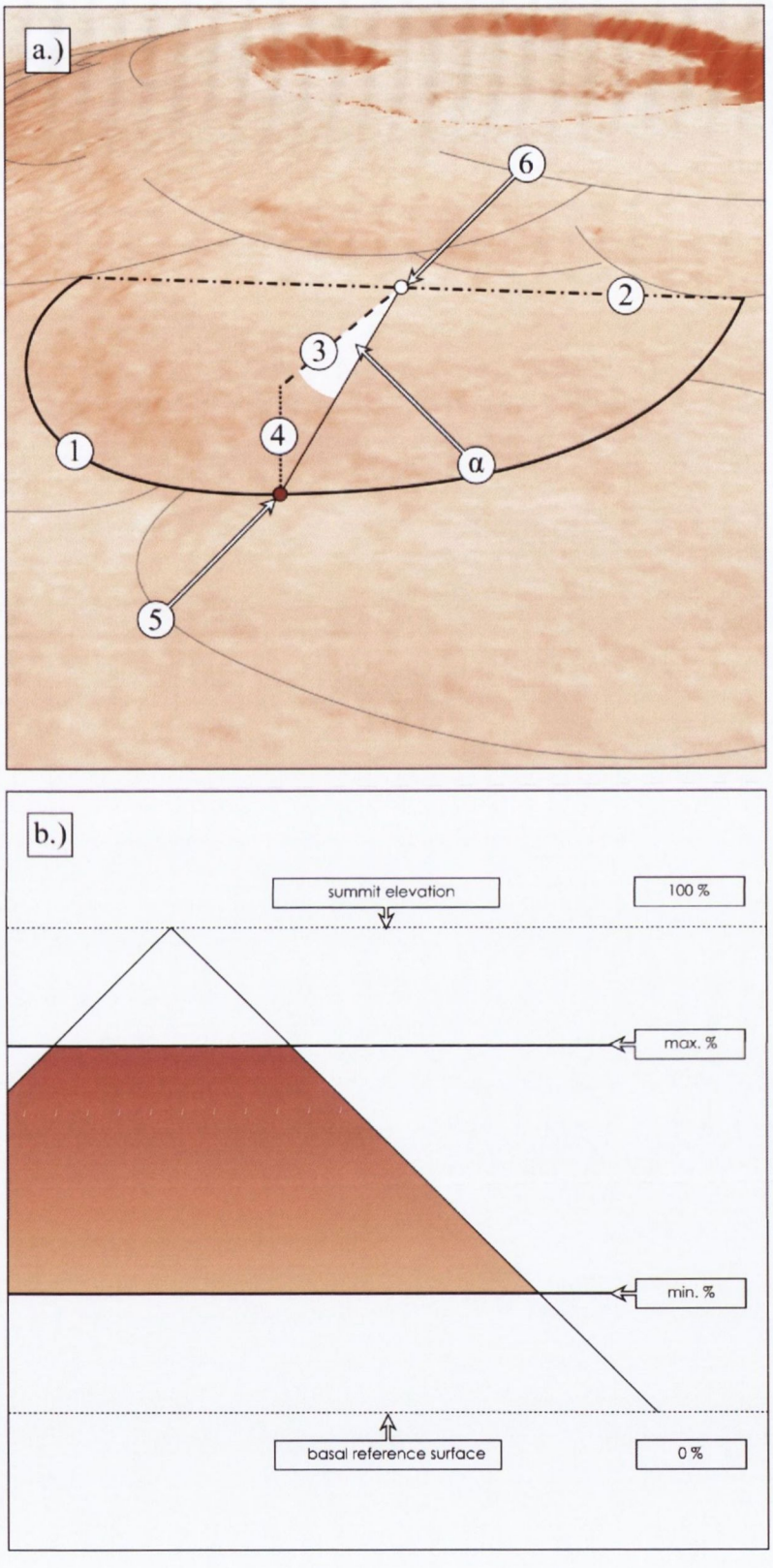

Plate 2.4. Schematic diagrams showing the various parameters we measured from the terrace traces. **a.)** The parameters describing terrace morphology: (1) bounding edge length (solid line); (2) chord length (dot-dashed line); (3) radial length (dashed line); and (4) vertical height (dotted line). Shown too are the bounding line and chord line midpoints (5 and 6, respectively), from which slope and elevation values were obtained, and (α), the angle which describes the terrace gradient. **b.)** Terrace elevation as a percentage of volcano height, calculated with respect to the basal reference surface of each volcano, derived from the relief values of *Plescia* [2004]. The shaded area on the volcano represents the elevation range in which terraces occur. Note that in some cases, the reference surface may lie above some terraces, resulting in negative percentage values for elevation range minima (**Table 2.2**).

Plate 2.5. An attempt at automatically detecting terrace boundaries on a study volcano, Ascraeus Mons. The points represent points on a Laplacian surface function of the volcano where rates of change of slope meet arbitrary conditions; note that whilst circumferential terrace boundaries are well-defined, the points where terraces meet are less so. This process was ultimately abandoned in favour of manual terrace mapping.

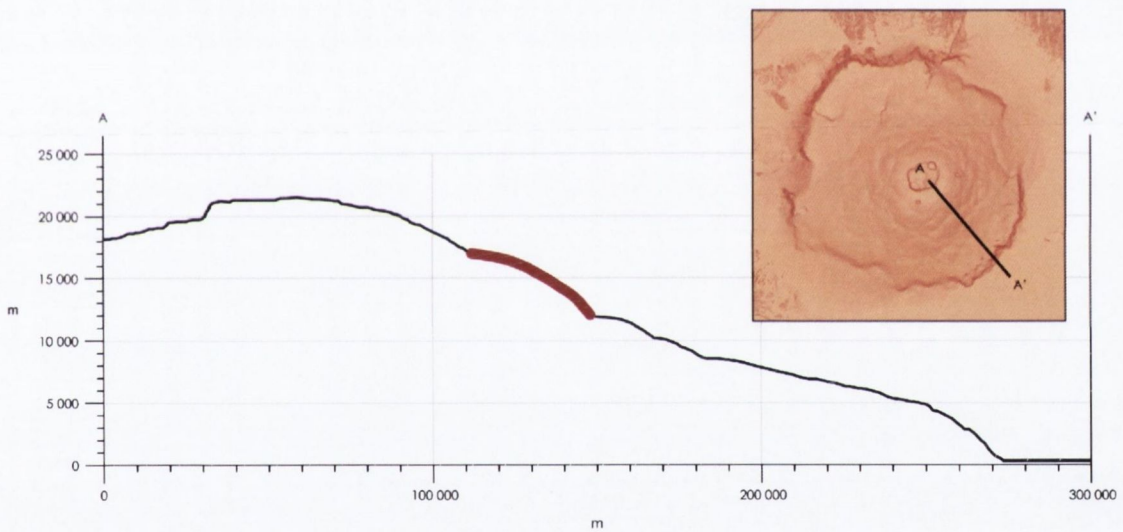

Plate 2.6. The characteristic cross-sectional terrace morphology derived from DTM data. A 5 × vertical exaggeration cross-section taken across the SE flank of Olympus Mons shows the convex-upward terrace profile; a single terrace is highlighted (heavy line). The location of the transect is shown on a slope map of the volcano (inset, top right). This convex-upward profile is consistent with thrust fault morphology.

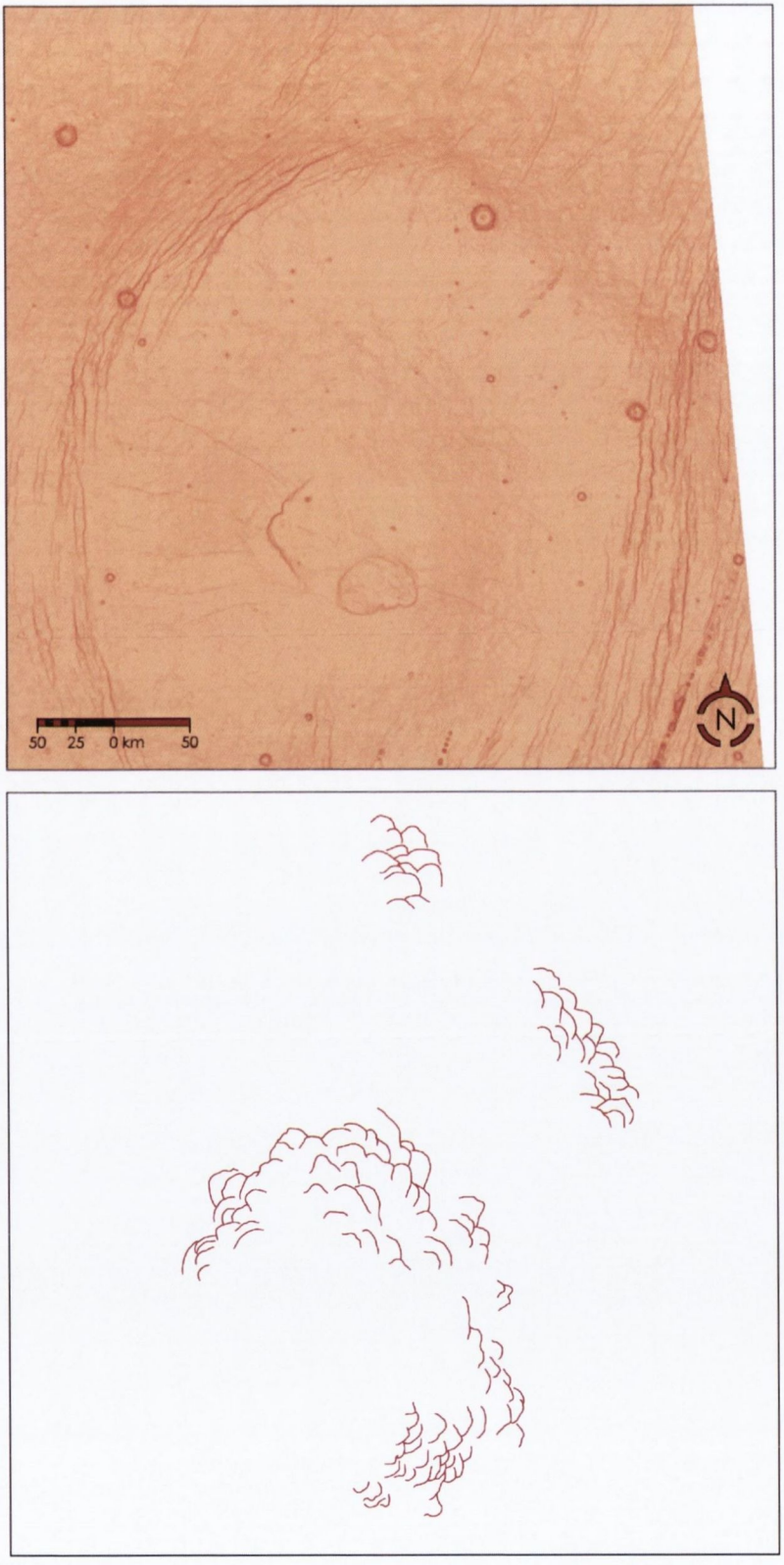

Plate 2.7. The distribution of flank terraces on Alba Patera. The volcano is displayed with its MOLA-derived slope map for reference (top), and its terrace sketch map (bottom). Note the fish-scale imbricate pattern of terracing on this and all subsequent volcanoes. Both the slope and sketch maps are displayed here with a sinusoidal projection. This layout applies to Plates 2.8-2.15, and 2.17, 2.19, and 2.22 (see section 3.3).

Plate 2.8. The distribution of flank terraces on Albor Tholus. Note the graben most prominent on the S and E flanks.

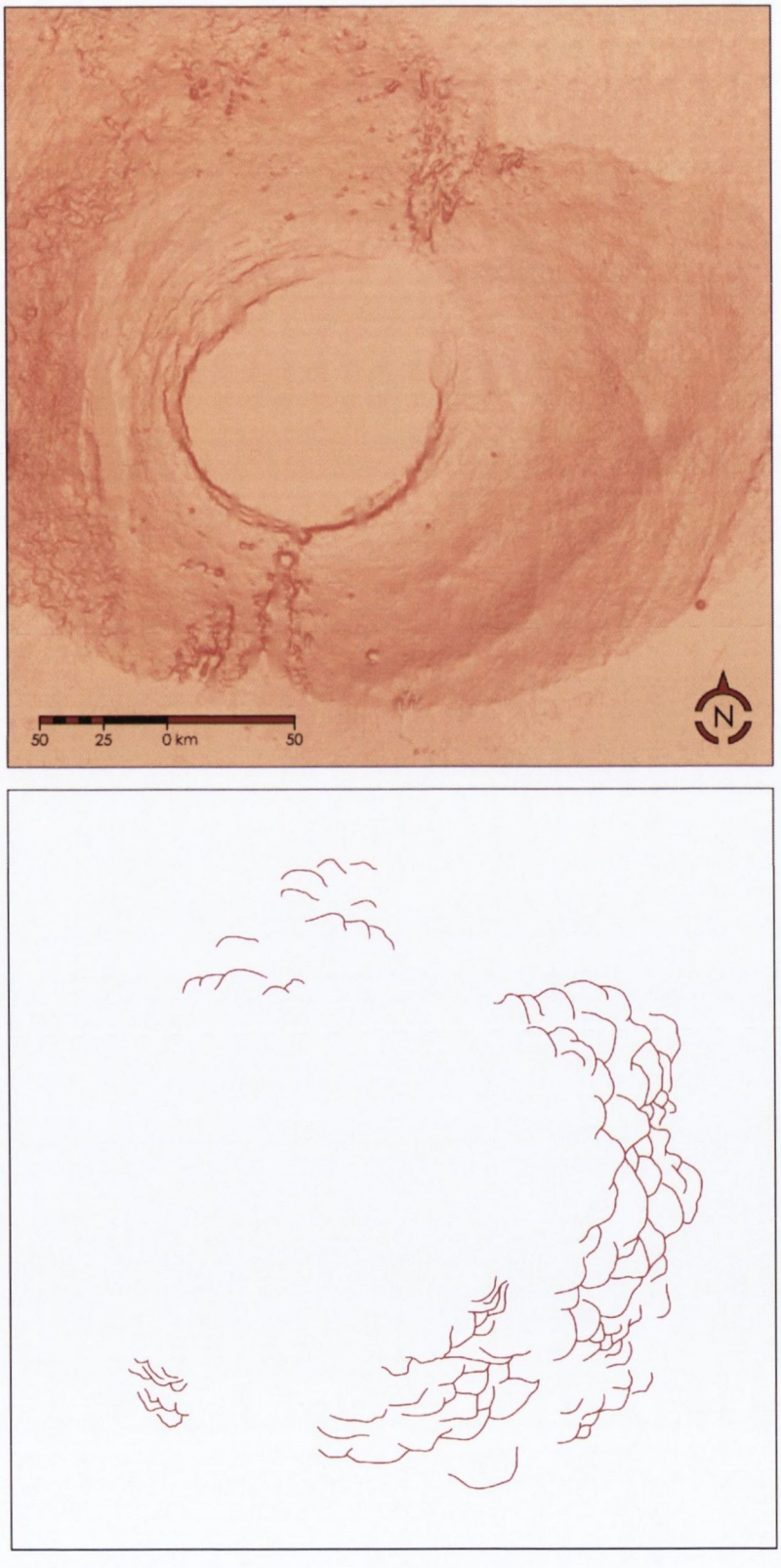

Plate 2.9. The distribution of flank terraces on Arsia Mons. This volcano's caldera is the largest on Mars. The NNW-trending smooth features on the summit and W flank are interpolation artefacts in the MOL data.

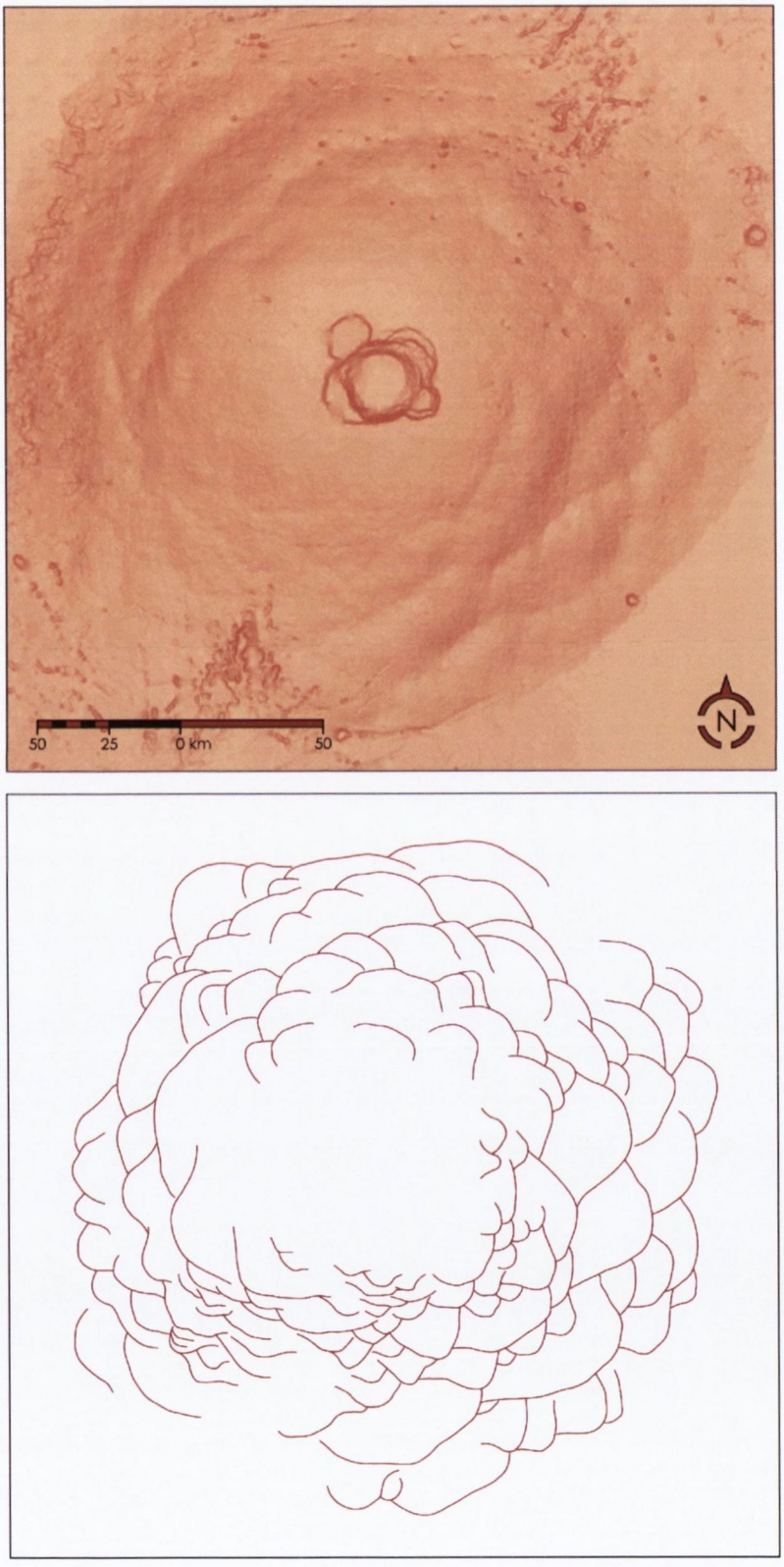

Plate 2.10. The distribution of flank terraces on Ascraeus Mons. The terraces on Ascraeus are amongst the largest and most readily visible of any terraced volcano on Mars.

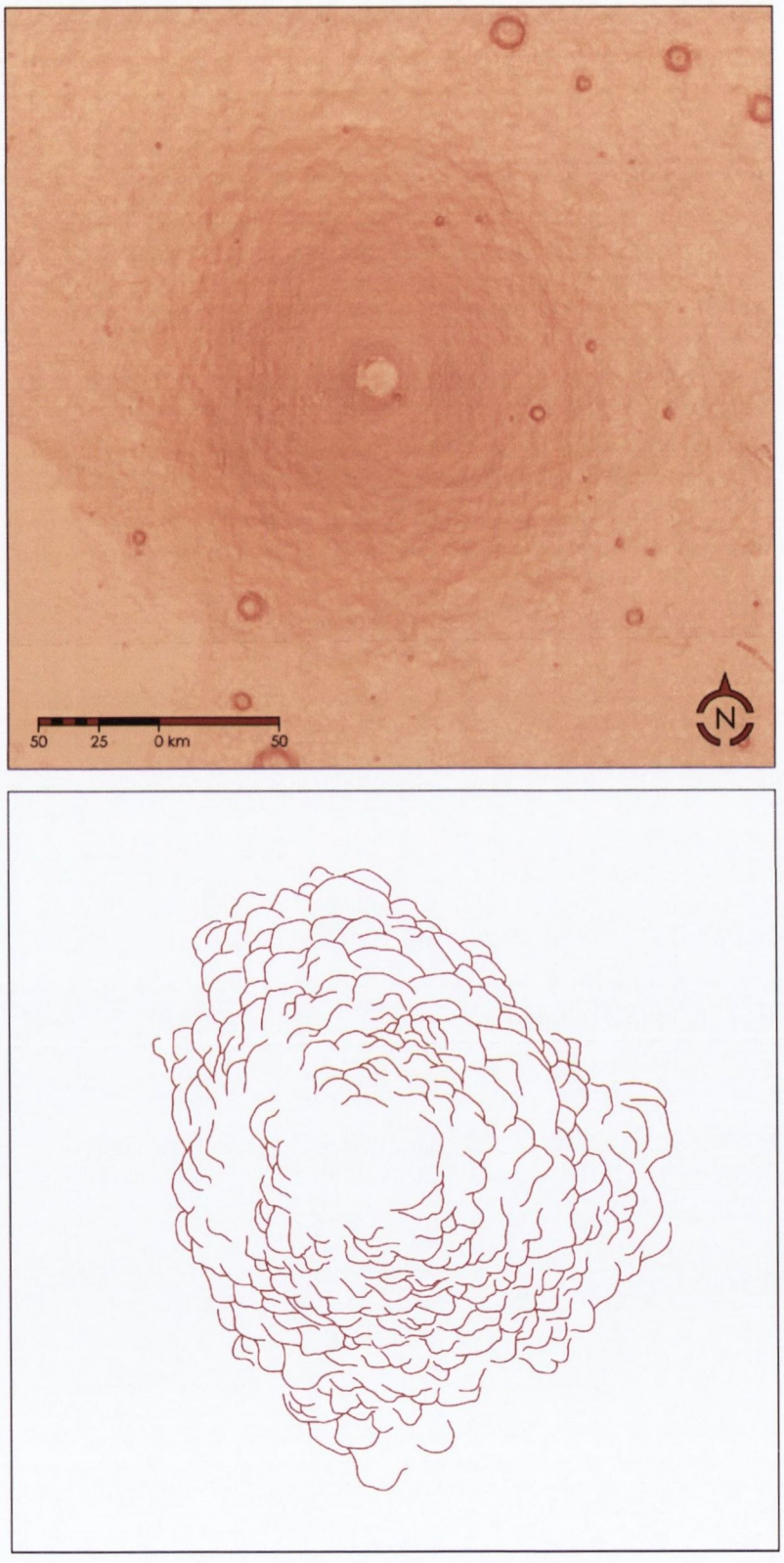

Plate 2.11. The distribution of flank terraces on Elysium Mons. Elysium has the greatest number of terraces of any volcano in this study.

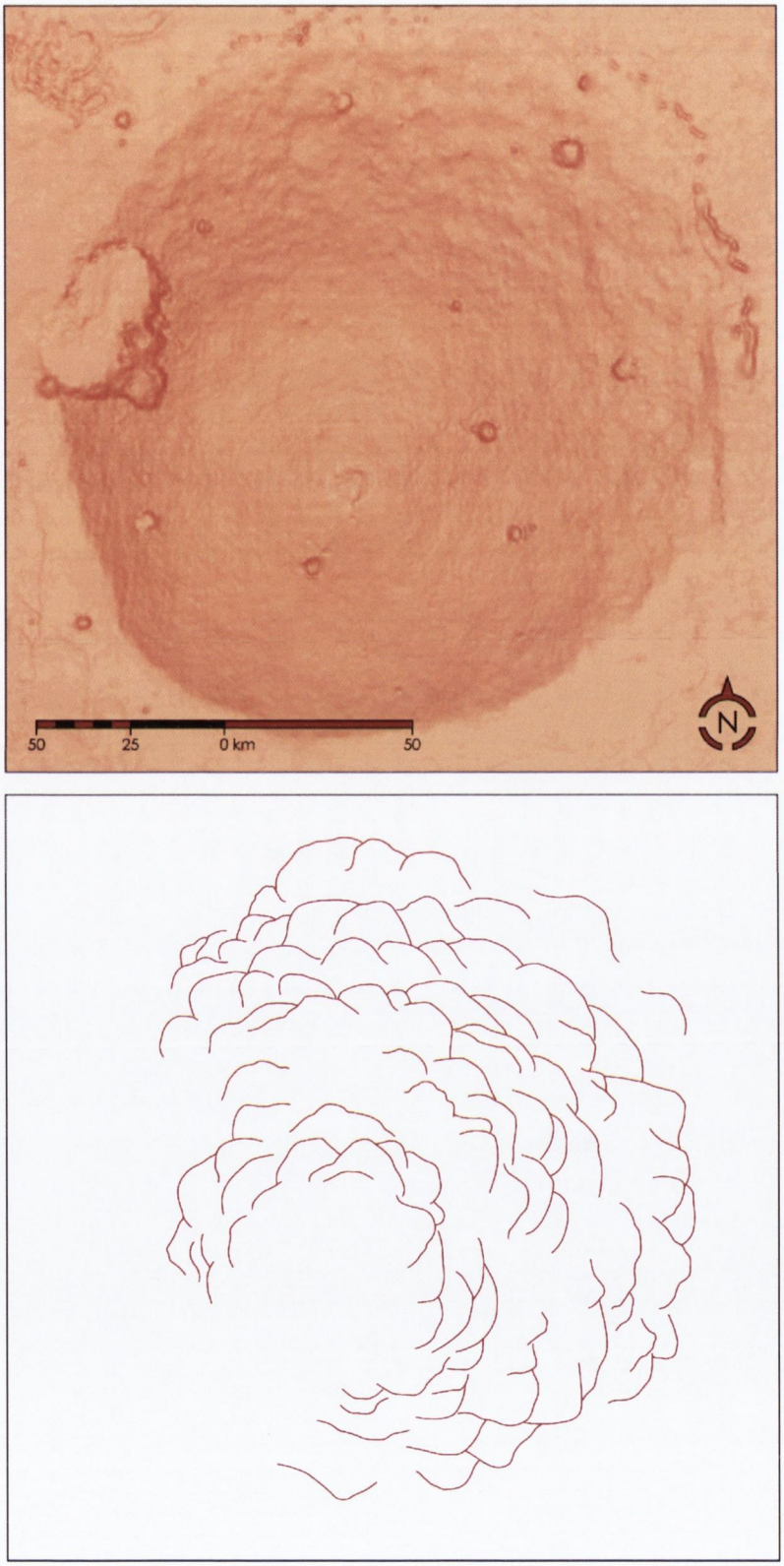

Plate 2.12. The distribution of flank terraces on Hecates Tholus.

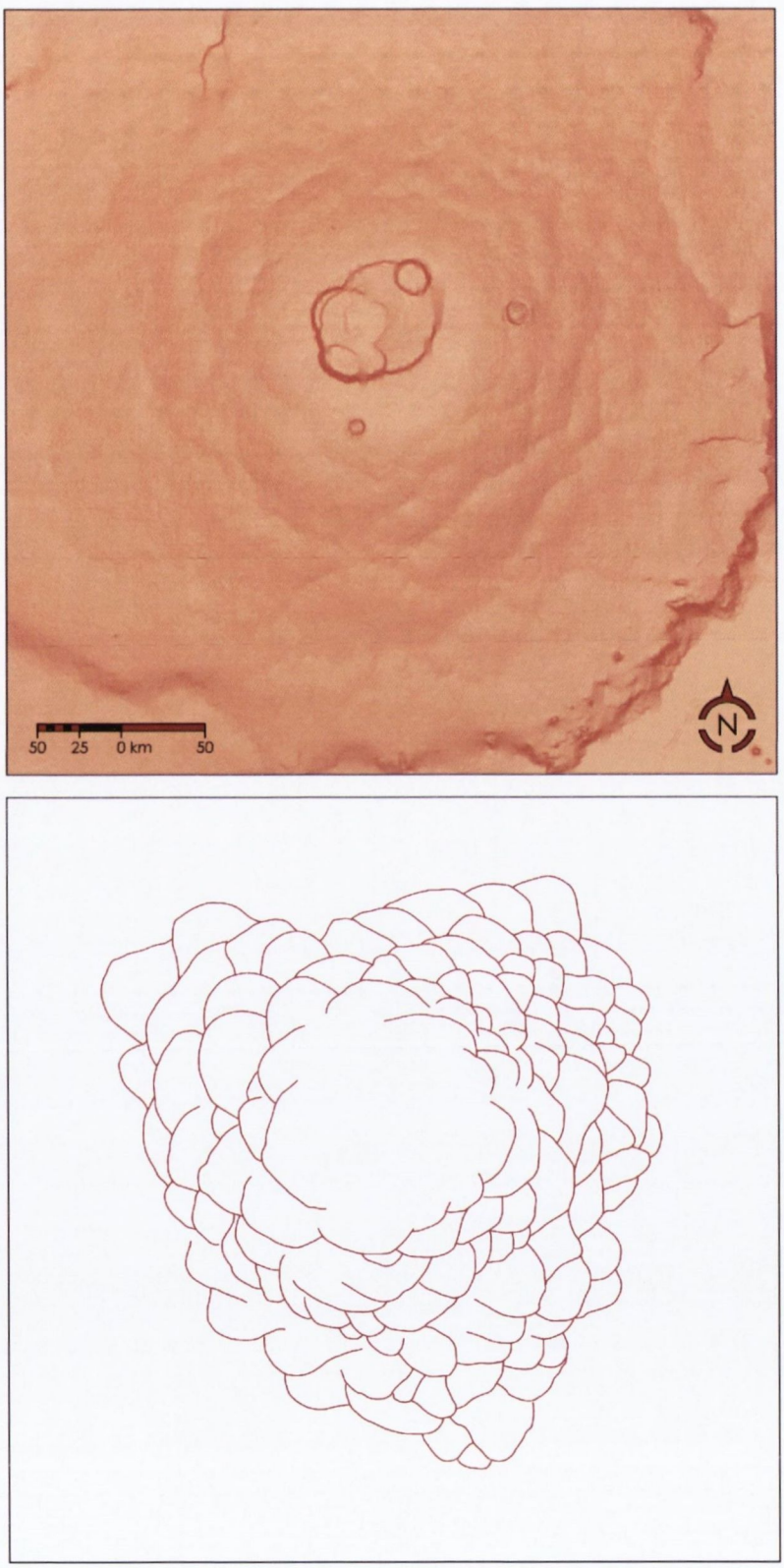

Plate 2.13. The distribution of flank terraces on Olympus Mons. Olympus is the largest volcano on Mars, and, like Ascraeus Mons, has many large, visible terraces on its upper flanks. Note portions of the basal escarpment encircling the volcano in the slope map figure.

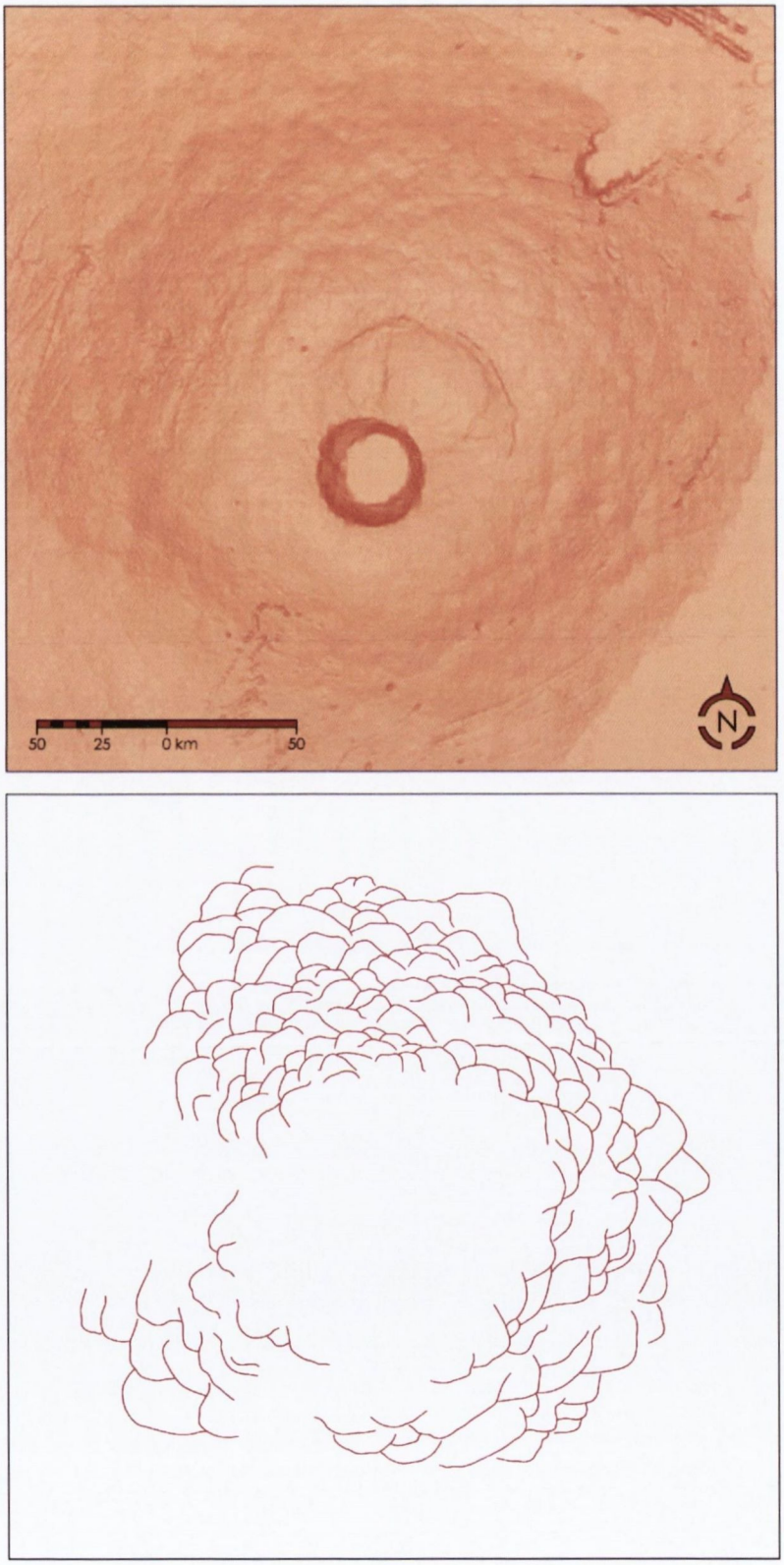

Plate 2.14. The distribution of flank terraces on Pavonis Mons.

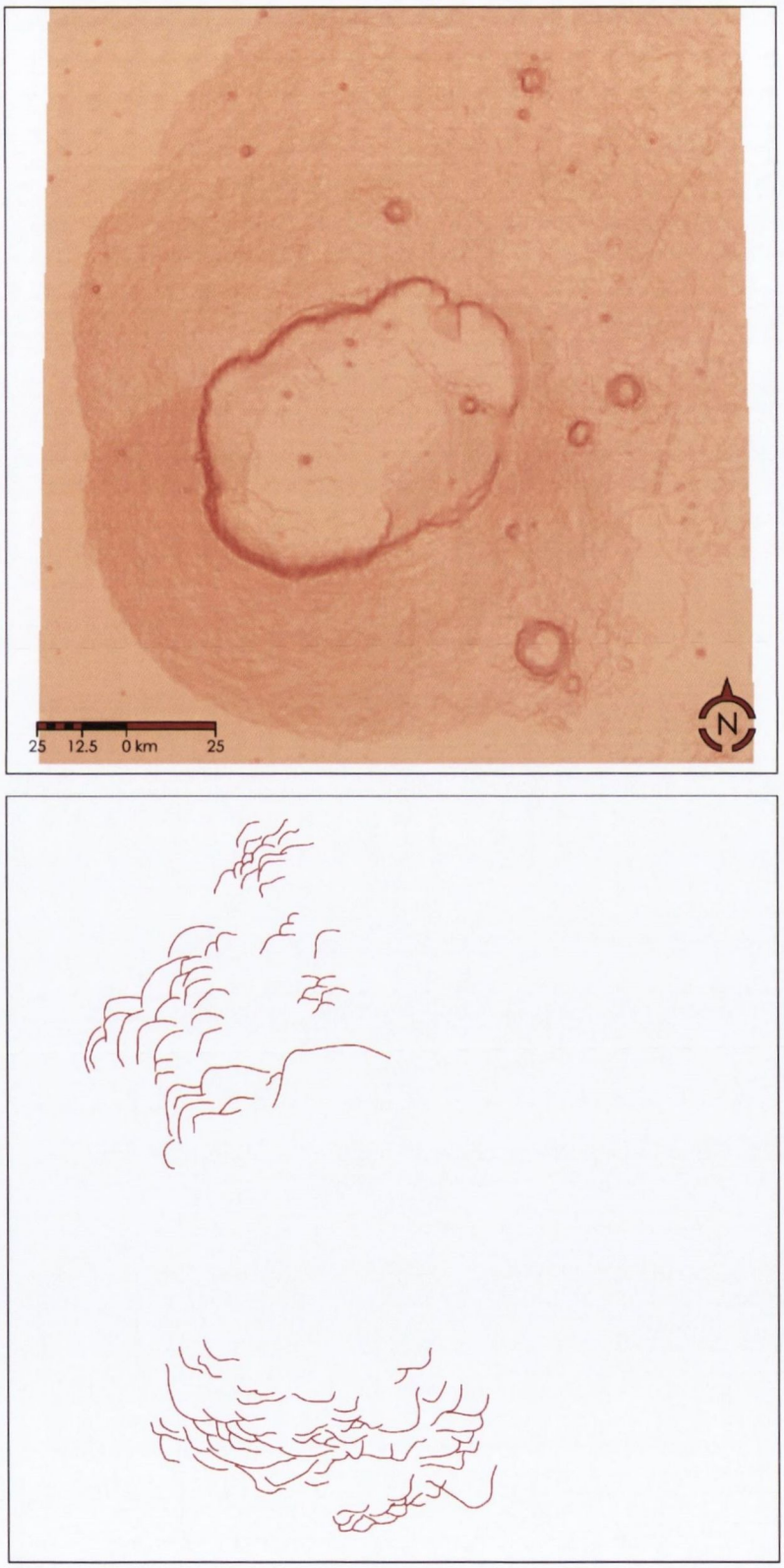

Plate 2.15. The distribution of flank terraces on Uranius Patera.

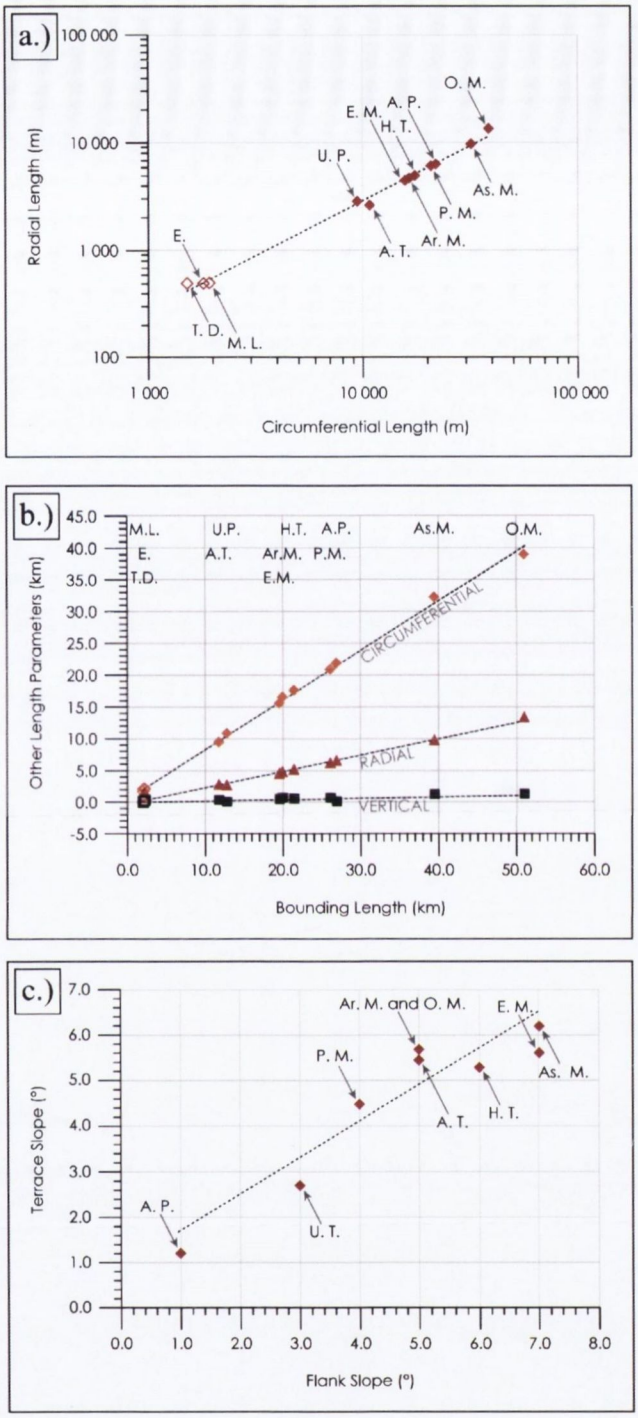

Plate 2.16. Analysis of key terrace morphometric data. Plotted values are averages for each volcano studied. Martian volcanoes are identified as in Plates 1 and 2. Terran volcanoes are identified as such: E. Etna; M. L. Mauna Loa; and T. D. Tendürek Dagi. **a.)** Log-log plot of terrace circumferential length vs. radial length [after *Elliot*, 1976]. The data are described with a power-law distribution; the trend line has the form $y = 0.2504x^{1.0161}$ and has an R^2 value of 0.9935. Note how terraces on the Terran shields follow this distribution. **b.)** Linear plots of terrace circumferential and radial lengths (diamonds and triangles, respectively), and vertical height (squares), vs. terrace bounding lengths. Linear trend lines fit all data on this plot. For bounding length vs. i.) circumferential length: $y = 0.7727x + 0.4386$, $R^2 = 0.9975$; ii.) radial length: $y = 0.2559x - 0.3341$, $R^2 = 0.994$; and iii.) vertical height: $y = 0.0244x - 0.073$, $R^2 = 0.8286$. Again, this morphological relationship holds true for the Terran examples. **c.)** Linear plot of flank slope vs. terrace slope; the data is described by the linear trend line $y = 0.7992x + 0.8925$, with an R^2 value of 0.8448.

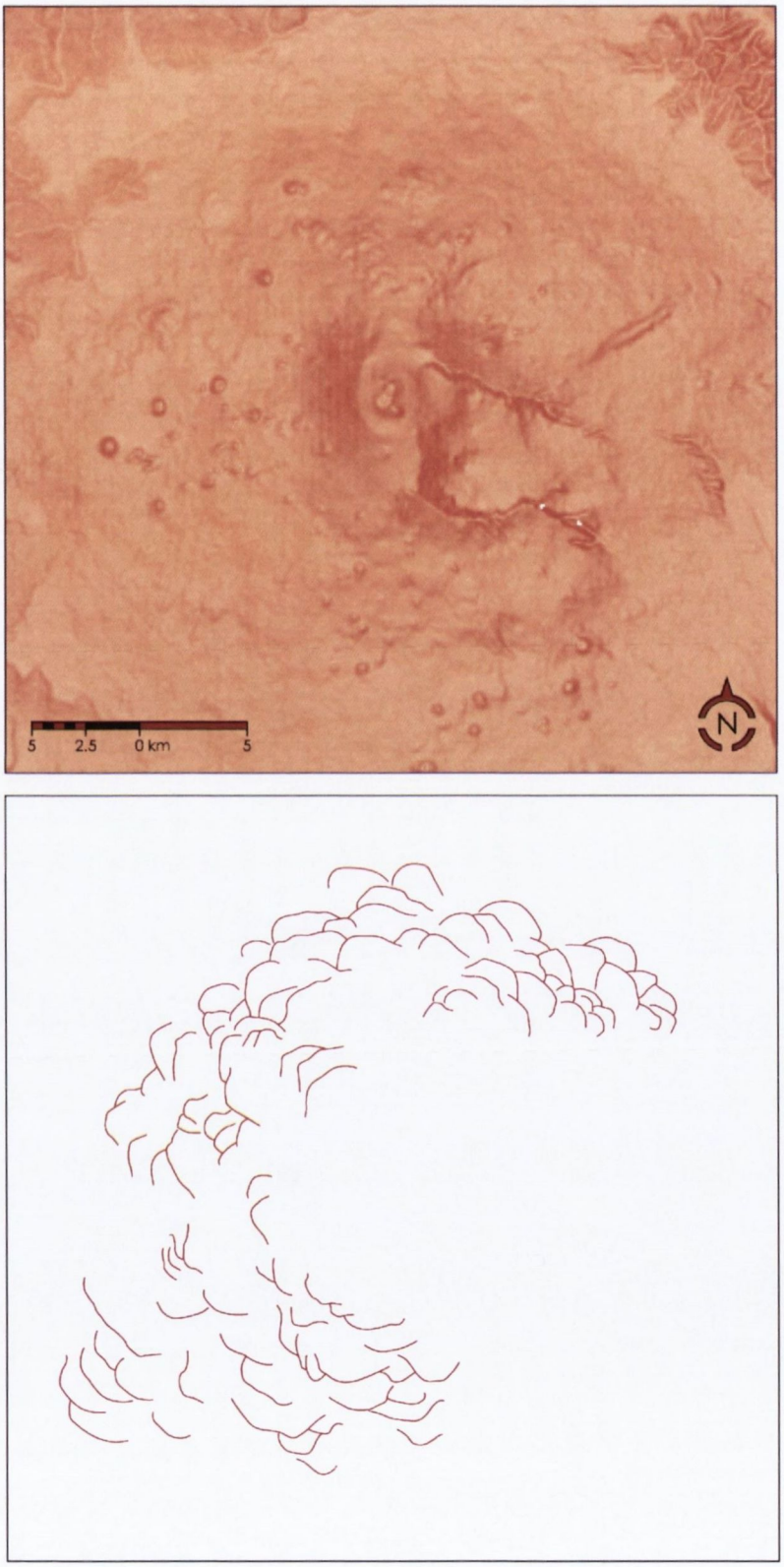

Plate 2.17. The distribution of flank terraces on Etna (Sicily). Note the abundance of parasitic cones on the volcano, located predominantly on the N and S flanks.

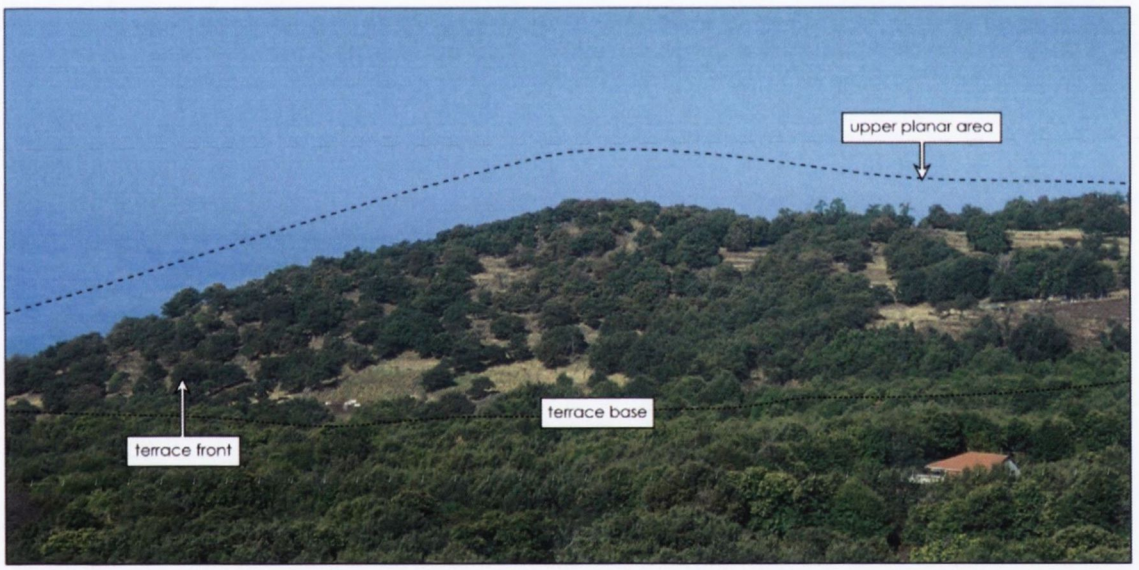

Plate 2.18. Photograph of a terrace-like structure (labelled) on the SW flank of Etna. Note the extensive vegetation and farmland cover, which serves to obscure any localised faulting and associated deformation. The structure is located at approximately 37.67° N, 14.92° E (WGS 84 map datum), and is ca. 1 km away; the image looks W.

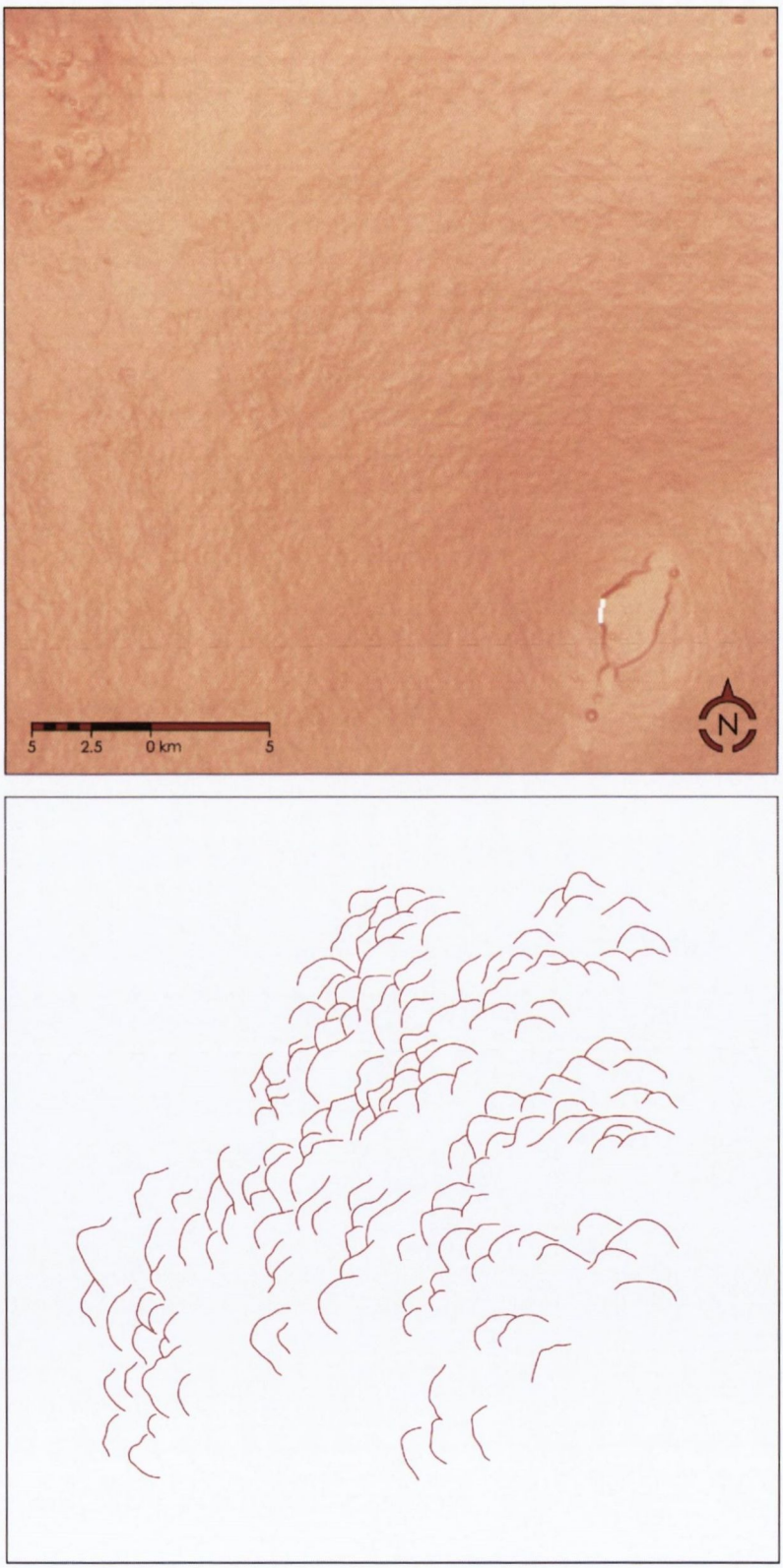

Plate 2.19. The distribution of flank terraces on Mauna Loa (Hawaii). The white mark inside the caldera (bottom right of the slope map) is due to lack of data for those pixels.

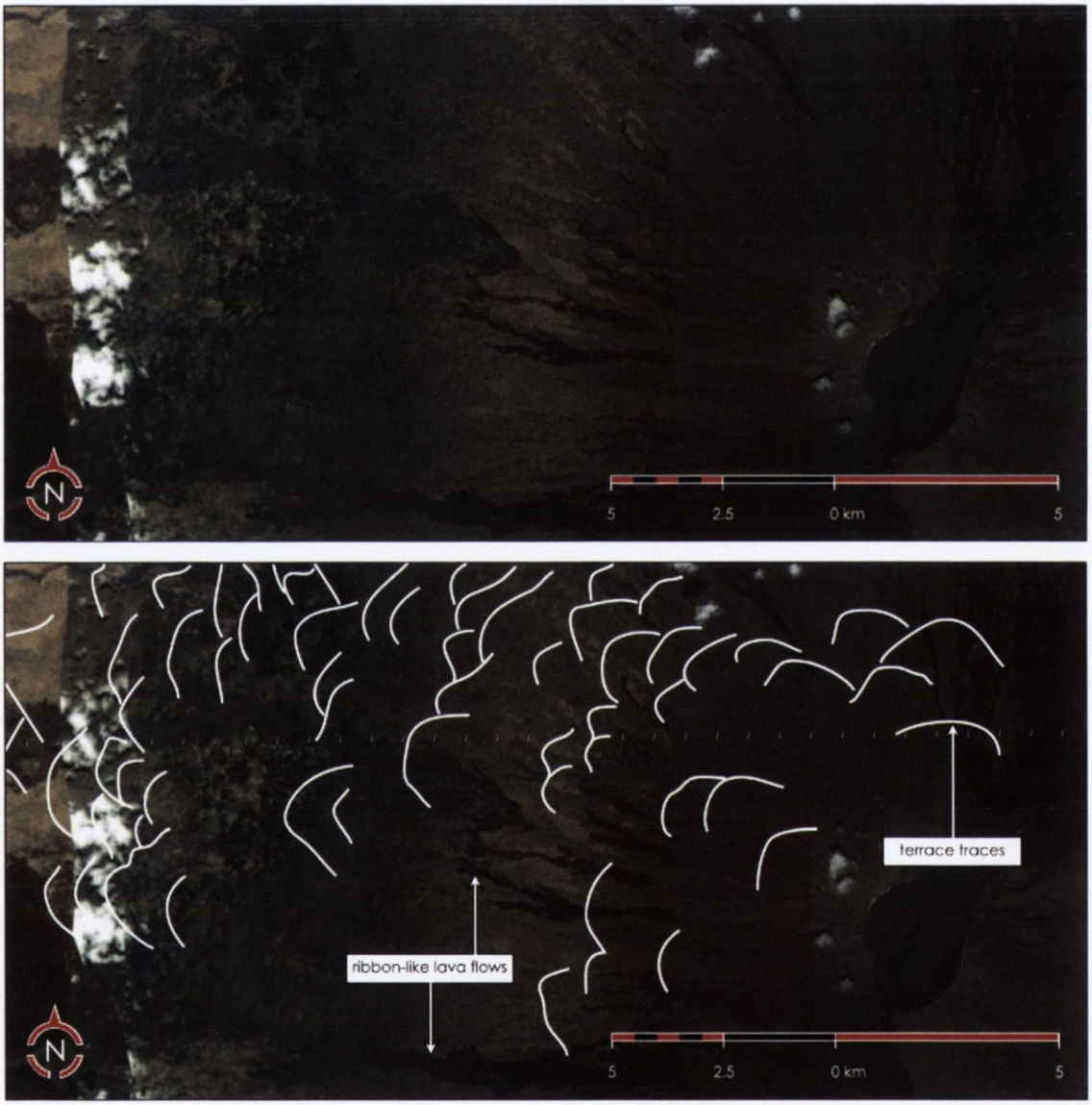

Plate 2.20. Portion of a satellite image mosaic taken from Google Earth™ (data © 2008 DigitalGlobe), showing thin ribbon-like lava flows across the undulating surface of the NW flank of Mauna Loa. In the lower image, both the flows and putative flank terraces are shown and labelled. There is no obvious spatial correlation between the terrace structures and the ribbon-like lavas.

Plate 2.21. Tendürek Dagi (Turkey), viewed from the E99 highway, looking E. The volcano is a stratovolcano located about 55 km SW of Mount Ararat, Turkey's tallest peak. Image credit: www.skimountaineer.com.

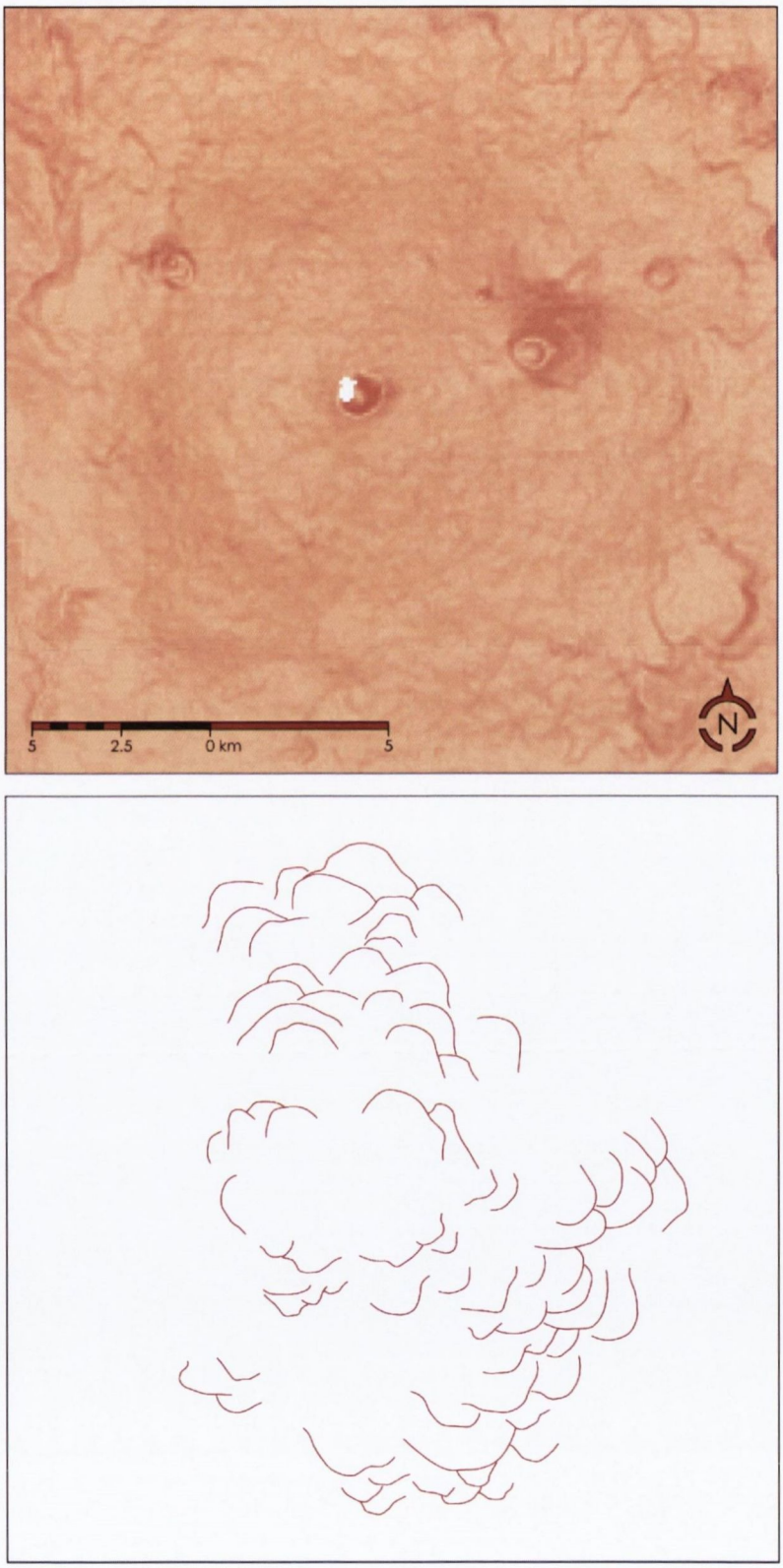

Plate 2.22. The distribution of flank terraces on Tendürek Dagi (Turkey). The white pixels inside the caldera have no elevation values.

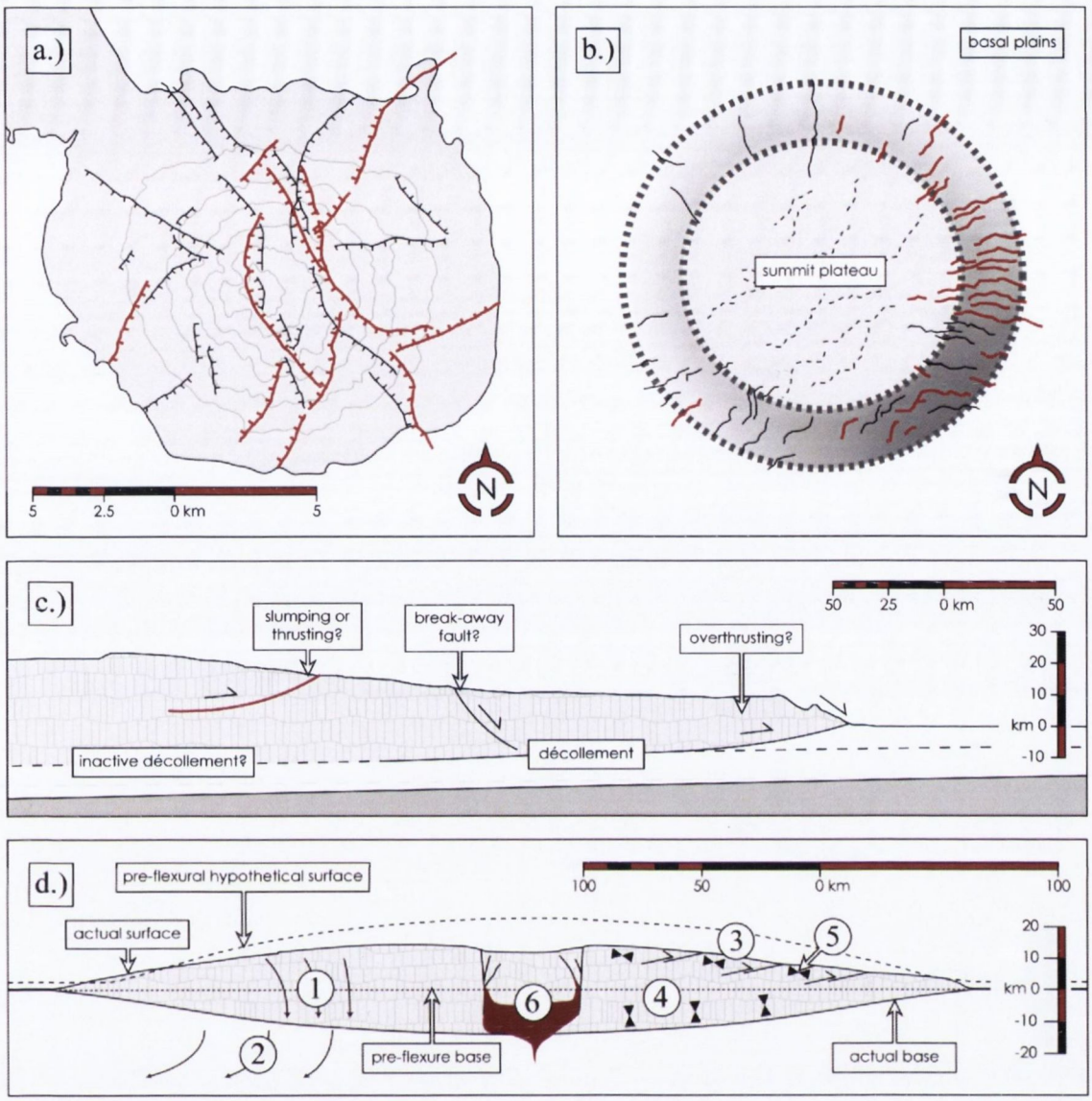

Plate 2.23. The geometry of structures predicted by proposed terrace formation mechanisms. **a.)** Volcano spreading. Simplified structural map of Maderas volcano, Nicaragua, after Fig. 6 of *van Wyk de Vries & Borgia* [1996]. Major normal faults (thick red lines) cut across the edifice to form leaf graben and crescent half-graben; minor associated faults are also shown (thin lines). Ticks indicate downthrown side. Contour lines have 200 m intervals. **b.)** Magma chamber tumescence, after Fig. 3a of *Marti et al.* [1994]. The predominant structure is an axisymmetric dome, the base and summit plateau of which are marked (heavy dotted lines), and which is bounded by blind concentric faults (not shown). Sub-radial tension fractures are drawn with heavy solid lines, while smaller fractures are shown with lighter solid lines. Irregular faults that delimit the central depression are shown with a dashed stroke. Scale not given in the original figure. **c.)** Shallow slumping. Simplified sketch map of possible volcanotectonic structures within Olympus Mons, after Fig. 10c of *Morgan and McGovern* [2005]. Significant structural features are shown, including a hypothesised inward-dipping fault plane (heavy line), along which thrusting may occur due to lateral flank spreading. Sketch is shown here with a 1.43 × vertical exaggeration. Note that this figure features lithospheric flexure (evinced by the slight bending of the base of the edifice) in a scenario where lithospheric thickness is very high (T_e > 70 km), and so illustrates a scenario where spreading and flexing occurs together. The flexural wavelength is long. **d.)** Lithospheric flexure (solely). Stylised diagram of Ascraeus Mons undergoing lithospheric flexure. The volcano's actual surface (from a NW-SE MOLA transect) and base, and hypothesised pre-flexure surface and base, are shown. Processes at work as the volcano flexes are highlighted: (1) inward and downward displacement of volcano during flexure resulting in constriction; (2) flow or flexure of viscoelastic lithosphere; (3) near-surface thrusts and undulations forming flank terraces; (4) σ_1 ~vertical due to load; (5) σ_1 low-angle due to constriction. The magma chamber is also shown (6). Sketch is shown with no vertical exaggeration (though the extent to which the base of the edifice has bowed is uncertain). This model assumes that T_e is very low, and may represent a case with massive plastic yielding at the flexural bulge. In this model, the flexural wavelength is long.

morphometric data for Martian shield volcanoes

Volcano	Edifice Size (km)	Base Elevation (m)	Summit Elevation (m)	Relief (m)	Volume (m^3)	Flank Slope (°)	Latitude	Longitude
Alba Patera	1,015 × 1,150	1,049	6,849	5,800	1.8×10^{15}	1.0	40.6	-110.0
Albor Tholus	157 × 164	-269	3,931	4,200	2.9×10^{13}	5.0	19.0	150.2
Arsia Mons	461 × 326	6,076	17,776	11,700	9.2×10^{14}	5.0	-9.5	-120.5
Ascraeus Mons	375 × 870	3,350	18,250	14,900	1.1×10^{15}	7.0	11.1	-104.2
Elysium Mons	375 × 375	1,513	14,113	12,600	2.0×10^{14}	7.0	24.5	146.7
Hecates Tholus	177 × 187	-1,746	4,854	6,600	6.7×10^{13}	6.0	31.5	150.0
Olympus Mons	840 × 640	-610	21,290	21,900	2.4×10^{15}	5.0	18.3	-133.2
Pavonis Mons	380 × 535	5,664	14,064	8,400	3.9×10^{14}	4.0	1.1	-122.6
Uranius Patera	242 × 280	1,955	4,955	3,000	3.5×10^{13}	3.0	26.5	-92.8

Table 2.1. Morphometric data for the nine Martian volcanoes studied. Values for edifice size, relief, volume, and flank slope are from *Plescia* [2004]. Volumes and sizes are calculated with respect to a reference surface for each volcano, which is typically the topographically lower change in slope of that edifice. Summit elevation values are taken from the MOLA dataset [*Smith et al.*, 2001], and are relative to the IAU2000 definition for Mars. Base elevations are then calculated from the relief values of *Plescia* [2004]. Latitude and longitude values are adapted from *Crumpler et al.* [1996], and are given here relative to a coordinate system with a centre of longitude of 0°.

terrace morphometric data for Martian volcanoes

Volcano	Number	Bounding Length (km)	Circumferential Length (km)	Radial Length (km)	Vertical Height (m)	Slope (°)	Elevation (m)		Elevation Range (%)	
							min.	max.	min.	max.
Alba Patera	127	27.0	21.6	6.3	128	1.2	931	5,907	-2	84
Albor Tholus	122	11.9	9.4	2.8	258	5.5	-74	3,381	5	87
Arsia Mons	115	20.0	16.3	4.6	459	5.7	8,289	16,834	19	92
Ascraeus Mons	142	39.6	31.9	9.6	1,084	6.2	3,874	17,300	4	94
Elysium Mons	264	19.7	15.8	4.5	415	5.6	2,176	11,362	5	78
Hecates Tholus	103	21.5	17.5	5.0	454	5.3	-3,561	3,858	-28	85
Olympus Mons	118	51.2	38.7	13.4	1,307	5.7	6,378	20,676	32	97
Pavonis Mons	167	26.2	20.8	6.2	487	4.5	6,080	13,457	5	93
Uranius Patera	121	12.8	10.8	2.6	115	2.7	1,614	4,071	-11	71

Table 2.2. Terrace morphometric data for the nine Martian volcanoes in this study, acquired according to the methods described in section 2.3 of the text. The terrace number is the total number of unequivocal terrace structures mapped per volcano. Bounding, circumferential, and radial length values are rounded to the nearest hundred metres. Vertical height and elevation minima and maxima values are given to the nearest whole metre. Slope values to the first decimal point are presented. Elevation minima and maxima values are relative to the IAU2000 definition for Mars. Elevation percentage ranges are calculated according to the relief values from *Plescia* [2004].

terrace morphometric data for Terran volcanoes

Volcano	Number	Bounding Length (km)	Circumferential Length (km)	Radial Length (km)	Vertical Height (m)	Slope (°)	Elevation (m)		Elevation Range (%)	
							min.	max.	min.	max.
Etna	107	2.3	1.8	0.5	83	9.6	625	1,964	-11	44
Mauna Loa	150	2.3	1.9	0.5	55	6.0	1,397	3,685	-29	76
Tendürek Dagi	77	2.0	1.5	0.5	61	7.2	2,388	3,191	-61	53

Table 2.3. Terrace morphometric data for the three Terran volcanoes in this study. The values here have been acquired as per those in **Table 2**. Elevation minima and maxima values are relative to the WGS 84 reference system for Earth.. Elevation percentage ranges are calculated from relief values in the SRTM data.

introduction

nature | origin | context

conclusions

3 On the formation, development, and structure of flank terraces using scaled analogue modelling techniques.

overview

Of the formation mechanisms proposed for flank terraces, lithospheric flexure is the strongest candidate. Terrace morphology matches that of thrust faults, structures predicted to form on a volcano as it undergoes flexure, whilst terraces are distributed in a manner consistent with a net reduction in surface area. However, flank terrace geometry has not been comprehensively described before, so previous studies have been unable to effectively assess terrace formation hypotheses.

Scaled physical (analogue) modelling techniques can aid in determining whether lithospheric flexure is in fact capable of producing flank terraces, and through varying key parameters can account for differences in volcano structure, geometry, and location. Sand cones placed upon silicone putty reservoirs and allowed to passively sink develop a suite of structures that systematically characterise lithospheric flexure, including a flexural depression, annular extension, and a circumferential trough. Foremost among these structures, however, is a set of surface convexities on the cone flanks which have a convex-upward, outward-verging morphology, and a fish-scale, imbricate distribution pattern. These model terraces are the surface expressions of inward-dipping thrust faults that form due to inner-arc shortening as the cone flexes.

Using DTM and photogeological data, it is possible to relate these and the other flexural structures to natural analogues on Mars. Due to the morphological similarities between the laboratory and real-world terraces, and the presence of other flexure-induced features on Mars, I argue that lithospheric flexure is the mechanism responsible for the formation of volcano flank terraces.

1. lithospheric flexure

On differentiated planets, the lithosphere generally consists of the brittle crust and upper mantle, situated above the asthenosphere, the ductile lower mantle. Excess loading by mass concentrations (mascons) or volcanoes leads to flexure of the lithosphere, resulting in the formation of an outer rise and an inner trough and, for sufficiently large loads, to stresses capable of fracturing the lithosphere [*Comer et al.*, 1985]. The response of the lithosphere to loading depends strongly on its flexural rigidity and thus thickness, T_e, and so most studies of the distribution of lithospheric stresses focused on determining this value. Determining the thickness of a planet's lithosphere provides important information on its thermal and chemical evolution.

Flexure may take place within the crust, if the rock is weak enough to flow under loading. This is the case for Earth, where thick sedimentary basins allow flexure into superficial rocks, or where the lower crust can respond in a ductile manner due to high heat flow. On Mars, thick sediments may not be present, but ice present in the upper crust could allow localised shallow flexure [cf. *Murray et al.*, 2010] (though the extent to which this type of subsidence will affect an edifice is

uncertain), whilst the lower crust might have been ductile at some stage in Martian history [*Watts*, 2001].

The effects of crustal loading on Earth have been extensively examined, e.g. flexure beneath the Hawaiian ridge [*Gunn*, 1943]. The availability of photogeological data for the Moon [*Melosh*, 1978] and Mars [*Thurber and Toksöz*, 1978] extended these studies beyond Earth. To calculate T_e, loading of a lithosphere is essentially regarded as the bending of an elastic plate whose flexural rigidity, D, is given as

$$D = E(T_e)^3 \times (12(1-v^2))^{-1}, \quad (1)$$

where E is the plate's Young's modulus, T is the plate thickness, and v is its Poisson's ratio [*Engelder*, 1993]. Observations such as the radial distances to a major load of surface fractures that satisfy a set of criteria for origin by flexure provide data which can be used to constrain D [*Comer et al.*, 1985].

For a detailed overview of the mechanics of lithospheric flexure, the reader is directed to *Engelder* [1993, p. 383 – 391] and *Middletown and Wilcock* [1994, p. 271 – 280]. In simple terms, however, lithospheric loading can be thought of in terms on an elastic (two-dimensional) plate of thickness *t* and length *l* undergoing flexure due to a line load. The plate experiences lengthening along its outer surface (**Plate 3.1: 1**), whilst its inner surface is shortened (**Plate 3.1: 2**). The neutral surface, the plane between the lengthened and shortened portions of the plate, is folded without changing length (**Plate 3.1: 3**). The plate can respond to this bending by simple orthogonal buckling, flexural shear, or flexural slip. Relative deformation remains the same in each case, but strain is concentrated around the hinge when a plate buckles, and on the limbs of the folded plate during flexural shearing or slip.

Flexural bending has implications for geological systems. The localised flexural response of the Terran lithosphere to loading of material eroded from mountain chains can influence the shape and extent of sedimentary basins, affecting their economic value [*Walcott*, 1972]. Magma ascent can be arrested by high compression within the inner arc of a flexed plate, such as that below Hawaii, leading to underplating [*McGovern and Solomon*, 1993; *McGovern*, 2007]. Additionally, flexure may also influence the state of stress within a volcano, affecting its volcanic and tectonic development; this is explored in greater depth in Chapter 4.

2. methodology

The basic approach of this work was to simulate flexure of the Martian lithosphere; using a set of simple, scaled physical models which featured two contrasting rheologies, a brittle cone induced a

load upon a ductile substratum and underwent deformation. Resultant structures were then recorded, analysed, and compared to those observed on Mars.

The modelling work was divided into two experimental programmes: one qualitative, the other quantitative. The qualitative programme investigated the effects of flexure upon a simple loading model, whose parameters were then varied to reflect a variety of real-world geometrical and rheological conditions. The shorter quantitative programme was used to measure a set of geometric values for several representative experiments and to calculate the amount of strain present in each so as to identify the orientation and magnitude of the principal strain axes.

Where possible, the model were scaled to known values for Mars (see section 2.3), but key parameters including volcanic effusion rates and the viscosity of the planet's lower crust remains as yet unconstrained. Coupled with uncertainty as to the material properties and internal layering of Martian volcanoes, these experiments likely represent a simplification of the reality. Nonetheless, this work explores a range of possible geometries and materials, and provides a first-order examination of the flexural process on Mars.

2.1 analogue materials

Fine (~300 μm mean grain diameter) aeolian quartzose sand served as a granular analogue to Martian volcanic products and the planet's upper lithosphere. When mixed in a 10:1 ratio with powdered gypsum to increase its cohesion, the material had a bulk density of approx. 1,400 kg m^{-3}, an internal friction angle of 33°, and a cohesion of about 10–20 Pa [after *Donnadieu*, 2000]. A transparent silicone putty (commercially produced by Dow Corning® as Silastic SGM 36) simulated the lower, viscoelastic lithosphere, as well as magmatic intrusions (see 2.4.2). Mixed with <1% by weight of quartzose sand, the gel also had a bulk density of ca. 1,400 kg m^{-3}, and a viscosity of 10^4 Pa s at experimental conditions.

Dry sand is a suitable analogue for brittle rock as it satisfies the Navier-Coulomb failure criterion [*Hubbert*, 1951], and has been used in laboratory studies to represent both volcanic products [*Merle and Borgia*, 1996; *Walter and Troll*, 2001] and upper crustal lithologies [*Holohan et al.*, 2004; *Girard and van Wyk de Vries*, 2005]. The use of silicone to simulate incompetent material is also precedent in analogue modelling, ranging from magma chambers [*Roche et al.*, 2000] and sills and dykes [*Mathieu et al.*, 2008], to low-strength layers (LSLs) [*Oehler et al.*, 2005] and ductile substrata [*van Wyk de Vries and Matela*, 1998].

Other materials were also tested for their suitability in these experiments. A higher viscosity silicon gel (ca. 10^5 Pa s) behaved similarly to the 10^4 Pa s putty but over proportionally longer timescales, and was discarded for practical reasons. Different model cone cohesions were investigated using other granular materials, including coffee and chocolate powders, iron filings,

and crushed ignimbrite. These substances proved difficult to utilise and/or recycle, however, and were rejected in favour of dry sand.

2.2 experimental procedure

The experimental setup for simple loading is detailed here. Where experimental parameters (e.g. cone geometry; see 2.4.3) are modified, addenda to this experimental procedure are given in the relevant sections. Experimental cross-sections are illustrated in **Plates 3.2** and **3.3**.

The experimental apparatus consisted of a circular container (to minimise any potential edge effects) 48 cm in diameter, into which a large reservoir of silicone typically 80 cm deep was placed (**Plate 3.2: 1**). A conical load of sand was then poured directly upon the silicone, to a predetermined circumference inscribed upon the gel's surface (**Plate 3.2: 2**). The cone was smoothed by sieving more sand onto its flanks. After construction, its flanks and the surrounding surface were covered by a thin (<1 mm) layer of sieved gypsum plaster to preserve any small-scale deformation that might form (**Plate 3.2: 3**).

The silicone responded to the cone's weight almost immediately, often manifesting a flexural depression before delivery of the sand was complete. To ensure the entire load was present before the onset of flexure, delivery times were restricted to less than 60 s. Cone emplacement was therefore effectively instantaneous, corresponding only to the very fastest effusion rates theorised for Mars [e.g. *Plescia*, 2004].

All experiments were incrementally photographed from plan view; low-angle illumination highlighted any subtle deformation that occurred. In most cases, structures had formed within 600 s, and no new surface strain was apparent after 1,200 s. Upon completion each experiment was excavated and the resultant flexural bowl also photographed.

2.3 scaling

Material properties and forces in these experiments should geometrically and dynamically scale to nature [*Hubbert*, 1951; *Ramberg*, 1981] (**Table 3.1**). The scaling ratio for any physical property is defined as

$$X^* = X_{model} \times (X_{nature})^{-1}. \quad (2)$$

The length ratio is the geometric scaling factor for these experiments ($l^* = l_{model} \times (l_{nature})^{-1}$), and is 10^{-5}; a model radius of 12.5 cm therefore represent a volcano 250 km in diameter, representative of a medium-sized shield volcano on Mars, e.g. Uranius Patera (see Chapter 2, Table 2.1). The dynamic scaling factor is the stress and cohesion ratio, and is given by

$$\sigma^* = l^* \times g^* \times \rho^*, \quad (3)$$

where l^* is the length ratio, g^* the acceleration due to gravity ratio, and ρ^* the density ratio. g is defined on Earth as 9.81 m s^{-2}, whilst on Mars it is 3.8 m s^{-2}; g^* is thus 2.58. The density of the materials used in these experiments is approx. 1,400 kg m^{-3}, and is assumed to be ca. 2,600 km g^{-3} on Mars, so ρ^* is 5.38×10^{-1}. The stress ratio, from (2), is therefore 1.39×10^{-6}. For a reference cohesion on Mars of 1×10^7 kg m^{-2} s^{-2} (Pa), the models should have a cohesion of 1.39×10^1 Pa, equivalent to the low-cohesion sand used.

The behaviour of Coulomb materials is theoretically independent of time, but the deformation of a ductile material is not rate-independent. A time ratio, T^*, is required, and can be calculated as

$$T^* = \sigma^* \times \mu^*, \quad (4)$$

where σ^* is the stress and cohesion ratio, and μ^* the viscosity ratio. The viscosity of the silicone used in the experiments is 10^4 Pa, but the viscosity of the Martian crust is unknown. However, assuming it is composed largely of mafic lithologies [e.g. *McSween et al.*, 2003], a value of 10^{20} Pa is reasonable [cf. *Girard and van Wyk de Vries*, 2005, and references therein]. μ^* is thus 1×10^{-16}, and gives a time ratio of 7.19×10^{-11}.

The time taken for structures to develop in these experiments, ca. ten minutes, is therefore equivalent to 300,000 years. This is a very short time for deformation to occur with respect to the accepted ages of Martian volcanoes [*Plescia and Saunders*, 1979], and is contingent on the viscosity parameter chosen for the ductile Martian crust. If the choice of viscosity value is correct, then flank terraces should form rapidly on volcanoes that were largely built before crustal flexure could begin. The possible viscosity range is extremely wide, however, and the temporal scaling factor is not well constrained. Nevertheless, the geometric and Navier-Coulomb variables for brittle deformation are well-scaled, so geometric and structural features should be correctly modelled.

2.4 qualitative experimental programme (QIX.)

This programme consisted of 56 experiments grouped into six sets (**Table 3.2**). The first set, simple loading, established a characteristic set of flexure-induced structures; the remaining five sets examined how these structures developed in response to a varied set of parameters. No measurements were taken in these experiments; instead they provide a qualitative basis for understanding the flexural mechanism. The experimental parameters for each experiment are given in **Appendix II.I**.

2.4.1 set A: simple loading

These experiments were performed as per section 2.2, and were intended simply to examine the effects of flexure upon a homogenous cone at the angle of repose. This series served as a control, absent of any parameter variations, against the results of which more complicated experiments could be compared. The experimental setup is illustrated in **Plate 3.2**.

2.4.2 set B: silicone inclusions

Volcanoes are often heterogeneous constructs, with materials of different competencies throughout. Poorly consolidated deposits [*Borgia et al.*, 2000], LSLs [*Oehler et al.*, 2005], intrusive complexes [*Borgia*, 1994], and structures like basal décollements and rift zones [*Morgan and McGovern*, 2005] undermine volcano stability and complicate the makeup of a volcano. The structural similarity of Martian volcanoes to those on Earth [e.g. *Crumpler et al.*, 1996] suggests these compositional characteristics equally apply to Mars.

Discrete bodies of silicone putty were included in these experiments, added to the sand cones during construction (**Plate 3.3a**). Tabular, conical, and sheet-like inclusions replicated features including magma chambers, intrusive cores, and LSLs. Experiments QlX. B 01-07 were performed on table tops; QlX. B 08-14 were carried out upon silicone reservoirs. Whilst comprehensive, this set was not designed to be exhaustive but rather to demonstrate the effect of ductile zones within an otherwise competent cone.

2.4.3 set C: cone geometry

Cone geometry was varied to assess the effects of flexure upon different load shapes and sizes, reflecting the range of volcano morphologies on Mars [*Hodges and Moore*, 1994]. Cone width was used as a proxy for volume; loads with diameters of 12 cm and 25 cm were modelled (**Plate 3.3b: 1, 2**). As terraced volcanoes can differ considerably in size (see Chapter 2, Table 2.1), various sand cone volumes were investigated. Slopes from the angle of repose of the particulate mix, 33°, to those approaching realistic Martian values, e.g. 5° for Olympus Mons [*Plescia*, 2004], were also assessed (**Plate 3.3b: 3**). Those cones with angles below that of repose were constructed by sieving rather than pouring, to predetermined heights and diameters, and again smoothed.

Several experiments in this set (specifically, QlX. C 07-12) were conducted with silicone carbide (SiC) particles randomly distributed across the model cone surface. The particles' movement during deformation was used to illustrate the direction and magnitude of surface strain.

2.4.4 set D: sand layer thickness

The thickness of the brittle, upper lithosphere on Mars (that portion of the planet comprising both crustal and mantle components) remains undetermined, though a range of values has been proposed

[*Comer et al.*, 1985; *Zuber et al.*, 2000; *Belleguic et al.*, 2005]. Additionally, lithospheric thicknesses are likely to vary across the planet, and thus beneath each terraced volcano, with commensurate effects upon their flexural profiles. The brittle Martian lithospheric was simulated in this set by sand layers of varying thicknesses, uniformly sieved directly upon the silicone (**Plate 3.3c**).

2.4.5 set E: plaster layer thickness

To further explore the effect of competency contrasts within Martian volcanoes, the covering plaster layer was incrementally deepened in these experiments, whilst all other parameters remained unchanged (**Plate 3.3d**). The thickened plaster simulated an increasingly rigid carapace within the cone (see Chapter 4, section 4.1, page 64).

2.4.6 set F: basal décollement

Finally, the effect of flexure upon a volcano decoupled from its basement was investigated. A detached volcano may display different superficial strains to one which is welded to the supporting substrata [*McGovern and Solomon*, 1993], and so warranted consideration. Such a basal décollement may be structural or rheological in nature, and can facilitate volcano spreading [*van Wyk de Vries and Matela*, 1998] and sector collapse [*van Wyk de Vries and Francis*, 1997]. Thus silicone sheets approx. 20 cm in diameter but of varying thicknesses were placed between the cone and a sand layer, to explore the potential effect upon a volcano of flexural slip along a basal detachment instead of flexural shear within a welded cone (**Plate 3.3e**). Once emplaced upon the silicone sheets, the cone's slopes were smoothed with sand as before, so the load did not rest on a dais of silicone. These experiments expanded upon those in the silicone inclusion set (specifically experiment QIX. B 07).

2.5 quantitative experimental programme (QnX.)

This programme consisted of three experiments, based upon the geometry of the simple loading model (**Table 3.3**), and using the same experimental setup as before (see 2.2). Brittle sand layers were present in two of the three cases cases. Whilst most Martian volcanoes are approximately axisymmetric, one experiment featured a cone with an aspect ratio of 2:1 (long axis:short axis), to examine the effect of edifice asymmetry.

A set of measurements was taken for all experiments to quantify the deformation due to flexure (**Table 3.4**). Most values were determined in the laboratory at the time the experiments were run; the time of first terrace formation was obtained from time data encoded on photographs of the experiments. Together, these data were then used to calculate average geometrical values, strain

amounts, and timing of deformation for each model, which help in understanding the kinematics of the flexural process (see 3.2, **Table 3.10**).

3. results

3.1 qualitative experimental programme results

Flexure occurred in virtually all of these experiments, evinced by four distinct types of structure: flank convexities, a bowl-shaped depression, a circumferential trough, and an annular zone of extension. The development of these four structural forms characterised all flexural loading experiments in this study. The tables provided for each experimental set list the most notable structures observed on each model.

3.1.1 set A: simple loading

The following observations describe the state of a representative simple loading experiment at its conclusion, but apply equally to all experiments in this set (**Table 3.5**).

In each case, the weight of the load caused it to sink into the silicone. The cone appeared to sag and experience a decrease in elevation, whilst its basal diameter remained unchanged or slightly decreased. A series of convex-upward, outward-verging structures quickly formed upon the cone's flanks, and developed continually throughout the experiment. These terrace-like features were concentrically arranged about the cone in an imbricate stacking pattern; their leading edges were often laterally contiguous for several tens of degrees (**Plate 3.4: 1**). Though they largely resembled the terraces observed on Mars and Earth, the model features were less arcuate in their surface trace. Additionally, the characteristic "nose" of real-world terraces was lacking, the leading edges of the laboratory terraces apparent instead of ridge-like bounding scarps. The most prominent convexities were those with the greatest scarps, though the majority were subtle structures best viewed with low-angle illumination. The heights and azimuths of prominence differed between experiments, but the structures were manifest on all flank elevations and sectors.

A broad, bowl-shaped flexural depression developed in the silicone as the load sank, and was visible upon excavation of the sand. The bowl fully enclosed the cone, and was bounded by a slight rise. Its base was near-flat, and some diapirism of the silicone gel produced a knotted texture at its centre. Continued flexure deepened the bowl and reduced its diameter, which served to pin, and in some cases horizontally shorten, the base of the cone.

Immediately inside the flexural bowl, a shallow trough formed proximal to the load, completely encircling it (**Plate 3.4: 2**). Outwardly constrained by the depression, the foot of the cone formed the inner wall. Convex structures sometimes occurred along the trough's outer wall, in some instances verging towards the cone.

Finally, a series of arcuate and en-echelon fractures developed at the outer edge of the trough, forming a circular system of extension centred on the load (**Plate 3.4: 3**). The greatest horizontal displacements occurred at the edge of the flexural bowl, with smaller cracks occurring further onto the surrounding surface; intersecting fractures formed discrete blocks within this zone. As the flexural bowl contracted the fracture zone broadened, its leading edge moving inward towards the cone.

3.1.2 set B: silicone inclusions

Ductile inclusions did not contribute to the formation of flank terraces; instead, despite featuring a range of inclusion geometries, the formation of spreading structures consistently typified this experimental set (**Table 3.6**).

Those experiments performed on counter tops, QIX. B 01-07, were unable to undergo flexure, and demonstrated that the presence of an inclusion led to the development of arcuate and/or radial graben on the upper surfaces of the sand cones. In some instances the cones spread or flattened (QIX. B 01, 07), whilst in another the inclusion penetrated the cone's upper surface (QIX. B 02). None of these experiments developed flank terraces.

As experiments QIX. B 08-14 were conducted on silicone, flexure did occur, indicated by the formation of annular extensional zones (**Plate 3.5**). Each model also developed spreading structures, however, from radially-oriented tension cracks (QIX. B 14) to fully developed, lenticular graben (QIX. B 09), positioned between the centre of the load and the outer fracture zone (**Plate 3.5: 1**). Terraces formed close to the summit on some cones (QIX. B 10, 13) (**Plate 3.5: 2**), but in no case did terraces form without extensional flank structures.

3.1.3 set C: cone geometry

Changes in cone width, ω, as a proxy for volume (QIX. C 03-06) did not produce appreciable effects: the same suite of structures was manifest in experiments with either 12- or 25 cm-diameter loads (**Table 3.7**) (**Plate 3.6**). Terraces, flexural depressions, troughs, and fracture zones were proportionately smaller in lower-volume models, but otherwise they developed as before. The number of terraces was reduced in these experiments.

A greater difference was apparent in experiments where cone slopes were varied. Flank structures were easily visible on slopes between 35° and 15° (QIX. C 07-10) but below this threshold, even with low-angle illumination, they were difficult to detect. However, the silicone carbide particles on the surfaces of experiments QIX. 07-12 — which represent the range of slopes from repose to those on Mars — all exhibited the same behaviour: points within the extensional zone moved towards the centre of the load, shortening the radial and concentric distances between each other, whilst the SiC particles beyond the annular fractures behaved in the opposite manner,

moving away from the load and one another. These experiments differed only in that the points' horizontal displacements decreased as values of α were reduced.

Other characteristic structures remained largely unaffected by changes in slope; troughs, fracture zones, and flexural bowls developed as before, though lower-angle cones produced shallower depressions in the silicone.

3.1.4 set D: sand layer thickness

Thin brittle layers did little to affect the development and morphology of flexural structures with respect to simple loading, even where cone volumes and slopes were changed (experiments QlX. D 02 and 03). Nonetheless, sand layer thicknesses exceeding 5 mm had a patent effect, particularly upon flank convexities and extensional zones (**Table 3.8**).

Terraces grew more pronounced with increasingly deep sand layers, until they became very clearly defined structures with vertical displacements of several mm along their leading edges (**Plate 3.7: 1**). Progressively thicker layers also increased the spacing between terraces, so fewer, larger convexities formed. This trend was reversed with the thickest sand layer (δ = 30 mm, QlX. D 09), however, as the terraces herein were less well expressed and more numerous than in the preceding experiment.

Experiments with ever deeper sand layers formed proportionately shallower flexural depressions. Thicker layers extended the width of the annular fracture zone, until in later experiments it grew to form a partial or complete half-graben system, bounded by steep scarps (**Plate 3.7: 2**). This rift occurred atop a broad topographic bulge, which tended towards the edge of the container. The circumferential trough narrowed as the bulge widened, forming a series of radially-orientated wrinkle ridge structures across the trough's base and outer wall (**Plate 3.7: 3**). Interestingly, increasingly thick sand layers also increased the radial distance of the topographic bulge to the load.

3.1.5 set E: plaster layer thickness

Whilst the ability of a thin (sub-mm) plaster coating to preserve subtle deformation had already been documented, even values of ε less than 5 mm tempered the expression of model terraces. Layers in excess of 10 mm thick suppressed and ultimately stopped terrace development entirely (**Table 3.9**; **Plate 3.8: 1**). Later experiments in this set too developed a broader fracture zone, typified by extensive polygonal and blocky terrain (**Plate 3.8: 2**). This served once again to narrow the flexural trough, leading to the formation of radial wrinkle ridges along the outer wall (**Plate 3.8: 3**).

3.1.6 set F: basal décollement

A basal detachment did not affect the development of flexural structures in these experiments, but did result in the formation of another feature: a convex ridge encircling the load (**Table 3.10**) (**Plate 3.9a: 1**). The ridge developed coevally with flexure, forming at the base of the cone, moving inward and increasing in height as sagging progressed, ultimately being located on the inward-facing wall of the trough. Immediately inside the ridge, the lower flanks of the cone adopted a concave-upward aspect, forming a shallow annular depression (**Plate 3.9a: 2**).

Fracturing generally delineated the apex of the ridge, which, with increasing sand layer thickness, formed a pronounced outward-facing scarp about the cone. In some cases, a smaller, backward-facing scarp also developed (e.g. QIX. F 09). Excavation of the overlying sand showed that the silicone sheet thinned and became bowl-shaped like that of the flexural depression, and that the scarp consisted of uplifted sand to a depth of at least a centimetre.

This basal scarp was present with sand depths of up to 30 mm. At $\delta = 60$ mm, however, flexure did not occur: instead, the load experienced spreading, forming a steeply-sided dome with radial leaf graben on its upper surface (QIX. F 06). The structure was most visible when the ratio of sand layer thickness to silicone sheet depth was greater than 1 (e.g. QIX. F 04); with $\delta:\beta \leq 1$ the scarp was less prominent. Nonetheless, even with values of $\delta:\beta$ greater than one, decreased load volumes (through reduction of the cone slope angle, α, or cone width, ω) had a definite effect, rendering the scarp much less visible until it disappeared entirely (QIX. F 10 and 11, respectively).

3.2 quantitative experimental programme results

The three experiments conducted in this set returned useful quantitative data on the geometric effects of flexure. The key results are summarised in **Table 3.11**; the entire dataset for each QnX. experiment is provided in **Appendix II.II**.

In each case, the cone experienced a decrease in basal diameter along both N-S and E-W transects, but lengthened vertically. The horizontal constrictional strain was approx. an order of magnitude less than that of the vertical deformation, and was especially pronounced in the 2:1 aspect ratio model, QnX. 03.

The flexural bulge was manifest as a positive topographic structure above the reference surface for each experiment; the flexural trough remained a negative topographic feature relative to the bulge, even when it too rose above the reference surface (QnX. 02). Width values for the annular extensional zones in experiments with sand layers were similar; where the sand layer was not present, however, this zone was considerably broader (QnX. 01). In every experiment, terraces were visible upon the models' flanks within two to three minutes after flexure began.

4. discussion

4.1 the effects of simple loading

The qualitative experimental set provides geometric and kinematic information on the properties of viscoelastic flexure in response to a conical load, and show that all four types of primary flexural structure developed contemporaneously. Their formation is summarised below.

The cone represented a gravitational high which sought to equilibrate with the surrounding plains, and so sank as a cohesive unit, bending the underlying silicone and forming the bowl-shaped flexural depression. The cone's upper surface experienced a radial and concentric shortening, with its area being preserved by the development of the terraces.

The formation of the flexural bowl displaced silicone radially away from the load; some of this material was uplifted to form an encircling flexural bulge. The annular extensional zone surrounding the cone was the superficial expression of this rise: the bulge's fold axis experienced an increase in surface area, which was accommodated by arcuate and polygonal fracture sets. The upward motion of the flexural bulge relative to the cone's lower flanks, together with the downward motion of the central material, produced the circumferential trough at the base of the load.

The quantitative loading experiments help quantify flexural deformation, and demonstrate that in each case where flexure occurred, the cone experienced a reduction in basal diameter along both horizontal axes. Cone volume was preserved, however, by a lengthening along the vertical axis, indicative of a horizontal constrictional strain. The anticlinal flexural bulge represented a low rise encircling the volcano, bounding the synclinal shallow circumferential trough. The rapid formation of terraces early in the experiments implies that only small strain amounts are necessary for these structures to form.

4.2. the effects of parameter variations

4.2.1 silicone inclusions

In virtually all instances, silicone inclusions changed their shapes by flowing, which increased their upper surface areas and formed extensional structures on the overlying sand. This flattening occurred regardless of inclusion shape or elevation within the cone, nor was it affected by cone geometry. However, terraces formation in this set of experiments occurred only with flexure, independently of any inclusion parameters. Thus, whilst ductile bodies, as a proxy for low-strength layers and other competency contrasts within a volcano, did not inhibit the development of terraces, they are not a prerequisite for terrace formation, either.

4.2.2 cone geometries

Both 12- and 25 cm diameter cones displayed terraces, though terraces on smaller loads were proportionately smaller. This implies that load size has little effect upon terrace formation, and is suggestive of a scale-invariant nature for these structures. Moreover, changes to slope angle did not appear to alter the flexural process, as surface contraction was observed across all cones during flexure, even when terraces were not visible. The difficulty in seeing terraces on lower-angle cones may be an experimental limitation, with the sand accommodating the contractional surface strain via grain flow. Nevertheless, the results indicate that terraces can form across a range of cone geometries.

4.2.3 sand layer thicknesses

For time-independent cases, a material's flexural profile is a function of its rigidity: an increase in that material's ability to resist the effect due to gravity of an emplaced load results in an increase in wavelength and a decrease in amplitude. The increase in basal layer thickness provided greater flexural support to a load, resulting in reduced bending, and forming progressively broader flexural profiles. This was manifest by shallower flexural depressions, wider annular extensional zones, and flexural bulges developing progressively further from the load. This in turn resulted in cones atop thicker sand layers experiencing smaller degrees of upper surface shortening than those upon thin layers, requiring the formation of fewer structures to resolve this strain. Accordingly, the thickness of a brittle layer below a conical load can influence the development and geometry of terraces upon that load.

4.2.4 plaster layer thicknesses

The gypsum plaster used in these experiments has a greater cohesion that quartzose sand, and so preserves small-scale structures like terraces well (e.g. QIX. Set A); nonetheless, a threshold was reached in this experimental set beyond which no terraces formed (approx. above ε values of 10 mm). This may be due to the material properties of the gypsum, whose yield strength is sufficient to accommodate flexure-induced surface stresses entirely through volumetric strain and without brittle deformation, thereby precluding the need for terraces to develop.

4.2.5 basal décollement

The flexure of a basally detached cone produced the same characteristic structures as a welded load, but with the addition of a circumferential scarp at its base. The convex-outward nature of this structure suggests material was pushed up and away from the cone as it sank. Additionally, the leading edge of the scarp corresponds to the areal extent of the underlying silicone sheet. That the sheet assumed a bowl shape indicates that its edges moving upward relative to the sagging load,

suggesting that the scarp was produced by outward thrusting of the ductile layer as it deformed during flexure.

If the silicone sheet was mechanically attached to the supporting sand, such deformation would have been contained within the typical flexural profile, and no new surface structures would be apparent. If decoupled from the sand, however, the silicone could behave as a discrete body, thrusting up and along the underlying sand, and the cone would be equally decoupled from the silicone sheet. In a detached model, therefore, flexure would be accommodated along two slip surfaces: the interface between the underlying sand and the ductile layer, and between that layer and the load. This would effectively form two flexural profiles, which accounts for the model morphology in this experimental set: the outer flexural bulge and trough formed as before, whilst the scarp and concave lower slopes of the cone represent a second, inner flexural crest and associated trough, respectively.

It is important to note that while flexure occurred in these models, some element of volcano spreading also took place, where spreading is defined by the differential movement of the edifice and basal material. Spreading can therefore occur without a significant movement of the volcano's margin. Such a juxtaposition of these processes (spreading and flexing) has been reported for Kilauea [cf. *McGovern and Solomon*, 1997a].

In experiment QIX. F 06, where doming of the cone occurred, the thickness of the underlying sand layer was probably sufficient to resist the downward force of the load without bending. The presence of the silicone sheet, however, allowed the cone to partially equilibrate through spreading, though only to the extent to which the silicone itself could horizontally deform (see 4.4.4).

4.3 kinematic synthesis

Considering the results of both qualitative and quantitative experimental programmes, it is possible to derive a representative kinematic model for the flexural process and resultant structures observed in these models.

A sand cone and thin sand substrate placed upon a silicone reservoir represent a brittle layer above a ductile one, which causes flexure when the cone attempts to gravitationally equilibrate (**Plate 3.10: 1**). The silicone is depressed by the load and flows away, forming a flexural bowl (**Plate 3.10: 2**). Uplifted silicone forms an anticlinal bulge around the cone (**Plate 3.10: 3**), and a circumferential trough at its base (**Plate 3.10: 4**). Extension along the bulge's fold axis creates an annulus of Mode-I fractures (**Plate 3.10: 5**). The growth of the flexural bulge and depression prevents the cone from spreading. The cone as a whole is shortened horizontally, but lengthens vertically in an attempt to preserve volume. Silicone diapirism may occur at the base of the cone.

Situated within the inner contractional zone, the cone's upper surface undergoes radial shortening (**Plate 3.10: 6**). Since the surface shortens from all radial directions towards a central

point, some concentric shortening must also occur, accompanied by vertical lengthening (ignoring the sand's capacity to accommodate volumetric strain). A strain ellipse with shortening along both the S1 and S2 axes, and lengthening along the S3 axis, characterises the cone's upper surface.

The brittle layer probably deforms not by simple orthogonal buckling, but by flexural shear. In the former case, the greatest strain is borne at the points of maximum curvature of the flexural profile, which correspond to the base of the brittle layer, and the cone summit. Conversely, flexural shear concentrates most deformation on the limbs. The surface strain on the cone is apparent mainly on its flanks, and decreases towards the summit. This strain is resolved by the formation of a set of conjugate shear fractures. With an outward vergence, these fractures form oblique-slip thrusts that dip towards the centre of the cone and terminate at a neutral surface inside the edifice (**Plate 3.10: 7**). Terraces on the cone's flanks develop as hanging-wall anticlines above these thrusts (**Plate 3.10: 8**), and form a fish-scale pattern due to the combination of radial and concentric shortening.

Upper-surface contraction occurs on all cone slopes and sizes, but only forms terraces when the yield strength of the sand is exceeded. Lower-angle cones do not depress the silicone sufficiently to exceed this value. Thickening of the brittle sand layer below the cone alters the flexural profile by increasing its wavelength and decreasing its amplitude: the flexural depression shallows, whilst the flexural bulge broadens and flattens. The cone is subject to a reduced amount of lateral shortening, and so requires the formation of fewer structures to resolve its surface strain. Thickened plaster layers are able to accommodate the shortening strain volumetrically without undergoing obvious brittle deformation much more so than sand alone, and so do not necessarily produce terraces.

A load decoupled from the sand substrate deforms by flexural slip along the basal detachment, though flexural shear is probably still the primary method of upper surface deformation due to the lack of strong mechanical layering within the cone. Like flexural shear, flexural slip localises the greatest strain at the points of inflection on the flexural profile, and shares the same sense of shear. Where the detachment surface is the interface with a low-competency material, flexure of the cone will force this material upward to form an outward-verging basal thrust. The surface expression of this thrust is also a hanging-wall anticline.

4.4 comparison with natural examples

To ensure the applicability of any experimental study, it is necessary to identify and compare its results with natural examples, to provide as thorough an element of "ground-truthing" as possible (e.g. Troll et al., 2002). Here, I review the geometries of the experimental structures with those of real-world examples on Mars.

4.4.1 flank terraces

The flank structures formed in these flexural experiments closely resemble the terraces on Mars. I documented terraces on Earth as well, and discussed them in Chapter 2. Terraces share a convex-upward, outward-verging morphology, and an imbricate "fish-scale" stacking pattern in plan view (**Plate 3.11**). The laboratory structures occur on a range of cone slopes and volumes, and at all flank elevations, regardless of the experimental parameters varied. It has to be noted that they lack the snub-nosed roundness characteristic of most observed terraces, featuring a flattened upper surface instead. Nonetheless, photogeological evidence indicates that terraces on Mars at least have been covered, and their forms tempered, by contemporaneous or subsequent lavas [*Thomas et al.*, 1990]. The features may therefore represent the terrace form prior to being mantled by eruptives (this issue is revisited in Chapter 4, section 4.3, page 67). If so, volcano flank terraces on Mars are hanging-wall anticlines over blind, inward-dipping thrust faults, formed in response to a contractional strain induced by simultaneous radial and concentric shortening of the volcano as it flexed downward, and which were covered by later lavas.

The systematic formation of laboratory terraces on cones of varying slopes and volumes is consistent with observations of Martian volcanoes. Both large and small volcanoes are terraced, e.g. Olympus Mons and Albor Tholus, respectively, as are volcanoes with different slopes, e.g. Alba Patera and Elysium Mons (~1° and ~7°, respectively) [*Plescia*, 2004].

Models with thicker brittle layers below the loads led to fewer, larger terraces. This is consistent with studies that have attempted to determine Martian elastic lithospheric thicknesses (T_e) using extensional surface features and elastic flexure theory [*Thurber and Toksöz*, 1978; *Comer et al.*, 1985] and a synthesis of topography and gravity data [*Zuber et al.*, 2000; *McGovern et al.*, 2002, 2004; *Belleguic et al.*, 2005]. Whilst estimates for crustal thicknesses differ between studies, in all cases relative T_e values are the same. Specifically, Ascraeus and Olympus Montes are consistently quoted as being supported by the thickest elastic crust of all Martian volcanoes. Of the nine study volcanoes on Mars, these volcanoes display the most visible and largest terraces (see Chapter 2, Table 2.2).

That thick plaster coverings inhibited terrace formation in the models, though thinner layers had no such effect, suggests that there is no significant competency contrast between the cover units of terraced volcanoes and their deeper strata. The rheological stratigraphy of Martian volcanoes is discussed further in Chapter 4 (section 4.1, page 64).

4.4.2 flexural trough

One of the distinguishing features of lithospheric loading is the formation of a flexural trough or moat about the load. Given their large masses, Martian volcanoes can be expected to display measurable vertical deflections of the lithosphere [*Comer et al.*, 1985]. Such troughs are not readily

visible on photogeological images, however, and are identified more easily on DTM data [*Zuber et al.*, 1993]. Indeed, MOLA topographic profiles indicate the presence of flexural troughs associated with several large crustal loads on Mars, including Olympus Mons [*Zuber and Smith*, 1997], the Tharsis Rise itself [*Solomon and Head*, 1982], and the entire southern hemisphere [*Watters*, 2003].

The difficulty in seeing these features may be due, in part, to infill by later material such as landslide deposits [*McGovern and Solomon*, 1997a] and lavas from smaller, nearby shields or fissures [*Bleacher et al.*, 2007]. Infill may also account for the lack of visible troughs on Venus [*McGovern and Solomon*, 1997b]. Assuming these moats form part of the flexural response of the Martian lithosphere to loading, they correlate to the circumferential trough formed in these flexural experiments, and thus likely share a similar tectonic provenance.

4.4.3 concentric graben

The annular zone of extension characteristic of these flexural experiments is a common feature of lithospheric loading, where bending stresses exceed the yield strength of the elastic crust. Load-concentric fractures have been observed on Earth [*Lambeck and Nakiboglu*, 1980], associated with mascons on the Moon [*Melosh*, 1978], and related to large crustal loads on Mars, including volcanoes [*Comer et al.*, 1985].

It is likely, therefore, that the ring fractures about Elysium Mons (**Plate 3.12a**), the arcuate graben that cross-cut the W flank of Ascraeus Mons (**Plate 3.12b**, and Chapter 4, section 4.2, page 66), and the group of prominent troughs on the NE foot on Pavonis Mons (**Plate 3.12c**) all correspond to the peripheral fracture system that forms in these experiments in response to flexure. In this case, these graben lie along the fold axis of a flexural bulge encircling each of these volcanoes.

4.4.4 basal scarp

The morphology of experiments with basal detachments bears a strong similarity to Olympus Mons: a convex-upward structure that (partially) encircles the load, bounding concave-upward lower flanks that transition to convex, terraced upper sides (**Plate 3.13**). Some minor differences exist between those models featuring a basal scarp and Olympus Mons, however: the feature surrounding Olympus features a ski ramp-like raised rim which is largely lacking from the models, and the terraced zones vary in position between the models and the Martian volcano.

Nonetheless, if the Olympus Mons scarp is in effect a basal thrust formed by flexural slip, then a strong planar mechanical anisotropy must exist beneath the volcano. Low-competency materials such as ice-rich regolith [*Tanaka*, 1985], volcanoclastic and/or aeolian sediments, hydrothermally altered deposits, or phyllosilicate clays [*McGovern and Morgan*, 2009] may provide a surface along which flexural slip could occur. These materials may lie across the Tharsis-Syria uplands.

Conversely, they may be innate to the volcano, in which case the scarp represents the outer extent of the shield.

The basal escarpment around Olympus has well-defined concave-outward boundaries in places that resemble the headwalls of landslide deposits. If flexure of the edifice has uplifted underlying incompetent strata, oversteepening could cause detachment of this material along listric normal faults, forming landslide deposits in an aureole about the volcano. These deposits probably helped fill the attendant flexural trough and obscure associated surface fractures.

This model has implications for the development of Olympus Mons. Previous authors have regarded the basal scarp and aureole deposits as evidence of gravitational spreading of the entire edifice [*Francis and Wadge*, 1983; *McGovern and Solomon*, 1993; *McGovern et al.*, 2004], though most did not account for the lack of spreading structures on the volcano's flanks [*Borgia*, 1994]. Lithospheric flexure along a discrete slip plane, however, together with some element of volcano spreading, can account for the overall morphology of Olympus Mons: flexure-induced constriction is accommodated on its mid- to upper flanks by distributed terracing, and at its base by slip along a basal décollement. Flexural slip might also have influenced the structure of other volcanoes, accounting for basal scarps surrounding Arsia and Ascraeus Montes, and Mauna Loa on Earth.

It is also worth noting that in experiment QlX. F 06, a very thick underlying sand layer appeared to prevent the flexure of a detached load, instead forcing it to partially spread and flatten, and develop radial cracks on its upper surface. The resulting structure resembles the pancake domes on Venus recorded by the Magellan mission [*Head et al.*, 1991] (**Plate 3.14**). These domes may be formed of viscous magmas extruded from a central conduit [*McKenzie et al.*, 1992], but *Fink et al.* [1993] suggested that their compositions cannot be constrained from their morphology alone. Accordingly, the conditions by which the experimental dome formed may provide some insight into how these Venusian structures formed, and of the material properties of that planet's crust.

In any case, flexure-induced contraction may be accommodated along a continuum between diffuse flexural shear resulting in the formation of many small thrusts, e.g. Elysium Mons (see Chapter 2, Plate 2.11), and discrete flexural slip, with radial shortening localised on a large basal thrust, like that of Olympus Mons.

5. concluding remarks

Scaled analogue models provide a first-order geometric and kinematic understanding of the flexural process. Through varying a set of parameters within a basic experimental setup, differences in cone geometry, internal layering, and crustal heterogeneity have been examined. Collating these results provides a basis for understanding flexure-induced deformation in these experiments.

A set of four structures characterises analogue lithospheric flexure. A flexural depression forms due to loading of a sand cone, which in turn uplifts material in an annulus around the load;

fracturing occurs along this bulge's fold axis. A concentric trough forms at the base of the cone due to the relative upward motion of the bulge. The cone itself is subject to bending, and its upper surface accommodates a synchronous radial and concentric constriction by the formation of hanging-wall anticlines above outward-verging shear fractures. These thrusts have a convex-upward and -outward morphology, and are distributed on the cone's flanks in an imbricate pattern.

The structures formed in these experiments bear a strong geometric similarity to natural examples on Mars. The real-world features may therefore have a similar provenance to their experimental counterparts. If so, flank terraces on Martian volcanoes represent thrusts formed due to flexure-induced contraction, and topographic moats and concentric fractures around several large shields correspond to flexural depressions and bulges, respectively. I conclude, therefore, that lithospheric flexure is the mechanism responsible for flank terrace formation on Mars, based on a synthesis of flank terrace observations, and analogue modelling. This hypothesis, however, needs to be tested in a real-world context, which is the focus of Chapter 4.

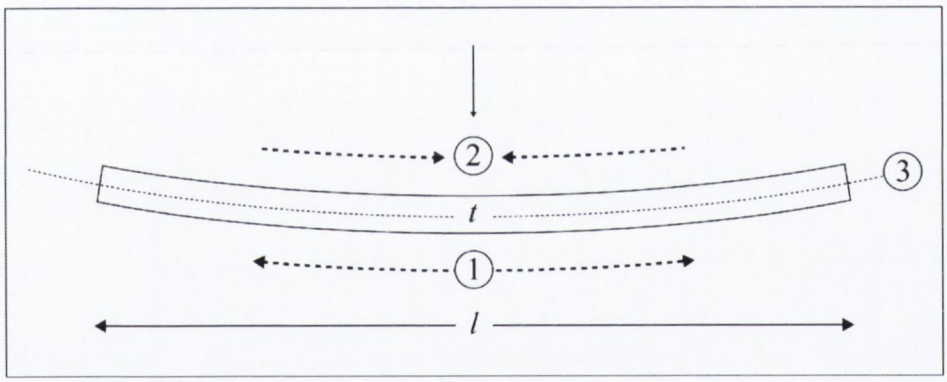

Plate 3.1. A cartoon illustrating the principal strains experienced by an elastic plate, of length *l* and thickness *t*, undergoing flexure. Lengthening occurs along the outer arc of the flexural profile (1), whilst commensurate shortening occurs inside the arc (2). No strain is experienced by the plate along the neutral plane. Note however that this cartoon refers specifically to a plate, and that lithospheric flexure can involve much greater thicknesses of rock, and is accompanied by a topographic arch that develops simultaneously to surround the load.

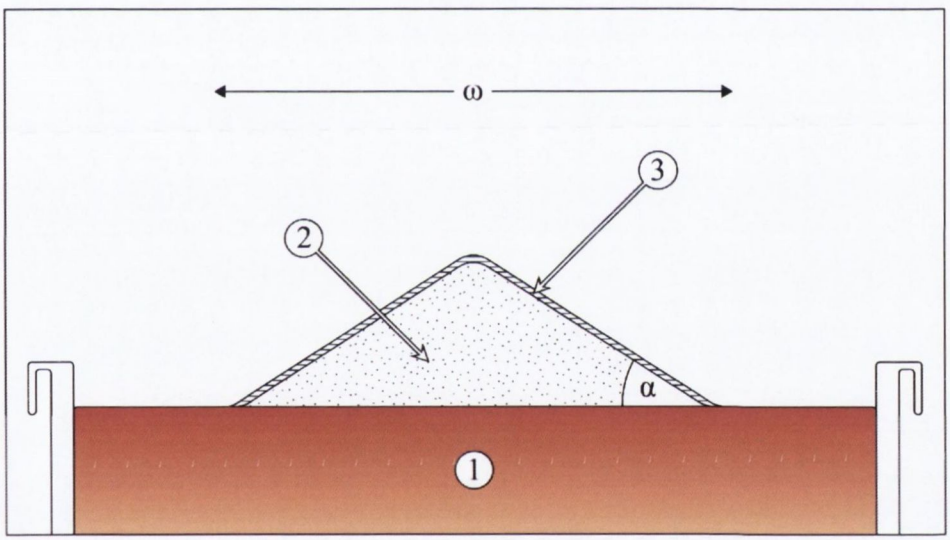

Plate 3.2. Schematic diagramme of the experimental setup for simple loading. A silicone reservoir (1) is loaded with a conical load of sand (2), which in turn is covered with a thin plaster layer to preserve any small-scale structures that might form (3). The cone's geometry is a function of its width, ω, and its slope angle, α. Note that the reservoir is deeper than it is wide, but the entire depth is not shown. Additionally, this experimental setup does not truly reflect lithospheric flexure, in that no elastic basal layer is present, but instead illustrates an approximation of Airy isostasy. Later experiments featuring a basal layer do represent true flexure, however (cf. Plate 3.3).

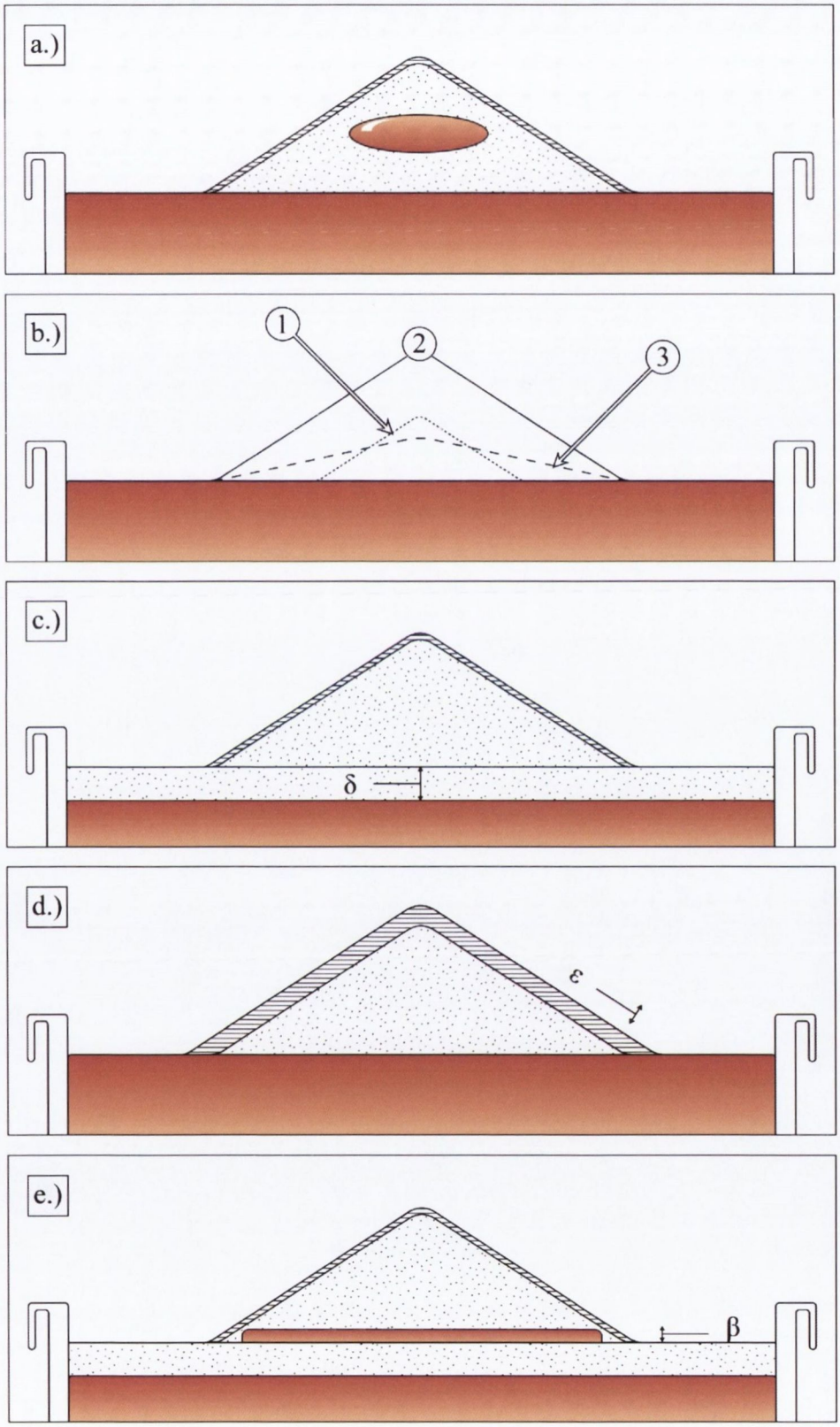

Plate 3.3. Variations in setup for the QIX. experimental programme. The effects of **a.)** silicone inclusions within the cone; here, an ellipsoid represents a high-level magma chamber (experiment QIX. B 06); **b.)** cone geometries: (1) 12.5 cm-diameter cone, (2) 25 cm-diameter cone, (3) 20° cone; **c.)** sand layer thickness, δ; **d.)** plaster layer thickness, ε; and **e.)** a silicone sheet of thickness β, serving to decouple the load.

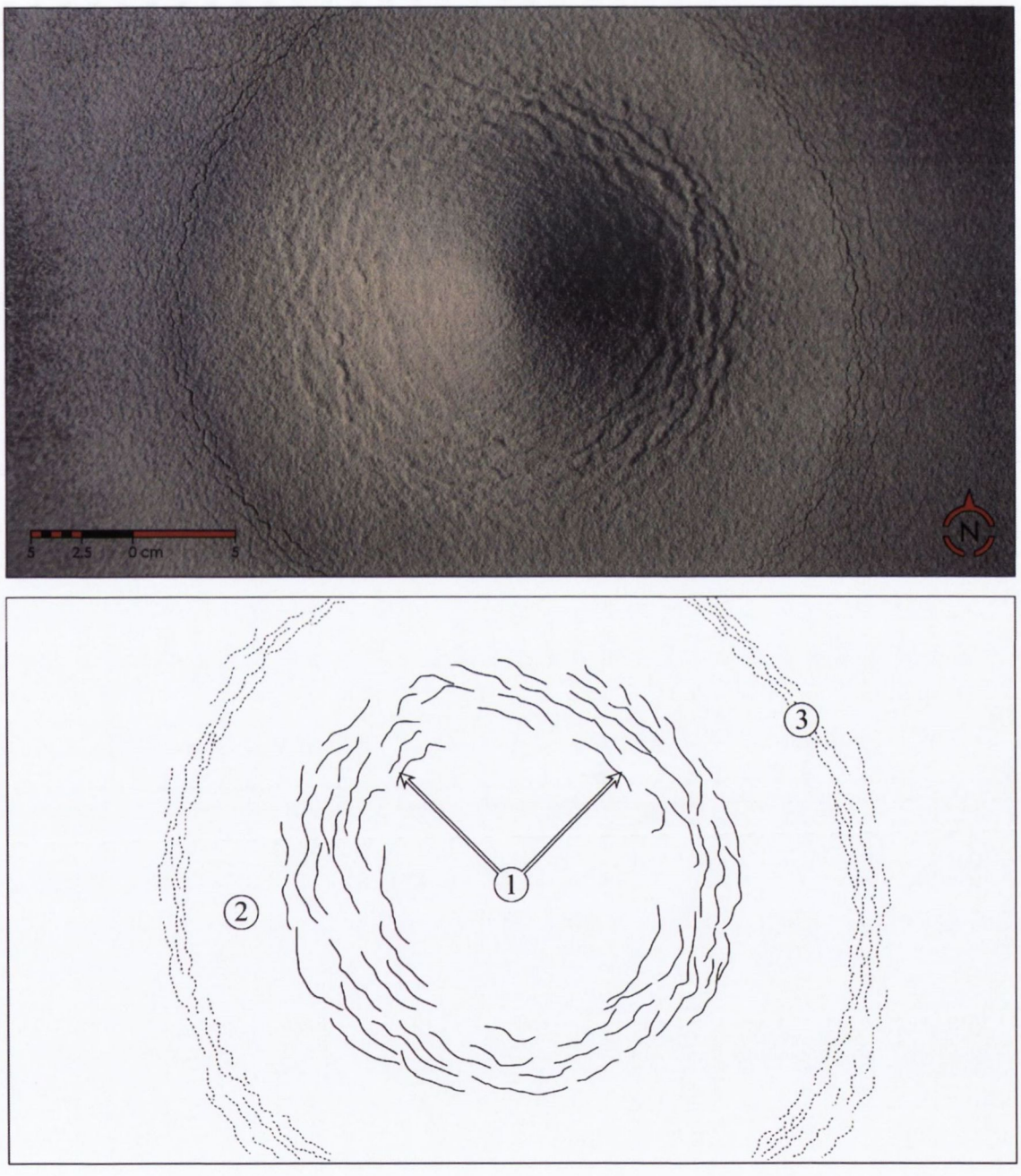

Plate 3.4. QIX set A: simple loading results. The cone produced a set of convex-outward, convex-upward structures (1), and shallow circumferential trough (2), and a zone of extension ringing the load. Experiment QIX. A 01.

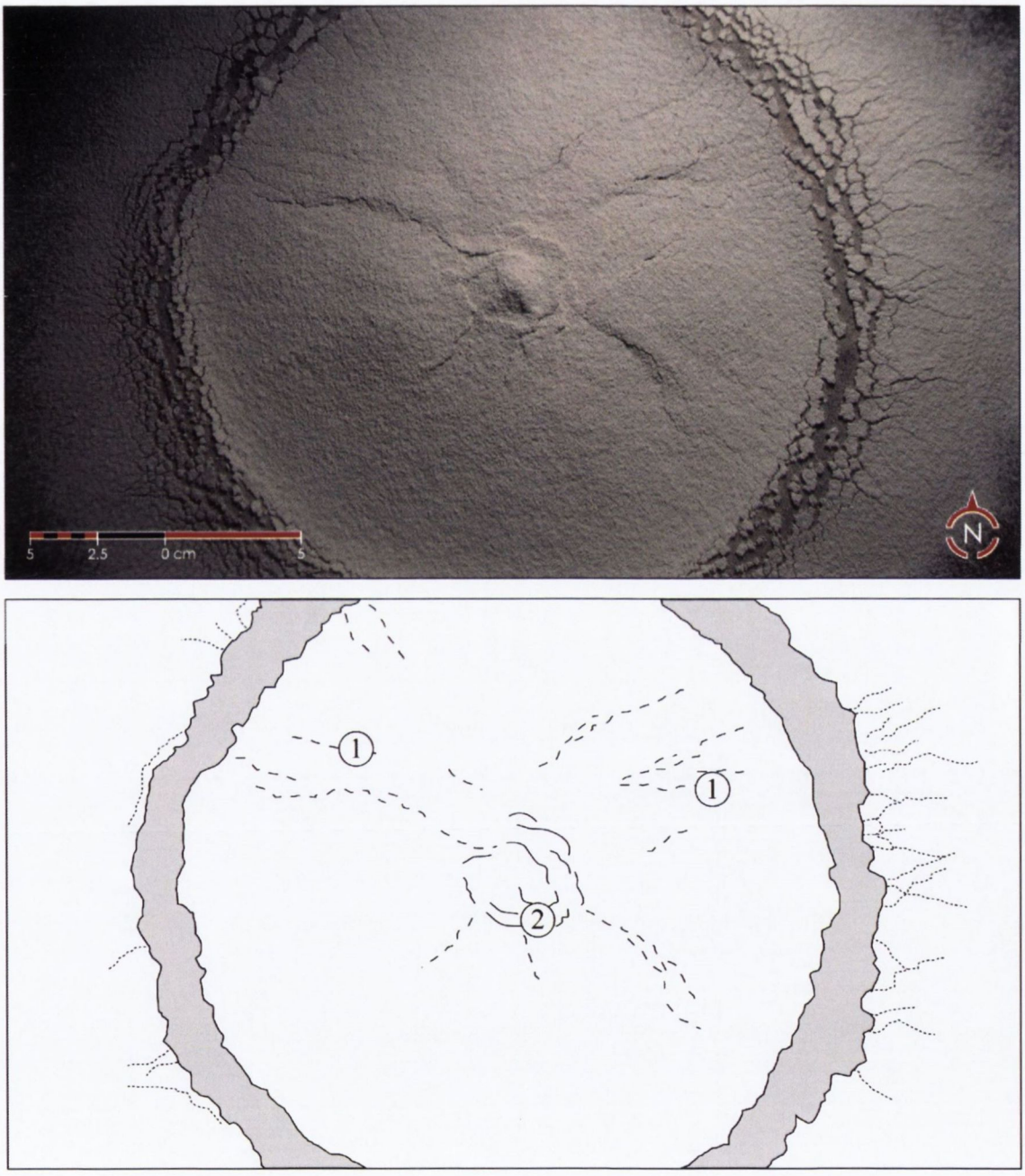

Plate 3.5. QlX set B: silicone inclusions. Though flexure occurred in this experiment, indicated by the annular zone of extension (grey fill), associated radial fractures, and group of terraces encircling the summit (2), a set of radially-oriented extensional structures formed on the cone's flanks. Experiment QlX. B 09.

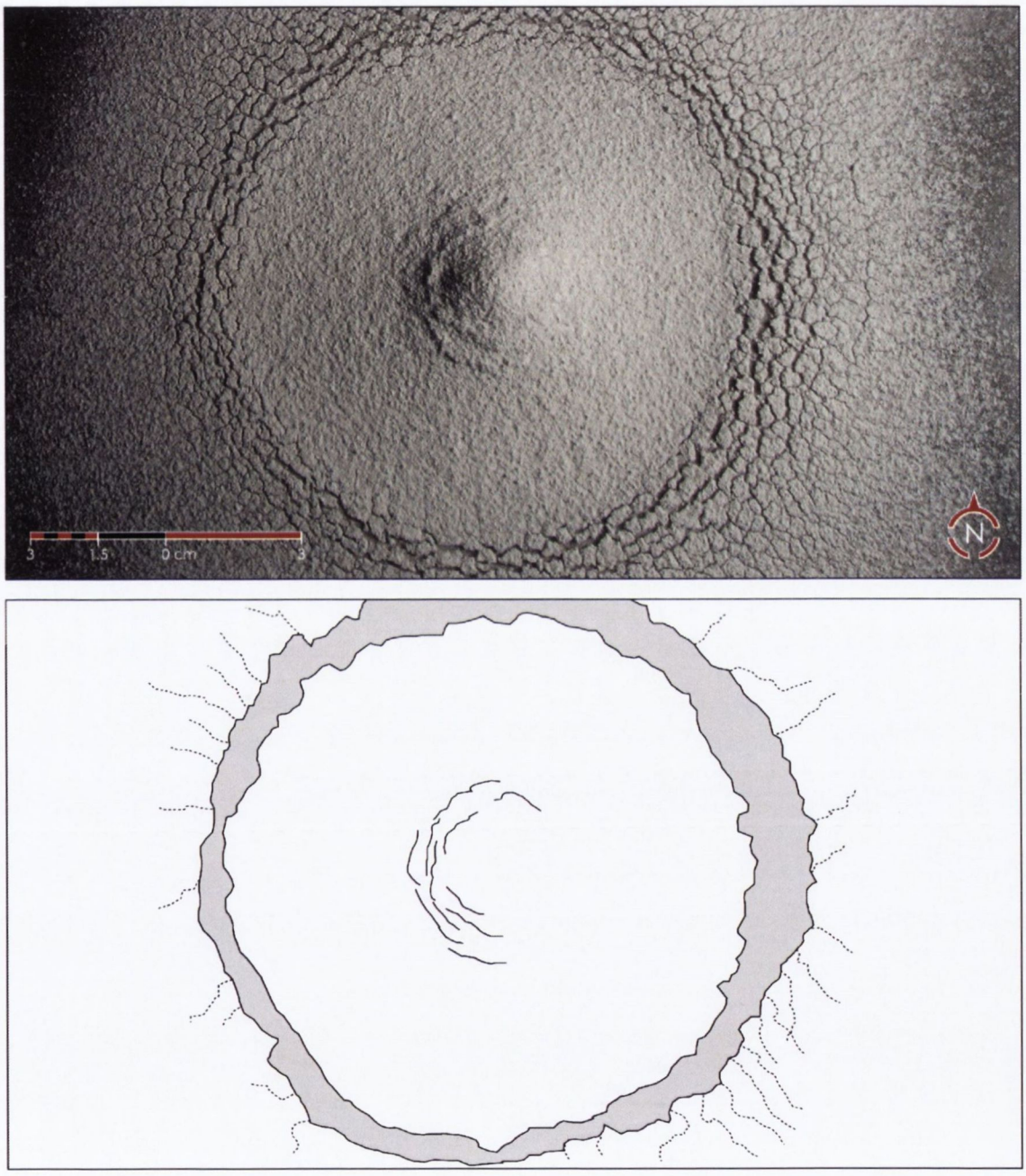

Plate 3.6. QlX set C: cone geometry. This 12 cm-diameter cone developed the same principal structures as larger cones. Terraces formed to circle the summit, whilst extension occurred around the load. Experiment QlX. C 03.

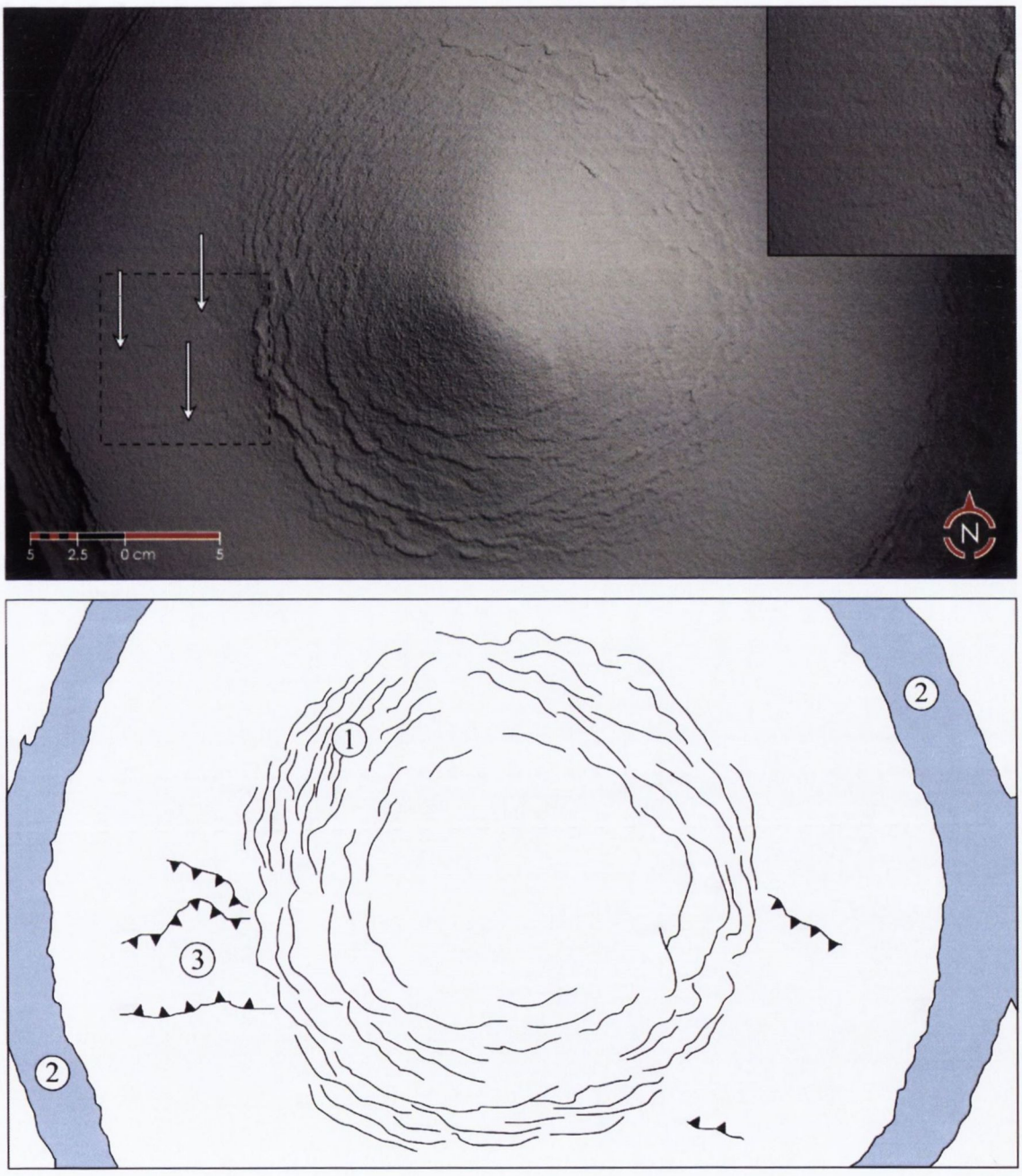

Plate 3.7. QlX set D: sand layer thickness. Key structures to form in this experimental set include (1) flank convexities, (2) a broad, circumferential zone of extension around the cone, and (3) a series of radially-oriented wrinkle-ridges within the flexural trough (highlighted by white arrows in the upper image, and shown in the inset to the top right). Experiment QlX. D 06. Note how the extensional zone in this experiment occurs at greater radial distance to those in earlier experiments with thinner elastic layer thicknesses (e.g. QlX. sets A, B), as a function of additional flexural support bring provided by thicker sand layers.

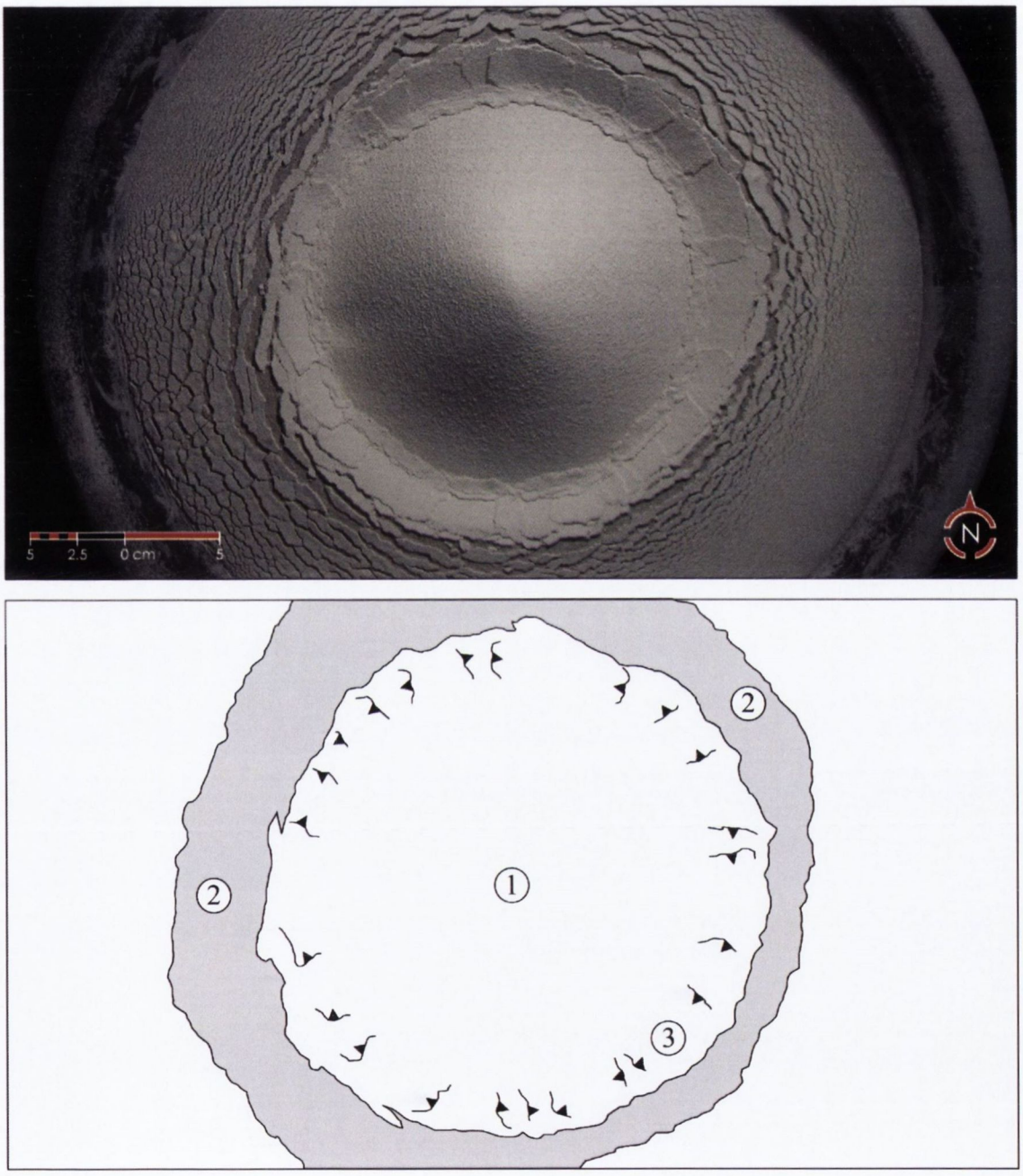

Plate 3.8. QIX set E: plaster layer thickness. The flanks of the cone in this experiment did not experience any visible deformation (1), though the characteristic annular extensional zone developed (2). Radial wrinkle-ridges again formed within the flexural trough (3); note too the circular, outward-verging ridge at the base of the cone. Experiment QIX. E 06.

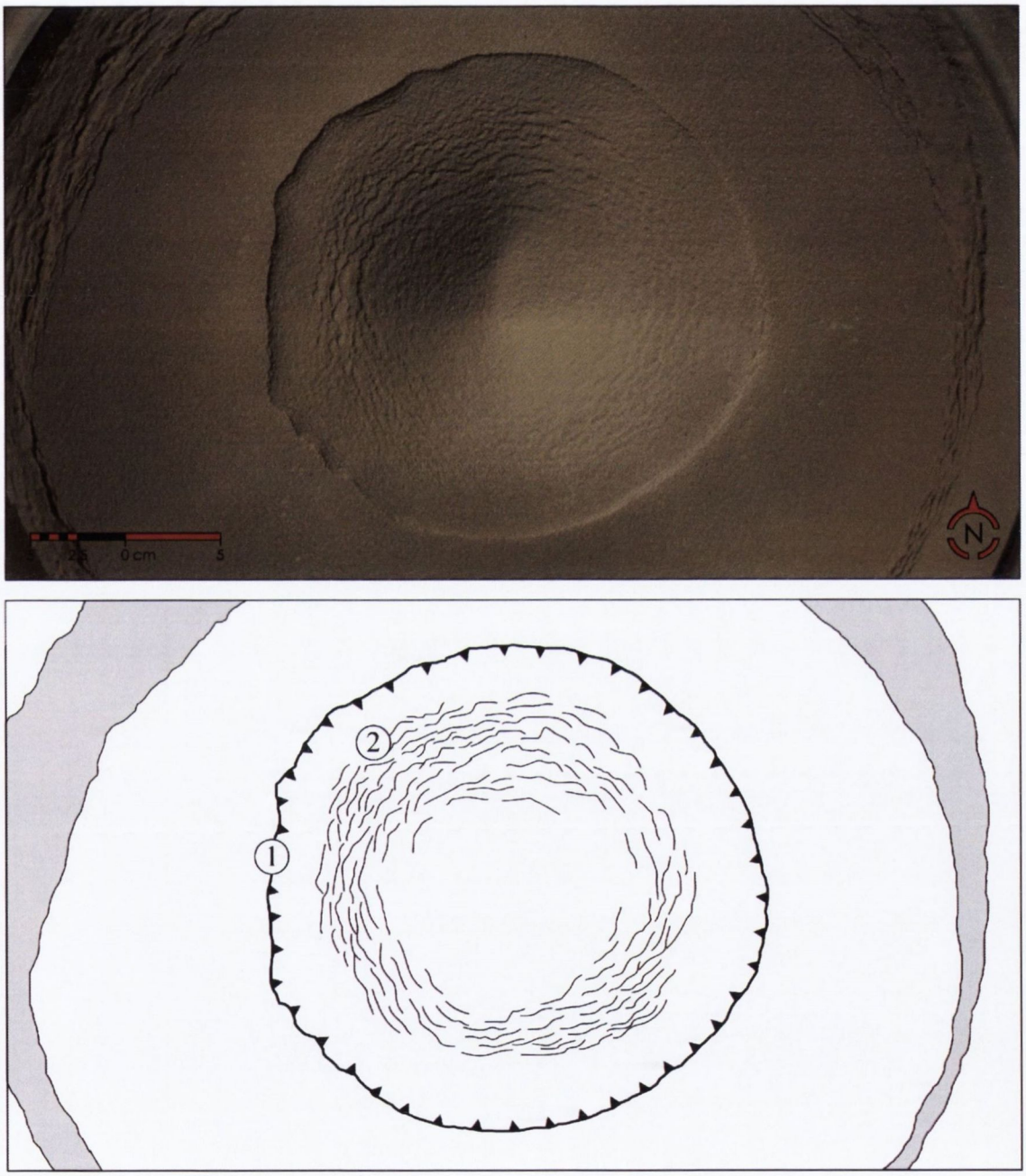

Plate 3.9. QIX set F: basal décollement. The presence of a detachment led to the formation of a scarp encircling the load (1): this outward-verging structure displayed some superficial fracturing, and formed a shallow moat at the base of the cone (2). An extensional zone also developed. Experiment QIX. F 04. Both flexing and spreading processes occurred in these models, the former due to sinking of the load into the underlying reservoir, and the latter accommodated by relative outward motion of the edge of the edifice with respect to the basal material (in this case the supporting sand layer).

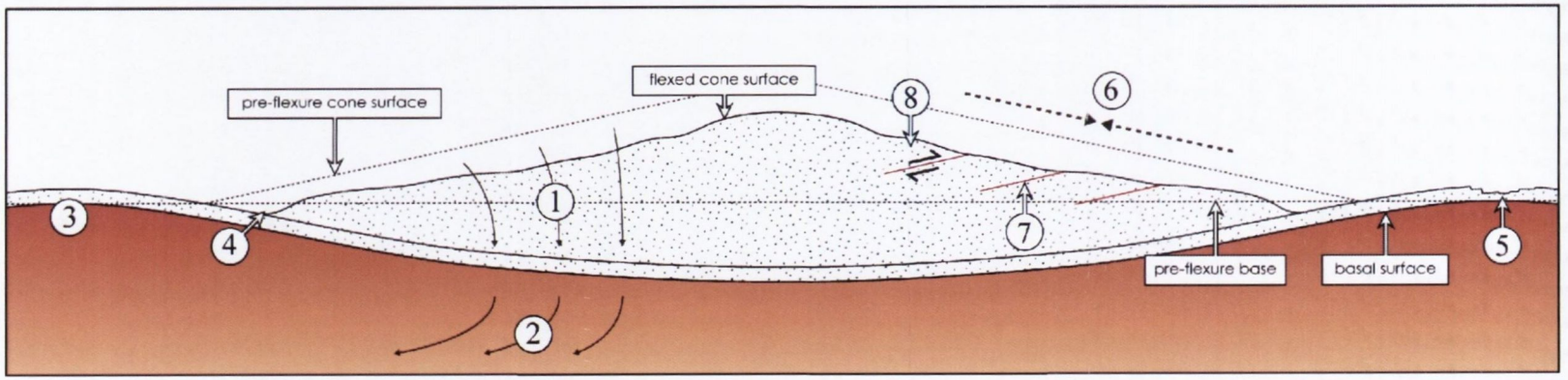

Plate 3.10. A cartoon illustrating the kinematic synthesis presented in section 4.3. The cone flexes inward (1), forcing silicone down and away (2). Displaced silicone causes a ring of uplift around the cone (3), and a circumferential trough to form (4). Extension along the flexural bulge leads to an annular system of fractures (5). The upper surface of the cone experiences radial and concentric shortening (6). This surface strain is resolved by the formation of inward-dipping, oblique-slip thrusts which verge outward (7). Movement along this planes forces material up into hanging-wall anticlines (8), which correspond to flank terraces.

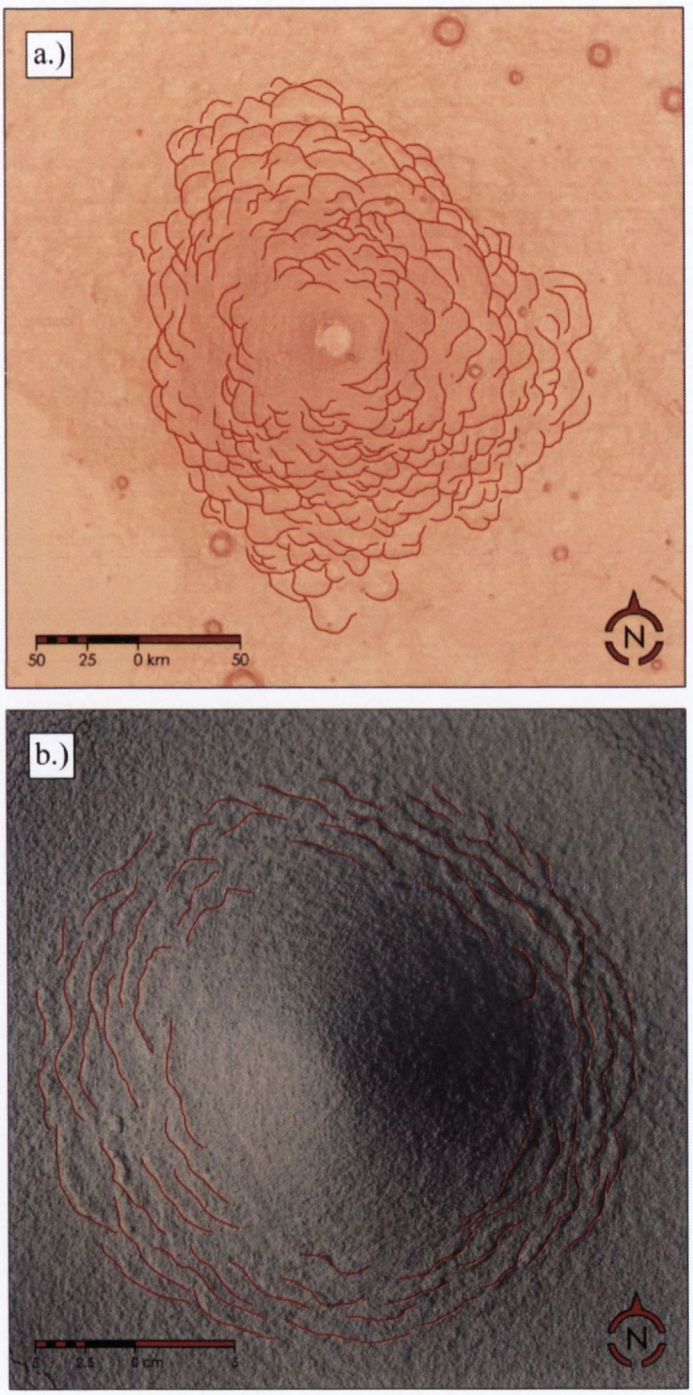

Plate 3.11. The geometric similarity between flank terraces on Mars and the convex features produced in these experiments. Both sets of structures share a convex-up morphology, and both are arranged in an imbricate pattern about conical loads. **a.)** MOLA-derived slope map of Elysium Mons volcano, with terrace boundaries overlaid (in red); and **b.)** photograph of experiment QIX. A 01, again with terrace traces.

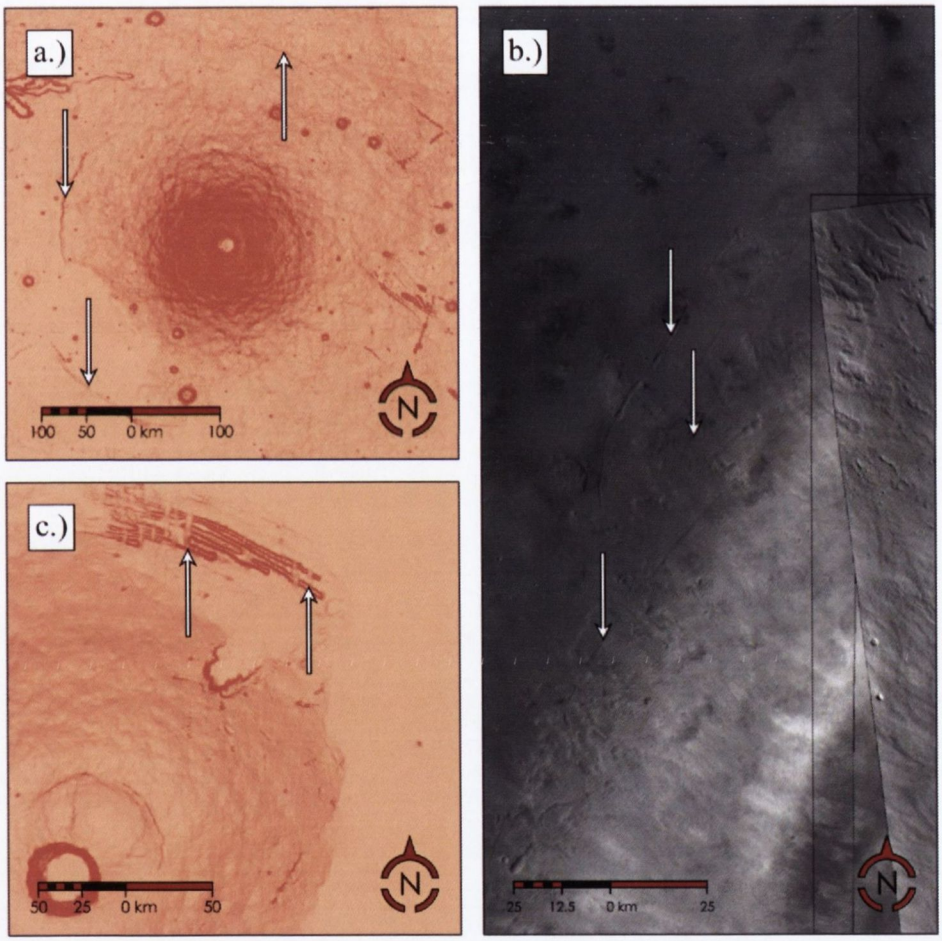

Plate 3.12. Arcuate fractures about several Martian volcanoes. These shields represent significant loads on the planet's crust. **a.)** Annular extension around Elysium Mons (indicated by the white arrowheads on the MOLA-derived slope map); **b.)** extensive graben on the NW flank and foot of Ascraeus Mons (HRSC and CTX mosaic; see Chapter 4, Plate 4.3); and **c.)** curved fractures to the NNE of the Pavonis Mons shield.

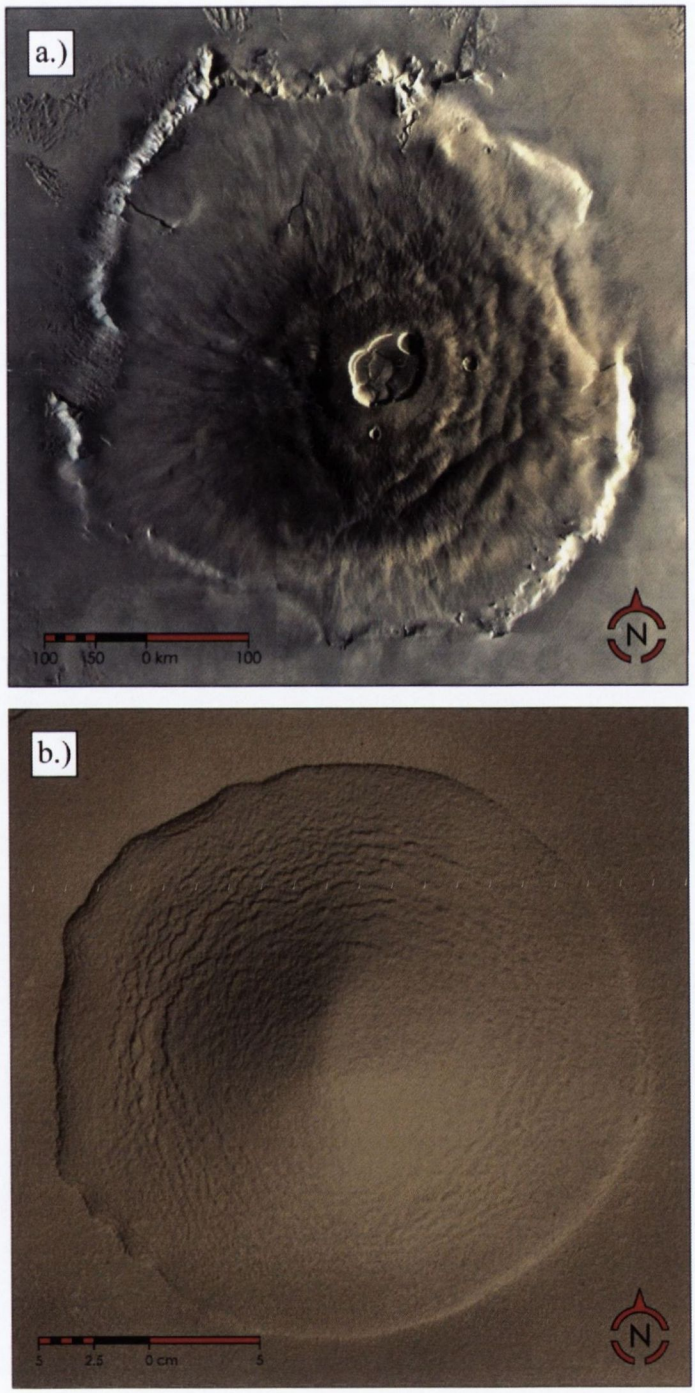

Plate 3.13. Morphological similarity between **a.)** Olympus Mons and **b.)** a basally detached flexure experiment — both constructs have a basal escarpment, concave-upward lower flanks, and terraced upper flanks. The image of Olympus is Viking Orbiter mosaic; the experiment is QlX. F 04 at T=final.

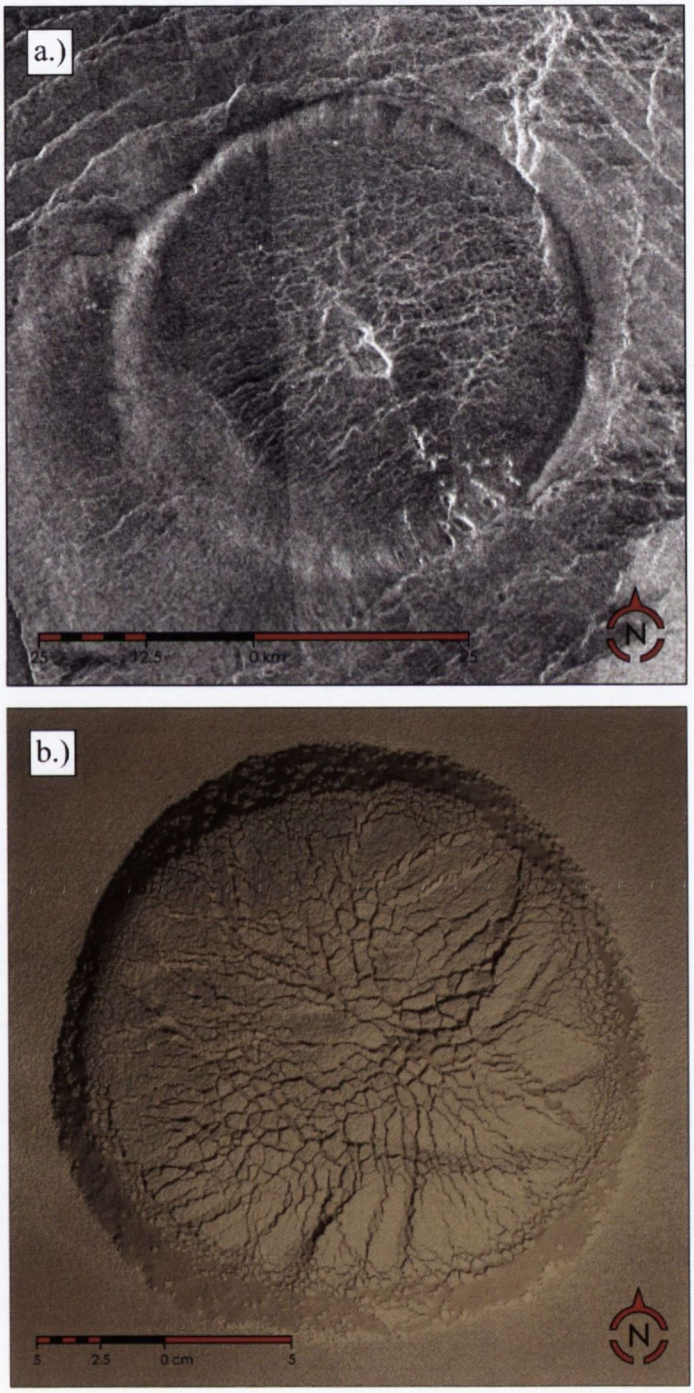

Plate 3.14. A comparison of pancake domes morphology with that of a domed, basally detached cone. Both structures are axisymmetric, have steep sides, and flat, fractured upper surfaces. **a.)** A pancake dome on Tinatin Planitia, Venus. The dome is approx. 60 km across. The image is a portion of Magellan C1-MIDR 15N009; 1, framelet 36; **b.)** experiment QlX. F 06 at T=final.

scaling parameters and ratios

Value	Symbol	S.I. Units	Model	Nature	Ratio
Length	**l**	m	1×10^{-1}	1×10^{5}	1×10^{-6}
Density	**ρ**	kg m^{-3}	1.4×10^{3}	2.6×10^{3}	5.38×10^{-1}
Gravity	**g**	m s^{-2}	9.81	3.8	2.58
Stress	**σ**	kg m^{-2} s^{-2} (Pa)	1.37	9.88×10^{5}	1.39×10^{-6}
Cohesion	**C**	kg m^{-2} s^{-2} (Pa)	1.39×10^{1}	1×10^{7}	1.39×10^{-6}
Viscosity	**μ**	kg m^{-2} s^{-1} (Pa s)	1×10^{4}	1×10^{20}	1×10^{-16}
Time	**T**	s	6×10^{2}	8.34×10^{12}	7.19×10^{-11}

Table 3.1. Scaling parameters used in this study.

qualitative experimental programme (QIX.)

Set	Name	Number
A	Simple loading	4 experiments
B	Silicone inclusions	14
C	Cone geometry	12
D	Sand thickness	9
E	Plaster thickness	6
F	Basal décollement	11

Table 3.2. List of experiment sets in the qualitative programme, and the number of experiments per set.

quantitative experimental programme (QnX.)

Experiment No.	Cone Width, ω	Cone Slope, α	Aspect Ratio (short:long)	Sand Layer?	Sand Depth, δ
QnX. 01	25 cm	33°	1:1	×	n/a
QnX. 02	25 cm	33°	1:1	✓	10 mm
QnX. 03	25 cm	33°	1:2	✓	10 mm

Table 3.3. List of experiment sets in the quantitative programme. The parameters for each experiment are also listed.

QnX. measurements

Number	Parameter	Symbol
1	Experiment datum (height of sand)	D_{exp}
2	Height of cone at start of experiment	H_{cs}
3	Diameter of cone at start of experiment*	Di_{cs}
4	Height of cone at end of experiment	H_{ce}
5	Diameter of cone at end of experiment*	Di_{ce}
6	Depth of flexural bowl	D_{fb}
7	Height of flexural bulge†	H_{fb}
8	Depth of flexural trough†	D_{ft}
9	Width of annular extensional zone†	Di_{xz}
10	Time at which terraces first developed	T_{tl}

*Measurements taken for this parameter along N-S and E-W orientations

†Measurement taken for this parameter at points N, S, E, and W

Table 3.4. The measurements taken for each experiment in the QnX. set. Length and height values for the cone before and after flexure were obtained, and the time at which terraces were first observed was also noted.

QIX. set A: simple loading

Experiment No.	Cone Width, ω	Cone Slope, α	Observation
QIX. A 01	25 cm	33°	Flexure | positive-relief flank structures | circumferential trough | annular extension
QIX. A 02	25 cm	33°	Flexure | some flank structures | trough | annular extension
QIX. A 03	25 cm	33°	Flexure | flank structures | trough | significant annular extension
QIX. A 04	25 cm	33°	Flexure | flank structures | shallow trough | annular extension

Table 3.5. Experimental results for QIX. set A.

QIX. set B: silicone inclusions

Experiment No.	Cone Width, ω	Cone Slope, α	Shape	Simulated feature	Observation
QIX. B 01	25 cm	15°	Conical	Low-strength layer	Spreading
QIX. B 02	25 cm	33°	Conical	Intrusive core	Spreading | exposure of putty
QIX. B 03	25 cm	15°	Conical	Low-strength layer	Spreading
QIX. B 04	25 cm	33°	Cylindrical	Intrusive core	Summit sank | circular depression
QIX. B 05	25 cm	33°	Tabular	Laccolith	Spreading
QIX. B 06	25 cm	33°	Ellipsoidal	Magma chamber	Nothing
QIX. B 07	20 cm	33°	Tabular	Basal décollement	Spreading | prominent leaf graben
QIX. B 08	25 cm	33°	Cylindrical	Intrusive core	Flexure | spreading
QIX. B 09	25 cm	33°	Cylindrical	Intrusive core	Flexure | spreading
QIX. B 10	25 cm	33°	Cylindrical	Intrusive core	Flexure | spreading
QIX. B 11	25 cm	33°	Cylindrical	Intrusive core	Flexure | spreading
QIX. B 12	25 cm	33°	Tabular	Magma chamber	Flexure | spreading
QIX. B 13	25 cm	33°	Conical	Low-strength layer	Flexure | no visible spreading
QIX. B 14	25 cm	33°	Conical	Low-strength layer	Flexure | spreading

Table 3.6. Experimental results for QIX. set B.

QIX. set C: cone geometry

Experiment No.	Cone Width, ω	Cone Slope, α	Parameter	Observation
QIX. C 01	25 cm	20°	Slope	Flexure | subtle flank structures | annular extension
QIX. C 02	25 cm	10°	Slope	Flexure | some flank structures | extension
QIX. C 03	12 cm	33°	Volume	Flexure | flank structures | extension
QIX. C 04	12 cm	20°	Slope + Volume	Flexure | extension
QIX. C 05	12 cm	33°	Volume*	Flexure | flank structures | extension
QIX. C 06	12 cm	20°	Slope + Volume*	Flexure | some flank structures | extension
QIX. C 07	25 cm	33°	Slope	Flexure | flank structures | extension
QIX. C 08	25 cm	30°	Slope	Flexure | flank structures | extension
QIX. C 09	25 cm	25°	Slope	Flexure | some flank structures | extension
QIX. C 10	25 cm	20°	Slope	Flexure | some flank structures | extension
QIX. C 11	25 cm	15°	Slope	Flexure | no flank structures | extension
QIX. C 12	25 cm	05°	Slope	Flexure | no structures | some extension

*Experiments QIX. C 05 and 06 were conducted with a 3 mm sand layer; see QIX. set D

Table 3.7. Experimental results for QIX. set C.

QIX. set D: sand layer thickness

Experiment No.	Cone Width, ω	Cone Slope, α	Sand Depth, δ	Observation
QIX. D 01	25 cm	33°	5 mm	Flexure | flank structures | annular extension
QIX. D 02*	12 cm	33°	3 mm	Flexure | flank structures | extension
QIX. D 03*	12 cm	20°	3 mm	Flexure | some flank structures | extension
QIX. D 04	25 cm	33°	2 mm	Flexure | flank structures | circumferential trough | extension
QIX. D 05	25 cm	33°	5 mm	Flexure | flank structures | shallow trough | broad extension
QIX. D 06	25 cm	33°	10 mm	Flexure | prominent flank structures | trough | broad extension
QIX. D 07	25 cm	33°	15 mm	Flexure | prominent structures | very wide extension
QIX. D 08	25 cm	33°	20 mm	Flexure | prominent structures | very wide extension
QIX. D 09	25 cm	33°	30 mm	Flexure | flank structures | broad extension

*Experiments QIX. D 02 and 03 also occur as QIX. C 05 and 06.

Table 3.8. Experimental results for QIX. set D.

QIX. set E: plaster layer thicknes

Experiment No.	Cone Width, ω	Cone Slope, α	Plaster depth, ε	Observation
QIX. E 01	25 cm	33°	1 mm	Flexure | flank structures | shallow trough | annular extension
QIX. E 02	25 cm	33°	2 mm	Flexure | some flank structures | broad extension
QIX. E 03	25 cm	33°	5 mm	Flexure | subtle flank structures | broad extension
QIX. E 04	25 cm	33°	10 mm	Flexure | no flank structures | very wide extension
QIX. E 05	25 cm	33°	15 mm	Flexure | no flank structures | broad extension
QIX. E 06	25 cm	33°	20 mm	Flexure | no flank structures | very wide extension

Table 3.9. Experimental results for QIX. set E.

QIX. set F: basal décollement

Experiment No.	Cone Width, ω	Cone Slope, α	Sand depth, δ	Putty depth, β	Observation
QIX. F 01	25 cm	33°	2 mm	5 mm	Flexure | flank structures | subtle basal scarp
QIX. F 02	25 cm	33°	5 mm	5 mm	Flexure | flank structures | (partial) basal scarp
QIX. F 03	25 cm	33°	10 mm	5 mm	Flexure | flank structures | basal scarp
QIX. F 04	25 cm	33°	20 mm	5 mm	Flexure | prominent scarp | broad extension
QIX. F 05	25 cm	33°	30 mm	5 mm	Flexure | prominent scarp | broad extension
QIX. F 06	25 cm	33°	60 mm	5 mm	No flexure | steep-sided dome | leaf graben
QIX. F 07	25 cm	33°	5 mm	10 mm	Flexure | (partial) subtle basal scarp
QIX. F 08	25 cm	33°	10 mm	10 mm	Flexure | flank structures | basal scarp
QIX. F 09	25 cm	20°	10 mm	5 mm	Flexure | (partial) subtle scarp
QIX. F 10	25 cm	10°	10 mm	5 mm	Flexure | some structures | very subtle scarp
QIX. F 11	15 cm	33°	10 mm	5 mm	Flexure | some structures | no visible scarp

Table 3.10. Experimental results for QIX. set F.

quantitative experimental results

Number	Parameter	Symbol	Value		
			QnX. 01	QnX. 02	QnX. 03
1	Height of cone at start of experiment (cm)	H_{cs}	4.9	6.7	3.6
2	Total height of cone at end of experiment (cm)	H_{ce}	7	8.2	7
3	Percentage increase of cone height		42.9%	22.4%	81.1%
4	Average diameter of cone at start of experiment (cm)	Di_{cs}	22.5	23.5	20.9
5	Average diameter of cone at end of experiment (cm)	Di_{ce}	21.2	22.5	20.3
6	Percentage change of cone diameter		-5.5%	-4.3%	-3.3%
7	Average height of flexural bulge (cm)	H_{fb}	0.6	1.0	0.5
8	Average depth of flexural trough (cm)	D_{ft}	-0.2	0.4	-0.6
9	Average width of annular extensional zone (cm)	Wi_{xz}	3.5	1.1	1.1
10	Time at which terraces first develop (s)	T_{tl}	120	180	120

Table 3.11. Quantitative data returned from the QnX. experimental set. Experimental results for QlX. Percentage increases in cone height and decreases in diameter are given relative to the initial value. Geometric values were measured in the laboratory; the times at which terraces first appeared were determined from time codes on photographs taken during the experiments.

introduction

nature | origin | context

conclusions

4 On the role of terraces within Martian volcanotectonism, based on a case study of the shield volcano Ascraeus Mons.

overview

Ascraeus Mons is one of the largest volcanoes on Mars. It is host to a broad range of visible, well-preserved surface structures. Features such as pit craters, graben, rilles, and flank embayments have featured in previous studies of this and other Martian volcanoes' geodynamic processes. Additionally, the flank terraces on this volcano are amongst the largest and most visible of any on Mars. Ascraeus Mons is therefore an eminently suitable candidate volcano with which to test if a flexure-induced origin for terraces is compatible with the formation of these other, better understood structures, and so serves as a case study for this work.

Two- and three-dimensional remotely-sensed data can be used to determine the spatial and temporal relationships of the entire suite of volcanotectonic structures on Ascraeus, and show that three distinct collapse events define the summit caldera complex. Extensionally-induced pit crater structures are among the most recent and abundant extensional structures on the volcano, although they are principally concentrated on the NE flank and the NE and SW embayments. Sinuous rilles are prevalent on the N flank, and show some evidence of tectonic control. Flank terraces encircle the main shield but are absent on the rift aprons. Broad, arcuate graben on the NW flanks and surrounding plains point to load-concentric extension, whilst a prominent thrust on the upper S flank attests to late-stage summit compression.

These observations can be used to develop a detailed evolutionary sequence for this volcano, and indicate that lithospheric flexure has indeed played a key role in shaping Ascraeus Mons and its surface structures. Owing to the similarities between Ascraeus and several other large Martian shields, I assert that this structural chronology may serve as a basis for determining the volcanotectonic histories of volcanoes across Mars.

1. Ascraeus Mons

As described in Chapter 2, The Tharsis Rise is the largest and youngest volcanic province on Mars. It is home to several giant volcanoes, of which Olympus Mons, offset to the NW, is the largest. To the NE, the Rise is dominated by three enormous shields, known collectively as the Tharsis Montes, aligned along a NE-SW axis. Arsia Mons is the southernmost Tharsis volcano, and, with a vertical relief of 11.7 km, is over three thousand metres taller than its neighbour, Pavonis Mons. To the NE, this triad is completed by the tallest and youngest Tharsis shield, Ascraeus Mons (**Plate 4.1**).

1.1 structural summary

Ascraeus is the third-largest volcano on Mars, with a volume of 1.1×10^{15} m^3 and a vertical relief

Elements of this chapter appear in modified form in Byrne, P. K., van Wyk de Vries, B., Murray, J. B., Troll, V.R. A volcanotectonic survey of Ascraeus Mons. Submitted to *Journal of Geophysysical Research—Planets.*

of 14,900 m [*Plescia*, 2004]. Like its Tharsis counterparts, Ascraeus has a convex-upward morphology, a summit plateau and caldera complex (**Plate 4.1: 1**), flank embayments (**Plate 4.1: 2**), and lava rift aprons [*Hodges and Moore*, 1994] to the NE and SW (**Plate 4.1: 3**). The shield is largely symmetric about the caldera complex [*Zimbleman and Edgett*, 1992]. *Scott and Wilson* [2000] identified eight discrete collapse events, sourced from both peripheral and central magma sources, whilst *Mouginis-Mark & Christensen* [2005] suggested a total of eleven. Long, ribbon-like flows, primarily sourced from flank eruptions [*Mouginis-Mark*, 1981] and characteristic of large Martian shields [*Plescia and Saunders*, 1979], are evident on the main flanks of Ascraeus. Sheet lavas derived from linear vents on the NE and SW of the edifice comprise the rift aprons [*Carr*, 1973].

Aureole deposits, similar to those observed at Pavonis and Arsia (though more areally restricted), occur at the N base of Ascraeus, on the topographic downslope of the Tharsis Rise [*Zimbleman and Edgett*, 1992]. These deposits may be due to glacial or related processes [*Hodges and Moore*, 1994]. Recent high-resolution photogeological mapping of Ascraeus indicates a transition from tube- to channel-fed eruption conditions on the main flanks, with a prevalence of tube-fed eruptions on the rift aprons [*Bleacher et al.*, 2007]. The NE lava apron is larger than that to the SW [*Plescia*, 2004], whilst the latter overprints the apron to the N of Pavonis [*Hodges and Moore*, 1994]. *Hiesinger et al.* [2007] used a flow model with data derived from photogeological mapping to calculate values for the mean viscosity and average effusion rate of lavas on the main portion of the volcano, yielding values of $\sim 4.1 \times 10^6$ Pa s and 185 $m^3 s^{-1}$, respectively.

Perhaps the most prominent surface structures on Ascraeus Mons are pit crater chains which, whilst present on Arsia and Pavonis, are much more prevalent on Ascraeus [*Hodges and Moore*, 1994]. Circular, near circular, or ovoid depressions, pit craters are distinguished from simple impact craters by the lack of a raised rim around the concavity (**Plate 4.2: 1**). Aligned groups of pits form linear crater chains (**Plate 4.2: 2**), and in many areas on the volcano, pit crater chains have coalesced to form contiguous "trough" structures (**Plate 4.2: 3**). A consensus exists that pit craters are formed by collapse into subsurface voids. Various processes responsible for the origin of these voids have been suggested, including formation due to dyke swarm emplacement [*Mège and Masson*, 1996], karst dissolution [*Spencer and Fanale*, 1990], or by extensional tectonics, either with tensional fracturing [*Tanaka and Golombek*, 1989] or dilational normal faulting [*Wyrick et al.*, 2004].

Sinuous rilles are another common surface feature on Ascraeus. Rilles are rimless channels narrower but more sinuous than pit troughs (**Plate 4.2: 4**). These structures closely resemble rilles observed on the Moon, both in terms of length and sinuosity [*Mouginis-Mark et al.*, 1984]. Volcanic processes such as ash flow erosion [*Cameron*, 1964], lava tube collapse [*Greeley*, 1971], and lava flow emplacement [*Gornitz*, 1972; *Hulme*, 1973; *Chen et al.*, 2008] have been suggested

as potential rille-forming mechanisms. Conversely, *Peale et al.* [1968] proposed that surface water flow might have led to rille formation. *Murray et al.* [2010] regard rilles on Ascraeus Mons as the products of water erosion too, formed when groundwater breaches the surface of the volcano. Both pit craters and rilles coalesce into radial or sub-radial graben, which in turn form large, V-shaped vermiform embayments midway up the SW and NE flanks of the volcano [*Zimbleman and Edgett*, 1992].

Equally prevalent but topographically subtle and laterally extensive, flank terraces are distributed across the surface of Ascraeus (**Plate 4.2: 5**). For a review of these structures see Chapter 1 (section 1, page 4), where proposed terrace formation mechanisms are discussed. DTM slope map-derived maps indicate that there are at least 142 flank terraces on Ascraeus; these structures represent folds over outward-verging thrust faults formed due to a net reduction in surface area in response to loading of the lithosphere by the volcano (see Chapter 3, section 4.4.1, page 48). High on the S flank, a mare-like wrinkle ridge circumferential to the summit complex resembles ridges on Pavonis Mons' summit [*Crumpler et al.*, 1996], and may also be due to lithospheric loading [*McGovern and Solomon*, 1993].

Crumpler and Aubele [1978] proposed an evolutionary sequence for Arsia Mons, comprising 1.) the development of the main shield through the accumulation of thick lava plains; 2.) summit subsidence due to magma chamber evacuation, possibly caused by the outbreak of parasitic eruption centres on the NE and SW flanks; and 3.) the formation of the large rift aprons to the NE and SW as volcanism continued from these lower eruption centres. These authors suggest Ascraeus and Pavonis Montes may represent the ends of the first and second stages in this sequence respectively — implying Arsia is the oldest, and Ascraeus the youngest of the three Tharsis Montes. *Bleacher et al.* [2007] also found that rift apron formation likely post-dated the main shield-building phase. Crater counts indicate that main shield building occurred between ~1.5 and ~1 Ga ago, with the latest units resurfacing the flanks during the middle to late Amazonian [*Hiesinger et al.*, 2007 and references therein].

2. methodology

2.1 dataset properties and preparation

The ESA's Mars Express High Resolution Stereo Camera (HRSC) experiment [*Neukum et al.*, 2004] served as the primary dataset in this study (Table 1). HRSC images offer extensive spatial coverage at a high level of detail — data from only six orbits are required to provide almost total coverage of Ascraeus at a nadir resolution of approximately 12 m/pixel — and so are extremely useful for this mapping work. Data from NASA's Mars Reconnaissance Orbiter Context Camera

(CTX) experiment [*Malin et al.*, 2007], at a resolution of ca. 5 m/px (**Table 4.1**), were used to supplement data loss on HRSC image h1206_0001.

As the three-dimensional Mars Global Surveyor MOLA [*Zuber et al.*, 1992; *Smith et al.*, 2001] 128 pixel/degree DTM dataset provides topographic coverage of most of Mars (see Chapter 2, section 2.1, page 17), it served as the base map in a GIS. Because terraces are not readily visible on two-dimensional photogeological images, the terrace traces for Ascraeus, mapped in Chapter 2 (section 3.3, page 19), were added to the GIS. ESRI ArcCatalog 9.1 was used to apply the IAU 2000 geographic coordinate system for Mars to all photogeological data, which were then assigned an orthographic sinusoidal projection with an east positive centre of longitude of 255.0°. The HRSC and CTX images were georeferenced to the MOLA elevation data and rectified in ESRI ArcMap 9.1, yielding the photomosaic in **Plate 4.3**.

2.2 mapping

Most mapping was performed using ArcMap 9.1's Editor and Advanced Editor functions, at a constant view scale of 1:30,000. Surface structures were mapped into polyline and polygon vector shapefiles; the entire dataset is shown in **Plate 4.4**. The mapping scale was chosen as it offers a good compromise between including larger, relevant structures and incorporating those that are too small to warrant consideration for this purpose. More expansive structures, e.g. the large graben to the NW of the volcano, were mapped at a view scale of 1: 70,000.

Structures below approx. 200 m in diameter were ignored, as were those whose provenance or extent was ambiguous, due to low quality imaging, erosion, or inundation by later volcanics. Features resembling sinuous rilles, but which are probable lava flow features [*Mouginis-Mark and Christensen*, 2005], were also ignored. Only structures with discrete boundaries were mapped as individual structures, e.g. pit craters within a larger collapse trough were regarded as belonging to that same feature, and were not counted separately.

Additionally, the scalloped texture on the volcano's NW flank does not allow unequivocal distinction between pit crater structures and collapse terrain unrelated to tectonic processes. The total number of pit craters presented here, therefore, is likely to under-represent the actual quantity of pits on Ascraeus Mons.

3. observations

A total of 4,590 separate structures were mapped on the flanks and rift aprons of Ascraeus Mons (**Plate 4.4**); individual structures within the caldera complex, such as fractures, graben, and pits, were not counted separately. Each type of structure was classified as the presumptive product of either volcanic or tectonic processes, and is presented here as such. Structures classified as tectonic in nature were further categorised as being the result of extensional or compressional mechanisms.

This classification scheme is also used in the discussion. Where given, height values are derived from the MOLA DTM, and horizontal measurements from the photogeological data.

3.1 eruptive structures

3.1.1 caldera complex

At 55 km in E-W diameter, the caldera complex of Ascraeus Mons is perhaps the volcano's most prominent feature (**Plate 4.5**). The complex on Ascraeus has been the focus of previous studies [*Mouginis-Mark*, 1981; *Zimbelman and Edgett*, 1992; *Scott and Wilson*, 2000; *Mouginis-Mark and Christensen*, 2005], which yielded between eight and eleven summit calderas. I suggest the probable existence of only three such calderas, in contrast to earlier work, based on detailed mapping of the caldera structures, experience of Terran calderas and analogue modelling [e.g. *Rymer et al.*, 1998; *Roche et al.*, 2001; *Walter and Troll*, 2001; *Troll et al.*, 2002; *Holohan et al.*, 2005], and comparative studies such as *Branney* [1995].

The main caldera is manifest as a faceted, roughly elliptical pit, with a near-circular polygonal floor and steep, inward-dipping walls (**Plate 4.5: 1**). The caldera, which has an ellipticity of approximately 0.75, is encompassed by a peripheral fault zone [*Branney*, 1995; *Holohan et al.*, 2005]. This zone of extension is characterised by a multitude of collapse pits and a set of linear graben and half-graben that define the caldera's polygonal shape (**Plate 4.5: 2**). Throws on their inward-facing bounding walls increase towards the caldera edge. Within the depression, there is a large terraced zone on the NE side, which features a dense fracture network and numerous faults (**Plate 4.5: 3**).

It is possible that this terrace represents the floor of a fourth caldera. The peripheral fault zone, however, fully encompasses this depression, and it is much more heavily fractured than the two smaller, older calderas (see below) despite all three being located on the edge of the central pit. Additionally, as a NE-SW elongate structure, the central caldera has the same orientations as the regional structural trend across the Tharsis Montes.

A larger, less fractured terrace exists on the SW wall (**Plate 4.5: 4**). Three intensely faulted zones that resemble bench-like talus deposits occur on the floor of the polygonal pit. The largest is related to the NE terraced zone and another to the SE caldera, whilst the last is on the W edge of the main pit.

Two older calderas are visible: one to the NW (**Plate 4.5: 5**), and a smaller pit on the SE side (**Plate 4.5: 6**). The northern structure is cut by the central caldera's extensional zone and its polygonal pit. The SE caldera is included within the extensional zone, and has clearly identifiable reverse and vertical faults that are cut by the central pit. A broad concentric terrace runs along its inner wall (**Plate 4.5: 7**). The additional calderas reported by other authors may in fact be terraces

within, or arcuate slumps formed by sequential collapses of, a larger caldera. Fluting occurs along the upper portions of several caldera walls, particularly on the S wall of the central pit.

The caldera floors are generally flat and featureless, though there is a very small rim or ridge near the S edge of the flat-floored central pit. Another is present in the NW caldera, where at least one wrinkle ridge is present too (**Plate 4.5: 8**). Caldera depths range from ca. 3,110 m in the case of the central structure, through 1,466 m to 818 m for the SE and NW depressions, respectively. Many radially orientated lava flows and thin sinuous rilles terminate at caldera edges, demonstrating that they were truncated by these later vertical collapse events. Some concentric fractures have possible eruptive vents (see 3.1.5), suggesting that in places magma rose along the peripheral extension zones after caldera formation [cf. *Walter and Troll*, 2001].

Several positive topographic structures that resemble wrinkle ridges are present on the planar area to the north of the caldera complex, and trend both radially and concentrically to the volcano (**Plate 4.5: 9**). Many lava flows and tubes can also be distinguished, and are distinct from the ridges. There are also a few clearly upstanding linear features visible, which could be dykes that have been eroded out and left standing above the surface. Several vents, which appear as lava ponds with an outlet into a lava flow and channel, are also seen. Most of these features are subtle, however, and this part of the summit is not clearly imaged on HRSC data; as such, a full interpretation of area is hampered at present.

3.1.2 sinuous rilles

HRSC data indicate a total of 116 sinuous rilles across Ascraeus Mons, with the majority concentrated on the NE flank. Rilles have wavelengths and amplitudes generally similar to their widths (e.g. 350 m) (**Plate 4.6: 1**). They are usually flat-floored structures that cut across the surrounding lava flows. Rilles commonly emerge from larger pit crater structures (**Plate 4.6: 2**), often connect groups of features, and can bifurcate from or merge with one other. Sinuous rille orientations range from circumferential to radial. Rilles may also have multiple orientations, abruptly changing from one to another independent of nearby structures or local topography, whilst their width and depth remain the same. In some cases, concentric rilles suddenly alter course and run downslope. These structures are distinct from smaller, sinuous channels within tube-fed lava flows on the shield, which are regarded as partially collapsed lava tubes [*Bleacher et al.*, 2007].

3.1.3 lava textures

There is a marked change in lava flow texture at the break in slope of prominent flank terraces, particularly on the E flank (**Plate 4.7**). Tube-fed flows are dominant on the lower portion of the terrace, towards the base. Flow relief is high, and individual units are often discernable (**Plate 4.7: 1**). On the flat upper surface of the lower, adjoining terrace the flows are more subdued, however,

with fewer apparent lava tubes and areas of almost no relief (**Plate 4.7: 2**). Many flows display both textures with no obvious break in continuity. This textural change spatially corresponds to the terrace boundaries identified on Ascraeus.

3.1.4 pitted terrain

Across parts of the lower S flank, areas of heavily cratered and pitted terrain were observed (**Plate 4.8**). This pitted texture extends for several tens of kilometres across the flank, and is superposed upon local pit craters and graben. The pits are generally smaller in diameter than unequivocal pit craters, ranging in width from 190 m to 350 m, and are less than 10 m deep. The structures have slightly raised rims in some instances. No clear radial distribution, relationship to other structures, or structural control is apparent. These features are mantled by the same surface deposits as neighbouring pit craters and the surrounding flanks.

3.1.5 vents

Eighteen discrete vents were observed on the surface of Ascraeus: seven on the summit proximal to the caldera complex, and eleven scattered across the NE and E flanks. The structures on the summit are largely linear and resemble fissures, and are probably related to nearby lava flows. Those on the flanks correspond to scoria cones; some appear largely intact, whilst others have been degraded and tempered by later volcanism (**Plate 4.9**). Most vents show no association with any tectonic features, though several are located close to flank terrace boundaries. The presence of parasitic cones mainly on the E half of the volcano may indicate an observational bias due to the extensive erosion and low image quality of the W flanks.

3.2 tensional structures

3.2.1 pit craters

A total of 4,166 pit structures were counted on HRSC data of Ascraeus Mons, including individual pit craters, pit crater chains, and coalesced trough structures. Pit craters range from circular to elliptical in plan view shape (**Plate 4.10: 1**). Rows of three or more pits in alignment form crater chains (**Plate 4.10: 2**), and crater chains can in turn merge to form troughs (**Plate 4.10: 3**). Some pits are inverted conical concavities and taper to a point, but most craters and troughs display U-shaped or flat floors. Very shallow floors may be the result of inundation by later lavas. Some degree of stratification is often evident within the walls of pit craters, with fluting and slumping of upper units producing talus at the base of the slopes, similar to that observed within the calderas of Ascraeus and Pavonis Montes [*Crumpler and Aubele*, 1978]; see 3.1.1. Scarps resembling normal faults often bound crater chains and troughs, resulting in a scalloped appearance. Such faults can

also cause terracing along the inner walls of troughs, and may even facilitate trough development through the collapse of material along them (**Plate 4.10: 4**). Like sinuous rilles, pit structures are superposed upon surrounding lava units, though no flows appear to have issued from the pit themselves. Typical pit crater diameters range from 190 m to 3 050 m, whilst trough length values can vary from 400 m to 55 000 m. The depths of these structures can also differ, ranging from several tens to hundreds of metres.

Pit craters, chains, and troughs occur all across the surface of Ascraeus, from the middle flanks onto the rift aprons, but are concentrated on the NE sector. Furthermore, pit crater chains are almost exclusively restricted to the flanks, whilst troughs are particularly prominent on the rift aprons, mainly to the N and SW: pit chains and craters are not as abundant there. Pit chain and trough orientations on the flanks and rift aprons trend from volcano-concentric to -radial with increasing proximity to the NE and SW flank embayment complexes. Some chains are not completely concentric but tangential, and cut across the slope. Moreover, several discrete chains are often aligned with one another despite being separated by several tens of kilometres, forming a linear set of structures extending across the volcano (**Plate 4.4**). Within the flank embayments, individual troughs may exhibit a range of orientations and abrupt changes in direction, although the overall embayment complexes are radial to the volcano. There are also several instances where pit structures are aligned with flank terrace boundaries, particularly on the E flank where such boundaries are clearly visible. Both pit chains and troughs follow these breaks in slope, and therefore postdate the flows that mantle the base of the terraces.

3.2.2 SW embayment graben

A NW-SE trending graben approximately 630 m wide is situated on the W edge of the SW flank embayment complex (**Plate 4.11**). The graben is located on a promontory bounded by two sub-radial troughs. Where the troughs meet, their walls provide a three-dimensional cross section of this part of the volcano, particularly to the SE where lighting conditions are favourable (**Plate 4.11: 1**). Its inward-dipping bounded faults are visible (**Plate 4.11: 2**), with a vertical throw on these normal faults of ca. 10 m based on measurements of the photogeological data. The upper section of the stratigraphy is dominated by a 400 m-thick packet of layers, within which some individual strata are visible (**Plate 4.11: 3**). There is a marked change in texture between these lavas and the lower, smoother portion of the trough walls (**Plate 4.11: 4**), and it is at this interface, 400 m below the graben floor, that the bounding faults meet (**Plate 4.11: 5**). The S side of the graben is a simple scarp, whilst the N side has several terraces and a potentially thrusted base (material has slumped to the graben floor along the N bounding fault). Such a configuration is created by a high-angle fault system, which is consistent with the trace of the graben fault in the E trough.

3.2.3 NW plains graben

On the W and NW flanks, and extending onto the plains, arcuate graben extend for ca. 90°, concentric to the volcano (**Plate 4.12**). The width of these structures ranges from 400 m to 1,200 m, with depth values ca. 10 to 100 m. They are wider, shallower, and more laterally continuous than the troughs observed elsewhere on the flanks. The cirque-like headwalls and fluted interior walls characteristic of pit crater structures are also absent, although pits do occur nearby, and in places are laterally contiguous with these shallow graben. The graben crosscut the plains lavas surrounding the edifice, but are covered by the collapse material sourced from the NW flank of Ascraeus [*Hodges and Moore*, 1994].

3.3 compressional structures

3.3.1 flank terraces

The 142 terraces on the flanks of Ascraeus are circumferentially arranged in an imbricate, "fish scale" pattern around the volcano, but are most prominent on the NW and SE flanks (see Chapter 2, Plate 2.10). Here, despite being draped in lava flows, terrace boundaries remain perceptible (**Plate 4.13**). On other flanks, lavas obscure terrace morphology and render them visible only on slope maps. Terraces do not appear on either rift apron. Where apparent, the change in slope between terraces is associated with a textural change (see 3.1.3). There is also a spatial correlation between terrace boundaries and the pit crater chains and graben (see 3.2.1). Flank terraces have a much larger areal extent than pit craters or rilles, with average values of 39.6 km, 9.6 km, and 1.1 km for bounding length, radial length, and vertical height, respectively (see Chapter 2, Table 2.2).

3.3.2 S flank thrust

The wrinkle-ridge structure high on the S flank of Ascraeus, noted by *Crumpler et al.* [1996], is orientated circumferential to the summit (**Plate 4.14**). This feature fits closely to the trace of a terrace identified using MOLA slope data. Its leading edge is an outward-verging, somewhat sinuous arcuate scarp (**Plate 4.14: 1**). The ridge is approximately 55 km in bounding length, with a radial width of 2 km. Superposed upon it is a multitude of smaller, sub-parallel wrinkle structures (**Plate 4.14: 2**). A back scarp faces towards the summit (**Plate 4.14: 3**). This is discontinuous and disappears at a radially orientated lava flow, which is itself cut by the outward facing scarp (**Plate 4.14: 4**). The ridge is approximately 180 m taller than the surrounding flanks.

4. discussion

4.1 eruptive structures and processes

The structure of the summit complex indicates that it is the product of one main collapse event that followed probably two smaller, earlier collapses. As most of the area around the caldera consists of flows cut by the peripheral fault zone, and only a few vents are clearly visible, there has been little eruption of material onto the flanks from the summit after caldera formation. Either eruptive volumes were sufficient to resurface only the caldera floors, or the last incidences of collapse were not accompanied by any eruptions at all, due to e.g. sub-surface magma withdrawal. The rims and wrinkle ridges in the caldera floors could have been caused by continued subsidence after the surface was formed.

The central polygonal pit is joined to the SW terrace and NE fracture zone by an anti-clockwise spiralling geometry, often seen in caldera analogue models where such fracturing is preserved [*Roche et al.*, 2000; *Holohan et al.*, 2008] which, together with the peripheral extensional zone [e.g. *Walter and Troll*, 2001], indicates that the entire ensemble is related to one collapse source. This implies that there is an elliptical, SW-NE trending intrusive complex underneath the volcano that has undergone extensive drainage. Terracing and possible flexing has occurred to the SW and NE, on the long axis of the collapse structure, in contrast to the caldera's steep short axis sides. This is consistent with a change in aspect ratio, i.e. the width of the caldera vs. the depth of the intrusive body beneath. The terraces and potential flexure point to an aspect ratio of less than 1, while the steep faults of the short axis suggest a ratio of just above 1. This structural arrangement signifies a depth of 30 to 40 km to the top of the intrusive complex, based on the results of *Roche et al.* [2000, 2001] and the observations of *Rymer et al.* [1998] and *Carter et al.* [2007]. This places the main magma chamber well below the volcano base, unless there have been large amounts of early sagging and flexure as the shield was being constructed.

Neukum et al. [2004] provide crater ages for the three calderas on Ascraeus Mons that are consistent with these observations: that is, both the NW and SE structures (**Plate 4.5: 5, 6**, respectively) are older than the central pit (**Plate 4.5: 1**), which has been given an approximate age of ~100 Ma. The discrepancy between the ages of what I regard as caldera terraces within the central depression (**Plate 4.5: 3**) and the pit floor may be due to the manner in which the caldera developed. The caldera terraces and polygonal pit probably formed during the same collapse event; if this collapse was rapid, they should have similar cratering ages. It is possible, however, that the huge collapse occurred slowly, in which case a central sagging occurred first, with the central block then becoming a discrete subsiding feature. Finally, terracing and slumping would develop [e.g. *Roche et al.*, 2001; *Geshi et al.*, 2002; *Carter et al.*, 2007]. Subsequent infilling by lava, dust, or water could alter these surfaces' derived ages, obscuring any useful relative or absolute age data for

the collapse chronology. It is also possible that the largest caldera floor, the smoothest of any on the volcano, was mantled by material that later slumped off the caldera walls. This mantling may also have occurred, although to a lesser extent, on the other caldera floors.

As a cross section through the upper three km of Ascraeus, the caldera walls present important lithological information that could be applicable to the entire volcano. The fluted texture that occurs near the caldera rims but disappears further down the walls suggests a change in competency within the edifice. The abundance of graben about the caldera complex, and the extent of the fractured slump deposits within, attest to the presence of poorly consolidated and possible ductile layers throughout the exposed volcanic sequence. The widths of these fractures and graben indicate that such ductile or low-cohesion layers lie close to the surface. The summit region of Ascraeus might therefore be composed of a brittle "carapace" of resistant layers, underlain by less competent units. Fractures, hydrothermal alteration, low-cohesion sedimentary layers, or ice might weaken these deeper strata [e.g. *Cecchi et al.*, 2004]. This rheological stratigraphy is probably also applicable to other areas where fluted upper units are observed, e.g. the walls of pit craters and graben (see 3.2.1 and 3.2.2).

Previous work has concluded that sinuous rilles on the Moon are the result of thermal erosion of terrain by high effusion-rate lava flows [*Hulme*, 1973; *Mouginis-Mark et al.*, 1984], and given the morphological similarity between lunar and Martian rilles, similar processes could act on Mars. However, *Murray et al.* [2010] used a flow model adapted from *Williams et al.* [1998] to determine the volume of eruptive material necessary to erode a specific rille on the NE flank of Ascraeus. They determined that at least 5.1 km^3 of lava would have been required to form the channel, and, in the absence of any large flows proximal to the rille, concluded that lava was not the erosive fluid responsible, and favoured water instead. Rille orientation and location are likely to have been affected by surface topography and subsurface structures. The sudden change in direction of some rilles indicates an element of tectonic control, whereby fluid flowed first along concentric lineaments within the volcano, and then downslope along its surface. Nonetheless, that the majority of rilles are aligned downslope suggests that the extent of tectonic influence upon their orientation is limited and secondary to gravity, whatever the fluid agent involved.

Lava flow textures depend upon effusion fluxes, temperature, the composition of the initial lava, and topography. The change in texture of flows across flank terraces may at least be partly controlled by the break in slope as one terrace meets another. This topographic control may cause lavas to pond on the flat, upper portions of terraces, subduing the higher-relief texture observed on steeper terrace bases. If so, lavas on Ascraeus must be extremely sensitive to topography, despite their possible moderate viscosities [*Zimbelman*, 1985; *Hiesinger et al.*, 2007], especially given a slope differential of only several degrees between terrace bases and upper flat areas. A heavily fractured terrace base could provide a greater topographic, and thus textural, contrast between the

two regions, however. Mantling by aeolian sediment may also serve to lessen flow relief, though why this process appears restricted to the flat portions of terraces instead of being ubiquitous is not apparent.

The pitted terrain observed on parts of the S flank of Ascraeus is not characteristic of lava flow textures seen elsewhere on the volcano, and shows no evidence of structural control. This texture may represent a population of secondary impact craters as observed by *Oberbeck and Morrison* [1974], or could be due to layers of ice sublimating near the surface. The pits do not appear to be related to surrounding volcanic or impact structures, however, nor does the terrain conform to classical permafrost, ice sublimation, or periglacial textures [*Squyres and Carr*, 1986; *Kargel et al.*, 2004; *Li et al.*, 2005; *Desportes et al.*, 2007]. Its provenance remains unclear.

4.2 tensional volcanotectonism

The range of pit structures observed on the flanks of Ascraeus Mons represents a continuum from single, isolated craters to laterally contiguous troughs. *Wyrick* and co-workers [2004] suggest that changes in lithology, dip, and displacement account for the variation in shape and type of structure along strike. Assuming a dilational faulting origin within a heterolithic stratigraphy, pit craters are a proxy for zones of extension within the edifice. Tensional stresses appear to be prevalent across the main flanks and the rift aprons, extending onto the surrounding plains (**Plate 4.4**). Prominent flank extension, however, contrasts with the compressional origin of the flank terraces across Ascraeus. Pits are superposed upon terraces, however, indicative of a general change in dominant flank tectonism from compression to extension at some point in the volcano's history. The alignment of pit craters with terrace boundaries (e.g. **Plate 4.13**) indicates that void, and thus pit crater formation, could have occurred with thrust faulting, or alternatively, as the terrace bounding faults were reactivated in extension.

Whilst most pit structures may share an origin due to extensional stress, other processes have acted subsequent to pit formation. Individual pits may represent a single incidence of collapse in which overlying material drains or subsides into a void; troughs are aggregates of such collapse events. Within isolated pits and troughs, such as those located high on the flanks, the slumped or collapsed material is constrained by the structure and remains at its base, with further deposition limited to aeolian activity. Yet troughs and pits that occur close to one another may be enlarged by mechanical processes such as sapping [*Laity and Malin*, 1985; *Harrison and Grimm*, 2005; *Irwin et al.*, 2006], by groundwater within the volcano [*Murray et al.*, 2010], or post-formation collapse. These structures can then coalesce to form contiguous channels through which material can be transported and deposited downslope. Individual troughs would thus have advanced towards the summit through headward erosion and undermining, whilst the large embayment complexes to the NE and SW widen with increasing radial distance (**Plate 4.4**).

Lithological layering similar to that seen within the caldera walls is also visible inside many pit craters and troughs across the volcano, i.e. packets of layered, fluted lavas atop a massive, undifferentiated unit (e.g. **Plate 4.11: 3, 4**). Slumping of the stratified units into the pits indicates poor cohesion of the upper lavas. That this lithological contrast is commonly observed suggests that it is not restricted to the summit of Ascraeus Mons, and may in fact exert control over the development of some surface structures, including the small graben within the SW embayment and the wrinkled thrust high on the S flank. Conjugate faults nucleate at the interface between two units of differing competencies. The point at which the SW graben's bounding faults meet may be such an interface, in this case at a depth of 400 m. The cross section indicates that the fault angles are inclined at about 53°, with a resultant angle of internal friction of approximately 37°. The NW-SE orientation of the graben implies slope-parallel radial extension, possibly related to that responsible for pit crater formation elsewhere on the flanks, although its inward-dipping fault planes are strong evidence of shear, not dilational, faulting.

Concentric to the volcanic load, the long, arcuate graben to the NW of Ascraeus cut, and thus postdate, the surrounding lava plains, though are in turn covered by the aureole deposits at the base of the volcano [*Hodges and Moore*, 1994]. The morphological dissimilarity between these structures and the pit troughs elsewhere on the volcano suggests that they might not share the same formation mechanism. An extensional origin is likely, however, as they are negative-topographic structures and appear to be fault-bounded. They may thus correspond to the circumferential structures predicted to form concentric to a load due to bending of the crust during lithospheric flexure, when σ_3 is horizontal and radial [*Comer et al.*, 1985; *McGovern and Solomon*, 1993; *Williams and Zuber*, 1995; *van Wyk de Vries and Matela*, 1998; *Murray et al.*, 2010]. Their bounding faults may also have nucleated at a lithological interface; their widths point to a brittle-ductile transition at a depth of several hundred metres. The underlying weaker material could be a fragmented lithology rich in ice or clay, or both. Similar graben upon the NW flanks, and thus within the current radius of Ascraeus, may be remnants of an earlier set of flexural-induced structures, covered by the subsequent growth of the volcano. In this case, flexure was an early-onset process that continued until at least the start of construction of the rift-aprons and surrounding plains.

4.3 compressional volcanotectonism

The circumferential wrinkle-ridge on the upper S flank of Ascraeus has a probable compressional origin, and is thus considered a thrust fault, due to its outward-verging, convex-upward morphology, and its resemblance to thrusts seen on volcanoes on Earth [*van Wyk de Vries and Borgia*, 1996; *Borgia and van Wyk de Vries*, 2003; *Mathieu and van Wyk de Vries*, 2009]. The paired outward- and backward-facing scarps are probably an antithetic fault arrangement relating to

a ramp-flat structure. Assuming a fault dip of ~35°, a value derived from the angle of internal friction calculated for the SW embayment graben (see 4.2), the depth to the detachment surface for this fault anticline is ca. 750 m.

The prevalence of wrinkle ridges on the structure indicates that numerous small thrusts were formed as a result of a many and thinly layered sequence, and that the entire assembly is the product of upper flank shortening. The number of thrusts present may be greater than that allowed by the resolution of the data. If so, the whole flank underwent homogenous shortening at first on numerous small, possibly conjugate thrusts. Then, with continued shortening, a major antithetic set dominated, probably above a major décollement located almost a kilometre below the surface. This depth is slightly greater than that of the SW graben, though the many smaller wrinkle ridges on the thrust indicate that there are many thinner alternating competent and incompetent layers. Such a situation has been reported at the Palaeocene Mull volcano [*Mathieu and van Wyk de Vries*, 2009].

This thrust has the same morphological signature as flank terraces on MOLA-derived slope maps of the volcano, and has been mapped as such (see Chapter 2, Plate 2.10). The flank terraces on Ascraeus, therefore, may also have had a classic thrust morphology, but were mantled and their forms softened by lavas erupted after the onset of flexure. Like the wrinkle-ridge, each terrace could consist of a series of structures instead of one larger fault, though traces of these smaller thrusts might no longer be visible. If the terraces on Ascraeus accommodated a constrictional surface strain upon the volcano, so too did the thrust high on the S flank. As this thrust has not been obscured by later lavas, however, it probably developed after most summit volcanism had come to an end [*Crumpler and Aubele*, 1978; *Bleacher et al.*, 2007], suggesting that flank compression, and thus lithospheric flexure, continued beyond the end of the main shield-building phase.

Furthermore, the lack of terraces on the NE and SW aprons provides information as to the possible timing of rift apron construction relative to that of the main shield. Terraces can form on shallow gradients such as the flanks of Alba Patera (see Chapter 2, Plate 2.7), which have an average flank slope of 1.2° [*Plescia*, 2004], yet the similarly inclined Ascraeus Mons aprons, with slopes of 1-1.5° [*Plescia*, 2004], do not express terraces. Whilst late-stage resurfacing of the aprons may have obscured what terraces had formed, leaving no trace of them on MOLA slope data, it is also possible that the rift aprons may not have had time to flex the supporting crust and develop flank terraces. This would imply that they are younger than the terraced main shield, a conclusion shared by *Crumpler and Aubele* [1978] and *Bleacher et al.* [2007] on the basis of consistent embayment of main flank lava flows by those sourced from the rift aprons.

4.4 structural synthesis

Collating these observations of Ascraeus Mons, it is possible to propose a comprehensive model for the volcanotectonic history of this volcano. I envisage that Ascraeus underwent incremental

construction within a paradigm of prolonged lithospheric flexure, with commensurate effects upon its eruptive history and the temporal and spatial development of its surface structures.

4.4.1. initial shield building

The length of time taken to develop the main Ascraeus Mons shield is a function of the range of possible effusion rates [*Plescia*, 2004; *Hiesinger et al.*, 2007]. Nonetheless, I suggest that the bulk of the edifice developed quickly with respect to the viscoelastic response of the underlying lithosphere. Initial volcanism, its location perhaps influenced by the NE trending Tharsis structural pattern [*Carr et al.*, 1977], was manifest as accumulations of thick lava plains [*Crumpler and Aubele*, 1978]. Central shield volcano construction followed, with the emplacement of basaltic lavas erupted from the summit and sourced from a major magma storage system that extended a minimum of 40 km below the surface. Whilst subject to an episodic supply of magma and long periods of repose [*Wilson et al.*, 2001], as few as three discrete collapse events may have occurred during the moderately short course of shield construction (**Plate 4.5**). These collapses were accommodated by outward-dipping reverse faults [cf. *Branny*, 1995], which then acted as magma conduits for subsequent eruptions. Mantling of the edifice by tephra and aeolian sediment, and mechanical fracturing and hydrothermal alteration of progressively deeper units due to the growth of the intrusive igneous complex and the continued emplacement of flows, led to an internal lithological stratification within the volcano (e.g. **Plate 4.11: 4**).

4.4.2. onset of flexure

As Ascraeus Mons continued to grow, the supporting crust began to flex. This may simply have been a viscoelastic response to the weight of the developing volcano. Additionally, however, a ductile layer consisting of ice-saturated regolith beneath the volcano may have undergone pressure- and magma melting, causing it to weaken and yield to the volcanic load [*Murray et al.*, 2010]. As flexure commenced, the state of stress within the edifice altered. The volcano experienced an increase in basal surface area, concomitant with a reduction in area of its upper surface due to principal stress orientations of σ_1 radial, σ_2 concentric, and σ_3 vertical [*McGovern and Solomon*, 1993; *van Wyk de Vries and Matela*, 1998]. The radial and concentric constrictional strain at the upper surface was accommodated by a system of inward-dipping, arcuate reverse faults topped by outward-verging hanging-wall anticlines (see Chapter 3, section 4.3, page 46). These thrust folds are the primary structures that formed the flank terraces upon Ascraeus.

The terrace bounding faults may have heavily fractured the volcano. If these shear fractures penetrated into the intrusive core, they may have acted as magma conduits even when active during flank compression [*Mathieu and van Wyk de Vries*, 2009]. The extent to which lavas were sourced from terrace bounding faults is not certain, however, as the flanks of Ascraeus lack many

conspicuous vents [*Mouginis-Mark, 1981*; *Mouginis-Mark and Christensen*, 2005; *Bleacher et al., 2007*; this study]. Beyond the radius of Ascraeus, the development of a flexural bulge resulted in an annular zone of extension, apparent as shallow, arcuate graben concentric to the volcano. These initial fractures were subsumed by subsequent growth of the edifice, only to be reactivated by continued flexure [*Comer et al.*, 1985], resulting in concentric graben both upon the shield and beyond it. The main shield-building phase thus continued beyond the onset of lithospheric flexure.

4.4.3. late-stage summit activity

The latest volcanism on Ascraeus Mons occurred during the late Amazonian [*Plescia and Saunders*, 1979], potentially as part of a large magmatic upwelling that resurfaced Arsia and Pavonis Montes too [*Bleacher et al.*, 2007]. These lavas were primarily sourced from the summit, mantling any structures downslope and rounding terrace morphology to form the landscape which is currently observed. Whilst the total volume of material deposited during this eruptive sequence remains unknown, it was insufficient to bury completely the flank terraces formed hitherto. (Though speculative, the terraces that remain visible today might represent the final increment of shortening upon the volcano's upper surface, or, like the load-concentric graben on its lower flanks, may be reactivated structures that formed much earlier, possibly at the commencement of flexurally induced strain.)

Extensional tectonic activity in and around the complex post-dated any summit volcanism, however. The last instances then of caldera collapse occurred either due to the withdrawal of magma from a central reservoir and its emplacement elsewhere, within or upon the volcano [*Mouginis-Mark*, 1981], or to continued collapse and subsidence without attendant volcanic activity [*Walker*, 1975]. Upper flank compression also continued after mid flank volcanism ceased, resulting in the formation of the S flank thrust, proximal to the summit (**Plate 4.14**).

4.4.4. rift apron construction

Apron construction may have occurred during the main shield-building phase [*Crumpler and Aubele*, 1978; *Bleacher et al.*, 2007], but the bulk of the aprons' volume was probably erupted during the late Amazonian — after main flank volcanism had come to an end — as evidenced by the lack of terraces on these comparatively younger structures. The weight of the volcanic load at this point prevented magma from reaching the summit along existing conduits (which could have been closed due to flexural compression), resulting in the shift of eruptive centres to the lower flanks.

The hiatus between main flank and rift apron volcanism may reflect the time taken for magma to establish new routes to the surface, and, as suggested by *Bleacher et al.* [2007], may be related to completely different magma production events for which Amazonian magma ascension followed

the already established Tharsis Montes pathways. The location of rift apron activity, on the NE and SW of Ascraeus, was influenced by the regional topography of, and subsurface structures throughout the Tharsis Rise [*Carr et al.*, 1977; *Wilson and Head*, 2002]; the latter included a low-viscosity zone beneath the volcano that acted as a pathway for magmatic ascent and emplacement [*Wilson et al.*, 2001].

Water also played a significant role in shaping the volcano at this point. At least some rift apron flows were mudflows and lahars [*Murray et al.*, 2010], sourced from ice-rich layers in the crust beneath Ascraeus, and water stored within its flanks [*Scott and Wilson*, 1999; *Mouginis-Mark and Christensen*, 2005]. Additionally, the late Amazonian-aged fan-shaped deposits extending from the NW flanks show evidence of volcano-ice interaction [*Parsons and Head*, 2005; *Kadish et al.*, 2008]. The proximal ridged terrain on the NW flanks may also have been formed as deposits from water-rich sediment rapidly released from inside the volcano [*Morris et al.*, 2003]. Furthermore, sinuous rille formation occurred after the main shield-building phase, penecontemporaneous with rift apron construction. Rilles incised meandering and braided channels into the last Amazonian units to be emplaced upon both the main flanks and rift aprons, indicating an increased presence of groundwater within and beyond the shield.

4.4.5. summit subsidence and surface extension

Lithospheric flexure continued throughout this time, with load-concentric graben developing upon the plains surrounding Ascraeus Mons (**Plate 4.12**). The final stage of volcanotectonic deformation on Ascraeus saw an extensional stress applied to the upper surface of Ascraeus, resulting in the development of fractures within the construct with near-circumferential orientations on the main flanks and near-radial along the rift apron axes. Faulting and fracturing along these structures created voids into which overlying material slumped and collapsed. This resulted in the formation of pit crater structures, with a tendency towards crater chains on the main flanks, and pit troughs on the rift aprons and surrounding plains. Existing planes of weakness within the volcano, such as the fracture zones surrounding each terrace, or older flexure-induced grabens now within its radius, may also have been exploited during this extensional phase. Subsequent erosion and collapse expanded the footprint of these structures, forming coalesced networks of pit troughs to the NW and SW of the main shield.

There is no clear evidence as to why there was a change in the state of stress within the volcano at this point. If the pit craters are the superficial expressions of a dike swarm injected into the edifice, it would mean a further and yet unrecognized period of volcanism on Ascraeus Mons, a volcano that previously experienced pervasive compressive stresses. Moreover, no flows appear to have originated from the pits. *Montési* [2000] suggested that the plains lavas surrounding Pavonis Mons may have buried its lower flanks while the central part of the volcano remained free, thereby

applying a tensional stress to its upper surface. Similar plains lavas encircle Ascraeus, so this process may be equally relevant there. Alternatively, the volcano's position atop a topographic ridge may have induced a NW-SE tensional stress across its upper surface, accounting for the greatest concentration of extensional features along a NE-SW axis. This effect could be considered a form of flank spreading, though notably there is no indication of the characteristic "leaf gräben" associated with volcanoes known to be spreading [*Borgia*, 1994; *Merle and Borgia*, 1996]. If this process is responsible for pit crater formation, however, its resultant tensional stress may have existed for as long as has the topography surrounding Ascraeus, expressed only when the flexural response was exhausted, but without further evidence this possibility remains conjecture.

The final units to develop within the Ascraeus Mons system were fields of low shields and their associated products distal to the apron margins [*Bleacher et al.*, 2007; *Hughes et al.*, 2008]. Emplaced along existing magma ascension pathways, this late and low-volume volcanism reflected the waning supply beneath the Tharsis Montes as the late Amazonian magmatic event shut down.

4.5 applicability beyond Ascraeus Mons

This volcanotectonic sequence is based upon observations of Ascraeus Mons alone, but may be applicable to volcanoes across Mars. Ascraeus is morphologically similar to the other two Tharsis shields, Arsia and Pavonis Montes [*Carr et al.*, 1977; *Plescia*, 2004], and shares with them a range of superficial structures, including NE trending rift aprons, concentric graben, NW flank aureole deposits, summit calderas, pit crater structures, and imbricate flank terraces [*Crumpler and Aubele*, 1978; *Comer et al.*, 1985; *Hodges and Moore*, 1994; *Crumpler et al.*, 1996; *Wyrick et al.*, 2004; this study, Chapter 2]. This structural similarity led *Crumpler and Aubele* [1978] to place all three Tharsis Montes within the same developmental sequence. It should be noted, however, that whilst these authors regarded Ascraeus as being the least structurally evolved of the three, this volcano shares the same gross structural features as the other Montes.

The processes that have shaped Ascraeus Mons then probably differ from those of Arsia and Pavonis only in terms of duration and extent but are otherwise equally applicable. Furthermore, flank terraces occur on volcanoes other than the Tharsis Montes, including Alba Patera, Albor Tholus, Elysium Mons, Hecates Tholus, Olympus Mons, and Uranius Patera, indicating that, at the least, these shields have also experienced the effects of lithospheric flexure. Therefore, whilst the tectonic and magmatic development of a given volcano may differ from that of Ascraeus Mons, this model establishes a framework for understanding the volcanotectonic histories of a range of volcanoes across Mars.

5. concluding remarks

Recently-available high-resolution photogeological data has enabled the comprehensive mapping of the surface structures of Ascraeus Mons. The number, spatial distribution, and temporal relationships of the volcano's summit calderas, pit crater chains, sinuous rilles, flank terraces, and encircling graben have been described. A synthesis of these observations provides a developmental model for Ascraeus, involving construction of the edifice within a context of lithospheric flexure.

Nascent volcanism established a broad construct of summit-derived eruptives above a large intrusive complex several tens of kilometres below the surface. Three incidences of caldera collapse occurred during shield construction, and progressive loading led to flexing of the viscoelastic lithosphere and removal of the cryosphere beneath the volcano. This in turn applied a radial and concentric constrictional strain to its upper surface, which was accommodated by outward-verging flank terraces. Flexure and surface contraction continued beyond the last phase of summit volcanism, forming circumferential graben about Ascraeus and thrusts on its flanks. Later activity switched to the volcano's periphery due to compression within the edifice, and resulted in the formation of extensive rift aprons. Continued sinking of the intrusive complex led to a tensional strain across the lower flanks and aprons that formed pit craters and troughs, whilst sinuous rilles probably developed due to late-stage water eruptions from within the volcano.

I conclude, therefore, that sustained flexure of the underlying lithosphere has played a dominant role in shaping Ascraeus Mons, influencing the location, timing, and form of many of the volcano's structures. Whilst these findings relate specifically to this volcano, they may be applicable to others on Mars, and beyond.

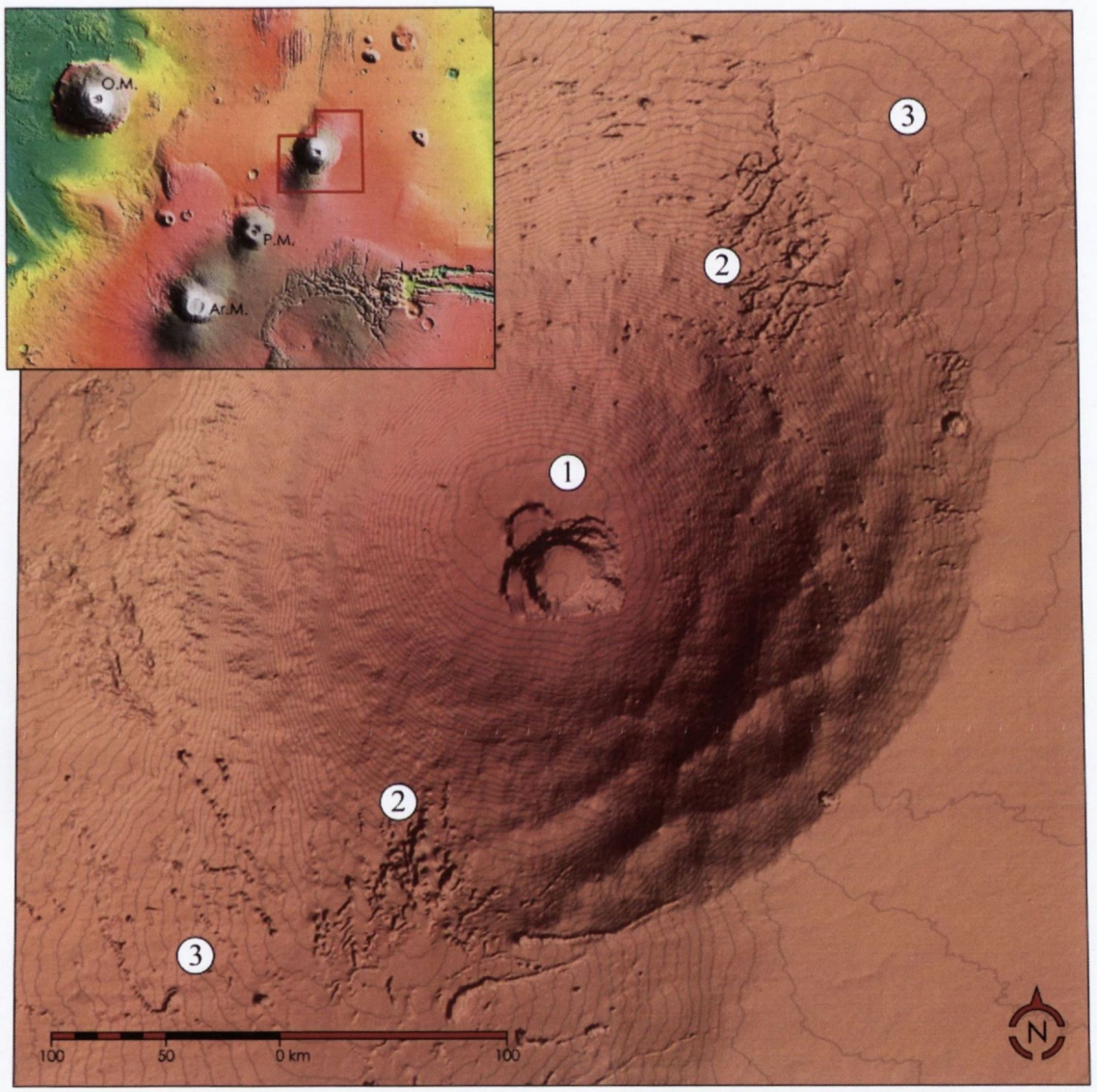

Plate 4.1. A MOLA-derived hillshade map of Ascraeus Mons. Key morphological features are shown: (1) the planar summit with caldera complex; (2) the NE and SW embayments; and (3) the NE-SW trending rift aprons. Contours have 1000 m intervals. The map is shown with a sinusoidal projection. Inset: a portion of the global MOLA elevation map, showing the location of Ascraeus Mons (outlined) with respect to Arsia Mons (Ar.M.), Pavonis Mons (P.M.), and Olympus Mons (O.M.). Inset image credit: JPL/NASA.

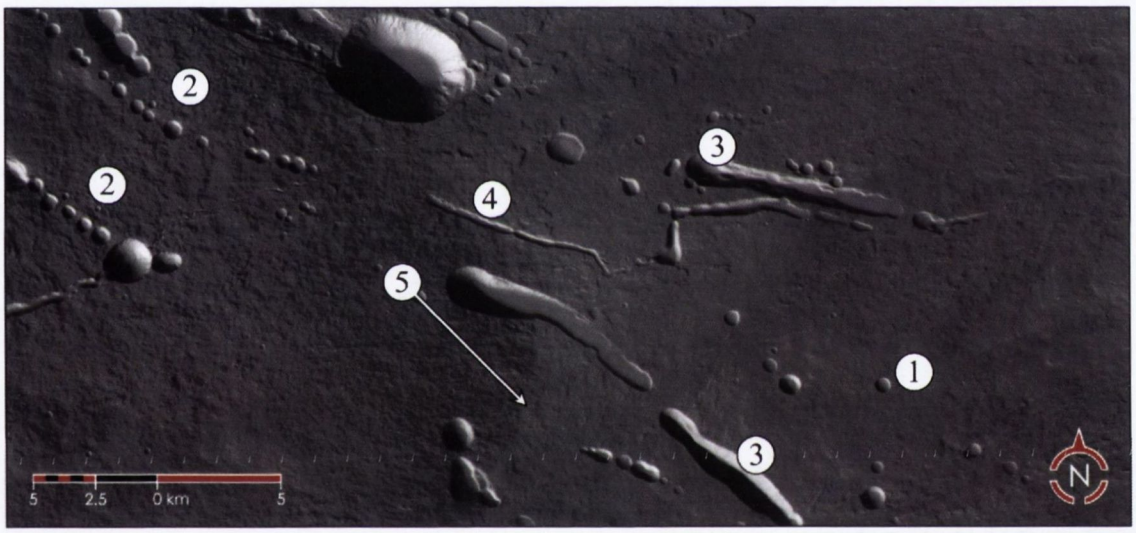

Plate 4.2. Examples of the principal surface structures on Ascraeus Mons: (1) pit crater, a discrete depression without a raised rim; (2) a series of pit craters aligned to form a chain; (3) pit trough formed from the coalescence of a crater chain; (4) sinuous rille, in this case with a downslope orientation and merging with a pit trough; and (5) flank terrace boundary, barely visible on photogeological data but characterised by an arcuate break in slope. The area shown is a portion of HRSC image h2054_0001.

Plate 4.3. Photomosaic of the HRSC and CTX images used in this study. The broad, vertical strips are HRSC data, whilst the diagonal, thinner strips are CTX. Arranged left to right, portions of HRSC images h1217_0001, h1206_0001, h0068_0000, h0016_0008, h2054_0001, and h2032_0001 are used. CTX images P02_001708_1889, P06_003330_1890, and P13_006165_1914 complement HRSC. The map is displayed in a sinusoidal projection, with an east positive centre of longitude of 255.0°. The boxes indicate the locations of Figs. 2, 5, 6, 7, 8, 9, 10, 11, 12, 13b, and 14.

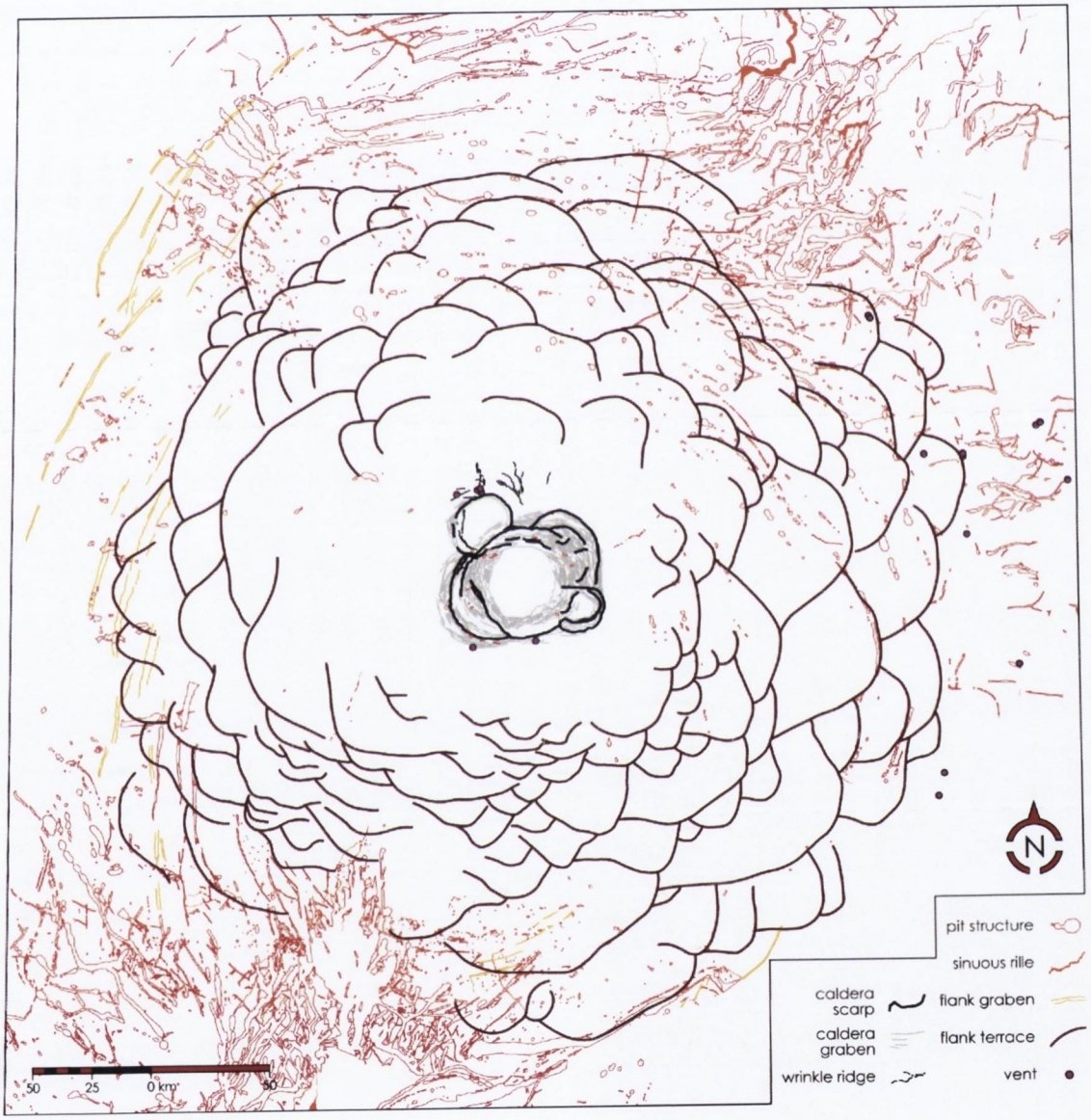

Plate 4.4. GIS dataset of all surface structures on Ascraeus mapped in this study. The map has the same projected coordinate system as that of **Fig. 3**.

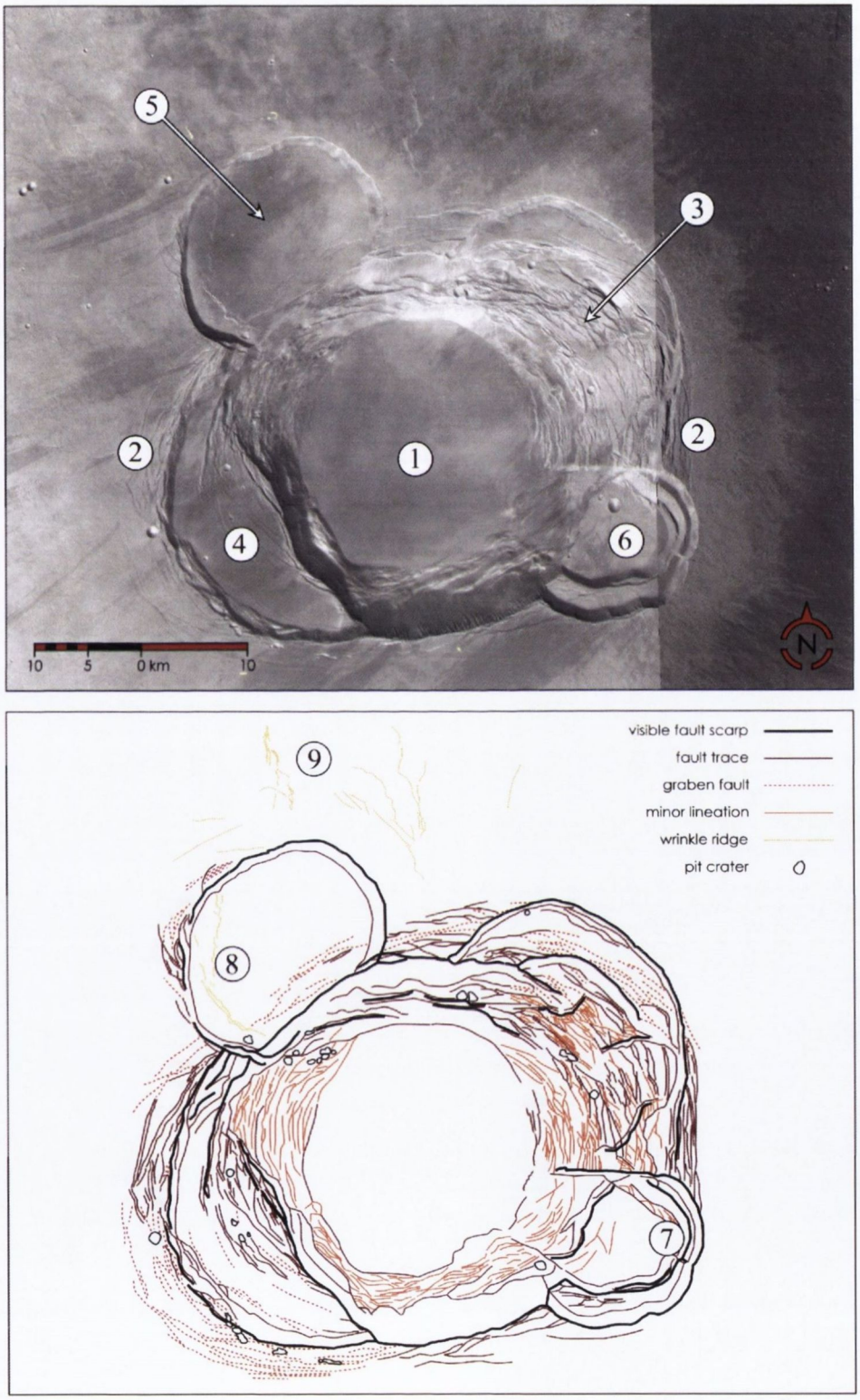

Plate 4.5. HRSC summit caldera mosaic (top), and a comparative sketch (bottom). The central polygonal pit (1) is enclosed by an elliptical peripheral fault zone (2). Also visible are the large, fractured terraces within the main caldera (3 and 4), and the two older calderas, to the NW and SE (5 and 6, respectively). At least two incidences of collapse have occurred within the SE caldera (7), whilst surface contraction has led to the formation of wrinkle ridges (8 and 9). HRSC images h0068_0000 and h0016_0008.

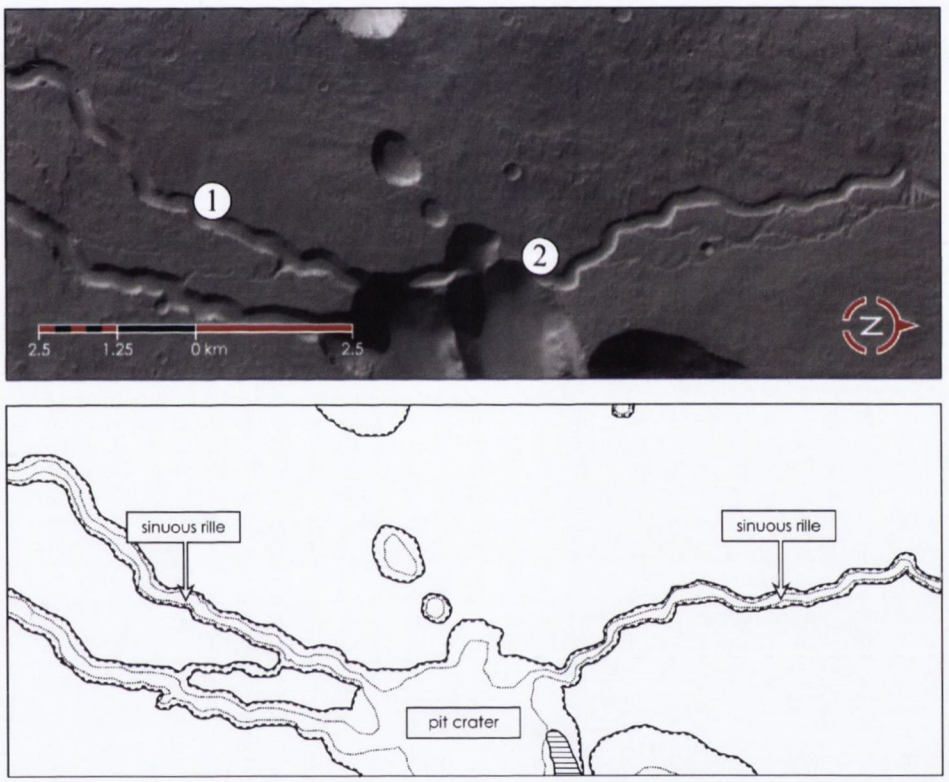

Plate 4.6. An example of one of the eruptive structures on Ascraeus Mons, this sinuous rille lies on the NE flank. The rille's width is comparable to its amplitude (1). This example also intersects the S edge of a pit crater, and reappears beyond the crater's N wall (2). HRSC image h2054_0001. In this and all subsequent sketches, solid lines outline each structure. Dotted lines delineate the structures' floors. Ticks indicate the edge of negative relief structures. Scree deposits are shown with a horizontal swatch.

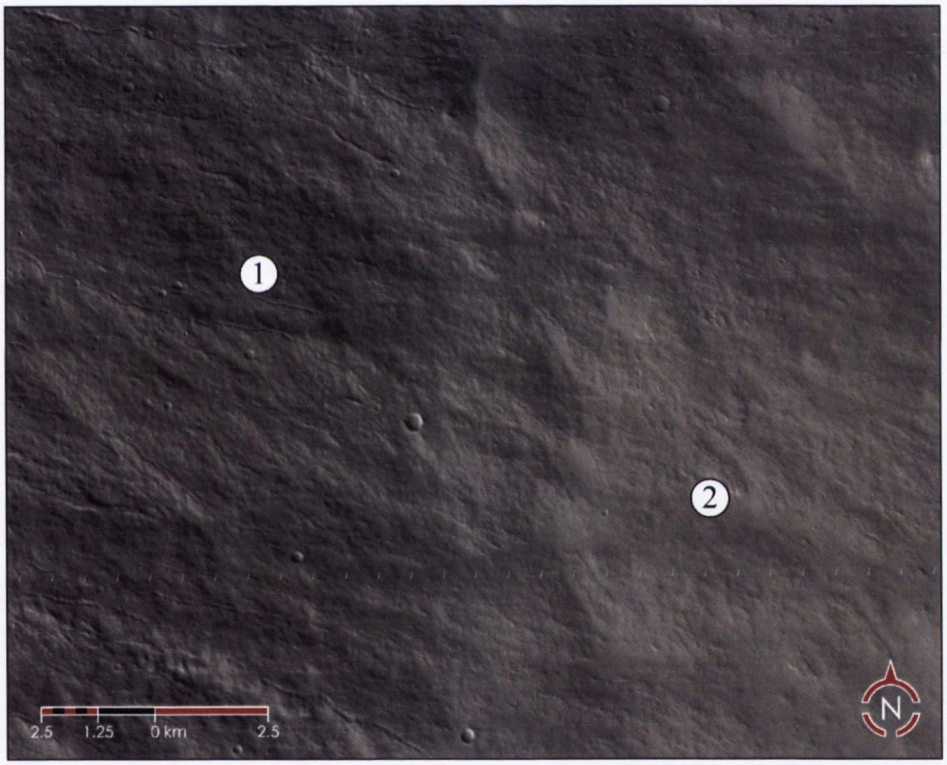

Plate 4.7. The contrasting surface texture at the base of a flank terrace on the E flank. Tube-fed flows have high-relief on the terrace nose (1), whilst the flat portion of the adjoining terrace is topographically muted (2). HRSC image h2054_0001.

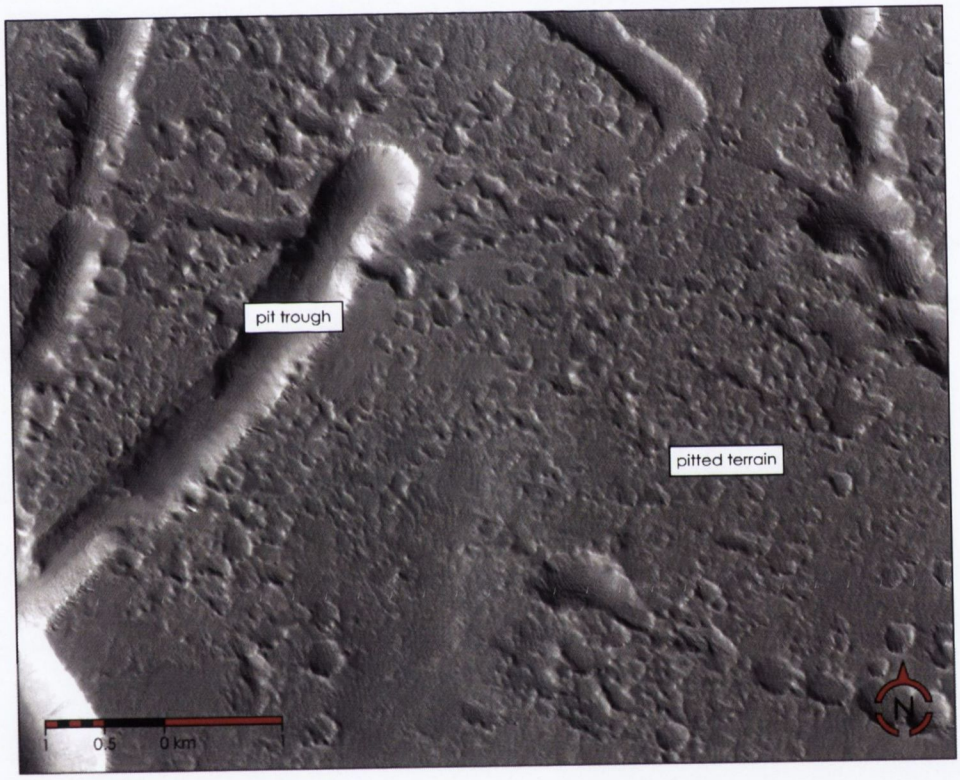

Plate 4.8. An example of the pitted terrain on the SW embayment, set amidst pit trough structures. CTX image P06_003330_1890.

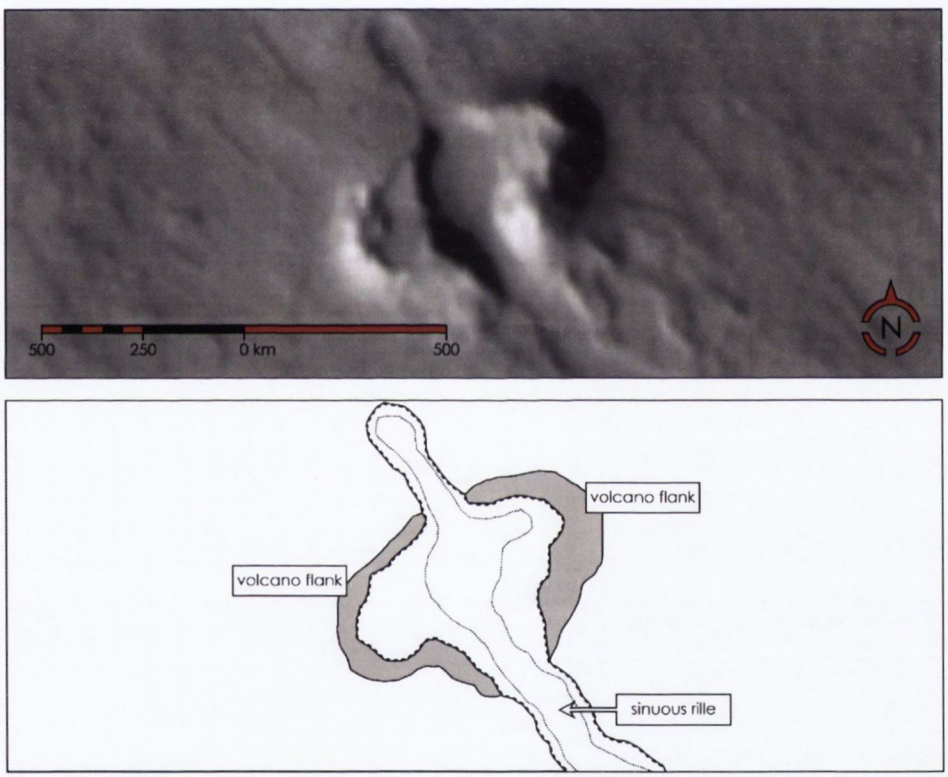

Plate 4.9. A parasitic vent on Ascraeus, in this case on the SE flank. This cone has been dissected by a NW-trending sinuous rille. The vent's flanks are shown with a grey fill. HRSC image h2032_0001.

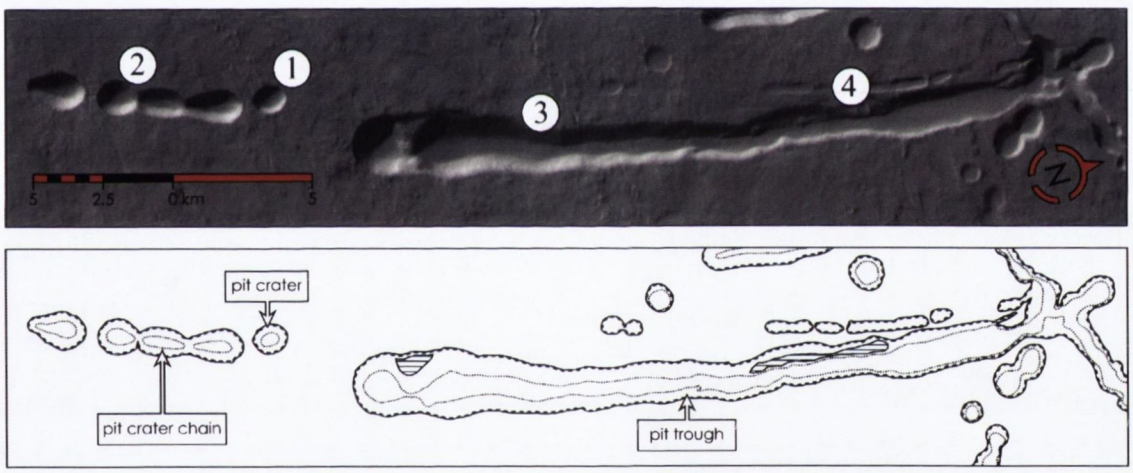

Plate 4.10. A group of pit crater structures, including: (1) an individual pit crater; (2) a crater chain; and (3) a coalesced pit crater trough. This latter type of structure is commonly bounded by scarps interpreted as normal faults, which appear to facilitate trough formation and are often accompanied by talus deposits (4). HRSC image h2054_0001.

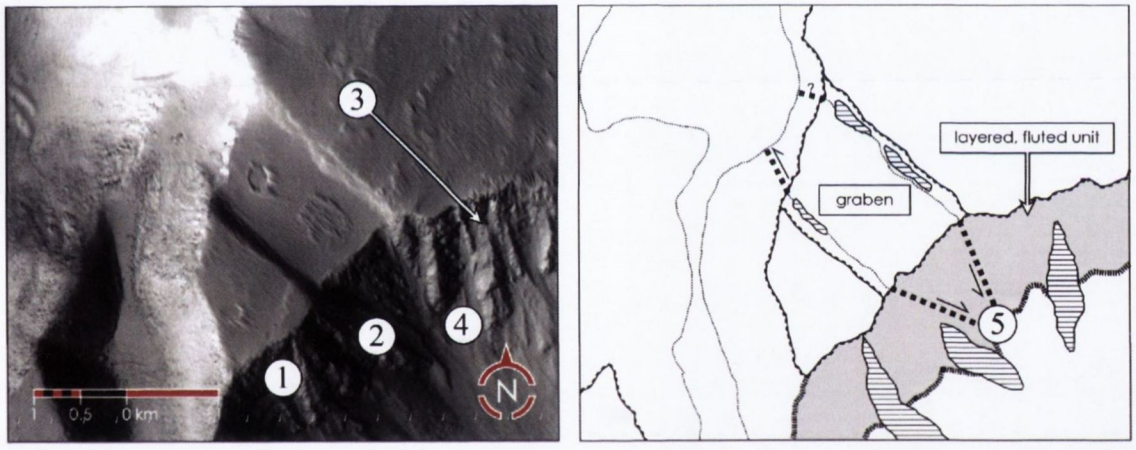

Plate 4.11. A portion of a CTX image showing the NW-trending graben within the SW embayment complex. Erosion has provided a cross-section of this structure (1 and 2), which clearly shows a layered, cohesive unit (3) above a more massive unit (4); the graben's bounding faults appear to nucleate at their interface (5). The visible extent of the layered, fluted unit is marked by a heavy, hatched line. CTX image P06_003330_1890.

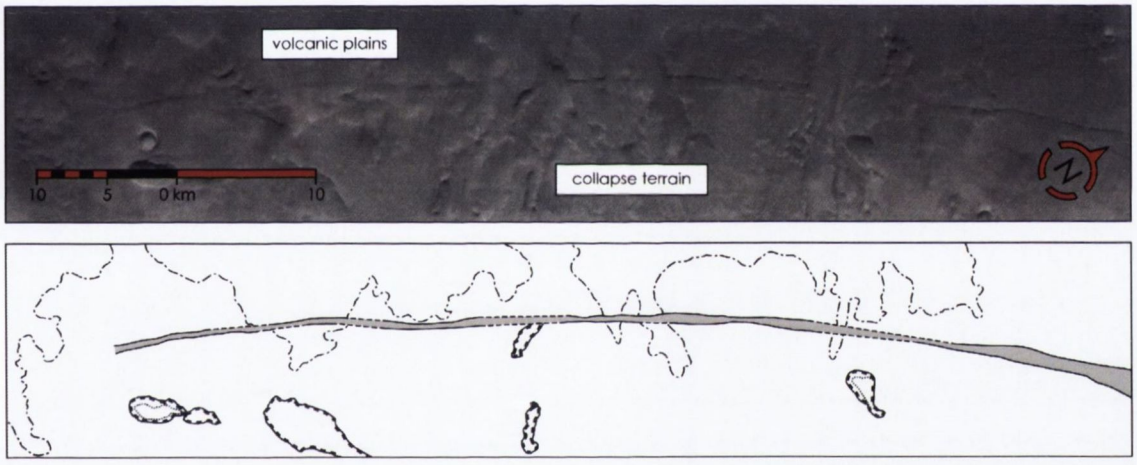

Plate 4.12. An example of a load-concentric graben to the volcano's NW. HRSC image h1217_0001.

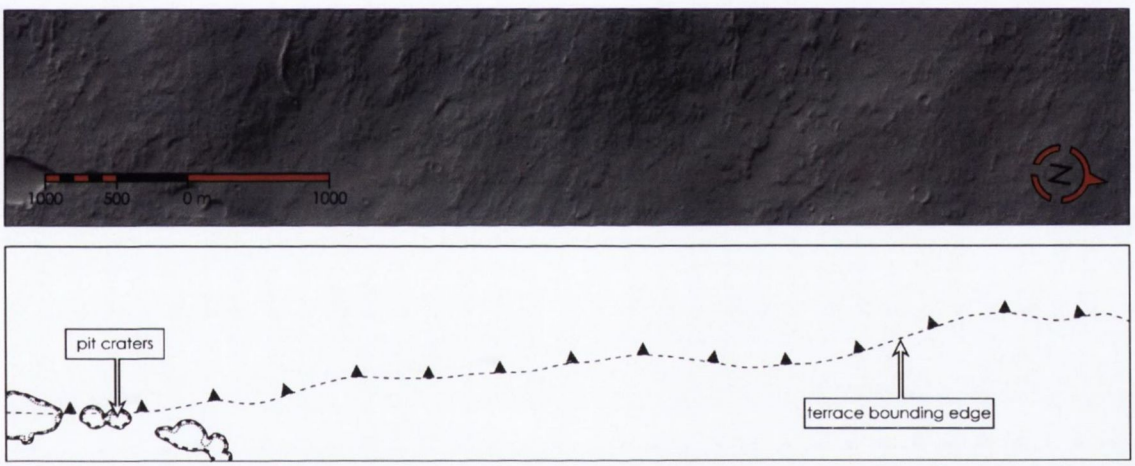

Plate 4.13. An example of a terrace boundary viewed with two-dimensional photographic data. The break in slope as one terrace meets another is visible, but fully differentiating these structures is difficult. A dashed line and closed teeth denote the presumed thrust fault's surface trace. Note the occurrence of pit craters proximal to the terrace base. HRSC image h2032_0001.

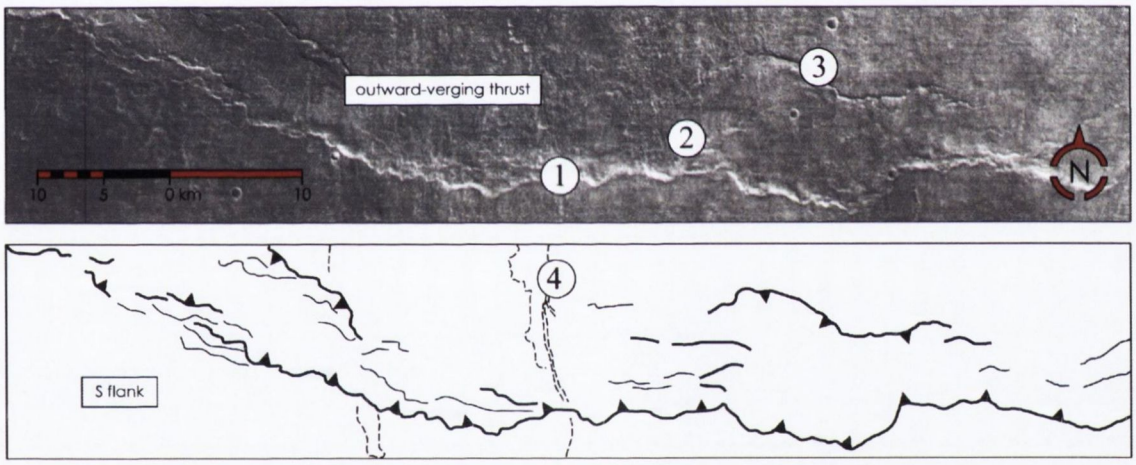

Plate 4.14. A portion of HRSC image h0068_0000 showing the S flank thrust system, with arcuate front scarp (1), sub-parallel wrinkle ridges (2), and back scarp (3) that terminates at a summit-derived tabular lava flow (4).

High Resolution Stereo Camera (HRSC) image data		
Image Number	**Resolution (m/px)**	**Coverage**
h0016_0008	12.3	E side of caldera and E proximal flank
h0068_0000	12.4	Caldera and volcano centre
h1206_0001	12.2	Medial W flank and SW embayment
h1217_0001	12.1	Distal W flank and plains
h2032_0001	12.2	Distal E flank and plains
h2054_0001	12.2	Medial E flank and NE embayment
Context Camera (CTX) image data		
P02_001708_1889	5.1	SW embayment
P06_003330_1890	5.1	Medial W flank and SW embayment
P13_006165_1914	5.1	Medial W flank and SW embayment

Table 4.1. Properties of the HRSC and CTX data used in this study. All data herein were geometrically calibrated prior to utilisation. Resolution values are those after reprojection, and are derived from the header information for each file. Only six HRSC images were required to provide coverage of almost the entire shield.

introduction

nature | origin | context

conclusions

overview

To understand the sequential development of a volcano on any planet, it is necessary to first establish the provenance of its structures. The results of remote-sensing mapping and laboratory modelling described in this thesis provide new information on the nature, origin, and structural context of previously enigmatic volcanotectonic structures.

Flank terraces are fundamental volcanotectonic structures, formed on the surface of a conical volcanic load when it flexes the supporting lithosphere. The presence of terraces on volcanoes of different ages, sizes, and locations across Mars shows that flexure is a common process. Though terraces can influence the location and form of other structures on a volcano, their greatest contribution is as an indicator of lithospheric flexure. Flexure can have a profound effect on the magmatic and tectonic development of a volcano; recognising that this process has occurred provides a framework for understanding the volcano's developmental history.

1. thesis summary

This study addresses volcano flank terraces on Mars, and uses two complementary methods — photogeological mapping and analogue modelling — to answer three fundamental questions concerning flank terraces:

- what is the geometry of flank terraces?
- what is the causal mechanism of terrace formation?
- what is the role of terraces within Martian volcano evolution?

Each question forms the basis of a core chapter in this thesis. The major findings from each chapter are presented here, in order to answer these questions.

1.1 what is the geometry of flank terraces?

Volcano flank terraces have a geometry consistent with that of thrust faults. Photogeological observations demonstrate that they are convex-upward, outward-verging structures that are systematically distributed in an imbricate "fish-scale" pattern on each volcano upon which they occur. Terraces are scale-invariant structures, maintaining a characteristic shape across a range of sizes. They are also ubiquitous structures, visible on many large shield volcanoes on Mars. Terraces are also apparent on at least three Terran volcanoes.

Though several mechanisms have been proposed to account for terrace formation, it has not been possible to appraise these hypotheses without a comprehensive understanding of terrace geometry. This work demonstrates that terrace morphology and distribution is inconsistent with most predicted structural geometries, but is compatible with an origin due to lithospheric flexure.

1.2 what is the causal mechanism of terrace formation?

Lithospheric flexure is the likely formation mechanism of flank terraces on Mars. Scaled analogue models serve as a basis for understanding how terraces form. When a brittle sand cone is placed upon a ductile silicone putty reservoir, the load sinks and flexes the silicone. The cone is constricted, and a radial and concentric shortening is applied to its upper surface. A series of inward-dipping shear fractures form within the cone to accommodate this surface strain, and are topped by convex-upward, outward-verging structures in an imbricate distribution. These features have a geometry very similar to that of flank terraces.

There is evidence that flexure has occurred on Mars. Arcuate graben encircle some of the largest Martian volcanoes, whilst topographic data indicate the presence of shallow troughs around others. Together, these observations show that lithospheric flexure provides a mechanical means by which terraces can form, and that this process is applicable to Mars.

1.3 what is the role of terraces within Martian volcano evolution?

Terraces serve as indicators that a volcano has undergone lithospheric flexure. Photogeological data of a case study volcano, Ascraeus Mons, suggest that terraces have also influenced the development of other surfaces structures. Pits, pit crater chains, and sinuous rilles all show a spatial correlation with terrace boundaries.

More pronounced, however, are the morphological effects on the cone due to flexure. This process accounts for the switch in volcanism from the summit to the lower flanks, which shut off summit activity and established large rift aprons at the foot of the volcano, as well as arcuate fractures concentric to the load. As terraces denote that flexure has occurred, their presence on this volcano provides a framework with which to view its surface structures, and hence its developmental history.

2. limitations of the methods used

2.1 photogeology

The identification of terraces on Mars and Earth is reliant on the use of three-dimensional Digital Terran Models (DTMs). DTMs can suffer from interpolation artefacts, orbital constraints imposed upon the imaging spacecraft, and atmospheric effects, however [cf. *Smith et al.*, 2001; *Farr et al.*, 2007]. The number of terraces on a given shield, therefore, and indeed the number of terraced volcanoes on Mars is probably underrepresented by the MOLA dataset. Similar considerations apply to the SRTM dataset for Earth. The Magellan SAR dataset for Venus provides topographic coverage for a third volcanic world [*Saunders and Pettenghill*, 1991], but its resolution may not be sufficient to reveal terraces should they be present.

2.2 analogue modelling

The accuracy of an analogue model is inherently limited by the degree to which it can be scaled to a natural system. This issue is compounded when the values of that system are not well understood. For example, the viscosity of the Martian lithosphere influences the speed of its flexural response, in turn affecting the rate at which terraces form. Without reliable estimates for this value, however, the experiments described here provide only a first-order insight into the dynamic properties of flexure on Mars.

Limitations innate to the experimental media also apply, particularly with regard to the granular, low-cohesive nature of the quartzose sand used to simulate competent rock. The sand may accommodate flexure-induced strains volumetrically or by grain flow, precluding the formation of discrete fault planes within the cone. Additionally, the low cohesion sand renders any attempt to cross-section a given model impossible.

3. suggested further work

3.1 photogeology

The challenges faced by existing DTM data may be overcome in part by the use of higher-resolution data to resolve terraces and terraced volcanoes on Mars. The recent availability of HRSC [*Jaumann et al.*, 2007] and HiRISE [*Li et al.*, 2007] topographical data derived from stereo photogrammetry could help in this respect.

Extending the search to other volcanoes on Earth is a natural progression from the work presented here. If terraces are a fundamental volcanotectonic structure then they should be expressed on a diverse range of Terran volcanoes, as on Mars. A methodical approach using SRTM or newly-available ASTER GDEM data could yield important information about the nature of flank terraces on Earth, which could be augmented by fieldwork and in-situ measurements. This work can even be extended to Venus by utilising the Magellan dataset to search for terraces there.

3.2 analogue modelling

Though subject to the limitations described above, the experimental setup used in this work could be modified to investigate the effects of yet more parameter variations. A silicone-iron filings mix would simulate a heavy intrusive core, in order to examine how extensional surface strains would be manifest as the core sinks (see Chapter 4, section 4.4.5, page 71). Incremental loading of a ductile substratum could be addressed too, and may represent more accurately the process of loading on Mars [*McGovern and Solomon*, 1993].

The use of larger model cones to simulate flexure and terrace formation could provide the means to resolve terraces on models with slopes approaching those of Martian volcanoes, though

this approach would require significant investment in experimental equipment and construction methods. The effect of regional deformation upon a cone, with and without flexure, represents a further technical challenge but may test the hypothesis that upper flank shortening, and thus terrace formation, could be accomplished via regional tectonism (see Chapter 2, section 4.5.3, page 26).

The influence of a basal décollement upon the flexural response could be examined further, by modelling a detachment surface with a much greater areal extent than the cone; this would represent a rheological contrast not innate to the volcano but due to regional-scale processes [e.g. *McGovern and Morgan*, 2009].

In an effort to further quantify these experiments, point-tracking software could be used to characterise surface deformation in the experiments through time. This approach would provide useful information on the strain amounts and concentrations within the experiment as flexure progresses. Additionally, stereo photogrammetry [cf. *Cecchi et al.*, 2003] could be used to generate 3D models of the experiments, enabling a direct comparison of morphometric data between laboratory terraces and those on Mars and Earth.

introduction

nature | origin | context

conclusions

references cited

Albee, A. L., Arvidson, R. E., Palluconi, F., Thorpe, T. (2001) Overview of the Mars Global Surveyor mission. *Journal of Geophysical Research*, **106**, 23,291-23,316.

Belleguic V., Lognonné, P., Wieczorek, M. (2005) Constraints on the Martian lithosphere from gravity and topography data. *Journal of Geophysical Research*, **110**, doi:10.1029/2005JE002437

Blasius, K.R., Cutts, J.A. (1981) Topography of Martian central volcanoes. *Icarus*, **45**, 87-112.

Bleacher, J., Greeley, R., Williams, D., Cave, S., Neukum, G. (2007) Trends in effusive style at the Tharsis Montes, Mars, and implications for the development of the Tharsis Province. *Journal of Geophysical Rsearch*, **112**, doi:10.1029/2006JE002873.

Borgia, A., Ferrari, L., Pasquarè, G. (1992) Importance of gravitational spreading in the tectonic and volcanic evolution of Mount Etna. *Nature*, **357**, 231-235.

Borgia, A. (1994) Dynamic basis of volcanic spreading. *Journal of Geophysical Research*, **99**, 17,791-17,804.

Borgia, A., van Wyk de Vries, B. (2003) The volcano-tectonic evolution of Concepción, Nicaragua. *Bulletin of Volcanology*, **65**, 248-266.

Borgia, A., Delaney, P. T., Denlinger, R. P. (2000) Spreading Volcanoes. *Annual Review of Earth And Planetary Sciences*, **28**, 539-570.

Branney, M. J. (1995) Downsag and extension at calderas: new perspectives on collapse geometries from ice-melt, mining, and volcanic subsidence. *Bulletin of Volcanology*, **57**, 303-318.

Branquet, Y., van Wyk de Vries, B. (2001) Effects of volcanic loading on regional compressive structures: new insights from natural examples and analogue modelling. *Comptes Rendus de l'Academie des Sciences*, Série IIA **333**, 455-461.

Cailleau, B., Walter, T., Janle, P. and Hauber, E. (2003) Modeling volcanic deformation in a regional stress field: Implications for the formation of graben structures on Alba Patera, Mars. *Journal of Geophysical Research*, **108**, 1,501-1,518.

Cameron, W. S. (1964) An interpretation of Schröter's Valley and other lunar sinuous rills. *Journal of Geophysical Research*, **69**, 2,423-2,430.

Carr, M. H., Greeley, R., Blasius, K. R., Guest, J. E., Murray, J.B. (1977) Some Martian volcanic features as viewed from the Viking orbiters. *Journal of Geophysical Research*, **82**, 3,985-4,015.

Carr, M. H. (1974) The geology of Mars. In: NASA Ames Research Center, *A Primer in Lunar Geology*, 459-460.

Carter, A., van Wyk de Vries, B., Kelfoun, K., Bechelèry, P., Briole, P. (2007) Pits, rifts and slumps: the summit structure of Piton de la Fournaise. *Bulletin of Volcanology*, **69**, 741-756.

Cecchi, E., van Wyk de Vries, B., Lavest, J-M. (2004) Flank spreading and collapse of weak-cored volcanoes. *Bulletin of Volcanology*, **67**, 72-91.

Chen, L. J., Bleacher, J. E., Lowman, P.D. (2008) The sinuosity of lunar rilles in the Aristarchus plateau. Lunar and Planetary Science Conference XXXIX abstract.

Chester, D. K., Duncan, A. M., Guest, J. E., Kilburn, C. (1985) Mount Etna: Anatomy of a Volcano. Chapman and Hall Ltd., London, pp. 300.

Cipa, A., Bébien, J., Bonin, B. (1996) Les terrasses et l'escarpement basal du volcan Martien Olympus Mons: Des témoins de vastes glissements gravitaires des flancs? *Comptes Rendus a l'Académie des Sciences*, Série II **322**, 369-376.

Comer, R. P., Solomon, S. C., Head, J. W. (1985) Mars: Thickness of the lithosphere from the tectonic response to volcanic loads. *Reviews of Geophysics*, **23**, 61-92.

Crown, D. A., Greeley, R. (1993) Volcanic geology of Hadriaca Patera and the eastern Hellas region of Mars. *Journal of Geophysical Research*, **98**, 3,431-3,451.

Crumpler, L. S., Aubele, J. C. (1978) Structural evolution of Arsia Mons, Pavonis Mons and Ascraeus Mons: Tharsis region of Mars. *Icarus*, **34**, 496-511.

Crumpler, L. S., Head, J. W., Aubele, J. C. (1996) Calderas on Mars: characteristics, structure and associated flank deformation. In: McGuire, W. J., Jones, A. P., Neuberg, J. (eds) 1996, *Volcano Instability on the Earth and Other Planets*, Geological Society Special Publication, **110**, 307-348.

de Pablo, M., López, I., Martín, F., Márquez, A. (2006) Volcanic evolution of Hecates Tholus, Mars: a multiple working hypothesis approach. European Planetary Science Congress 2006. Berlin, Germany, 18 - 22 September 2006., p.59, P0016.

Desportes, C., Rice, M., Lee, P. (2007) Periglacial polygon fields on Devon Island, High Arctic, as possible analogs for high-latitude polygonal terrain on Mars: implications for Phoenix. Lunar and Planetary Science Conference XXXVIII., Abstract 2341.

Donnadieu, F., Merle, O. (1998) Experiments on the identation process during cryptodome intrusions: New insights into Mount St. Helens deformation. *Geology*, **26**, 79-82.

Elliott, D. (1976) The energy balance and deformation mechanisms of thrust sheets. *Philosophical Transcripts of the Royal Society of London*, **283**, 289–312.

Engelder, T. (1993) Stress regimes in the lithosphere. Princeton University Press, Princeton, New Jersey, U.S.A. 475 pp.

Farr, T. G., Rosen, P. A., Caro, E., Crippen, R., Duren, R., Hensley, S., Kobrick, M., Paller, M., Rodriguez, E., Roth, L., Seal, D., Shaffer, S., Shimada, J., Umland, J., Werner, M., Oskin, M., Burbank, D., Alsdorf, D. (2007) The Shuttle Radar Topography Mission. *Review of Geophysics*, **45**, doi:10.1029/2005RG000183.

Fink, J., Griffiths, R. (1991) Laboratory Simulations of Lava Flows with Solid Crusts. Lunar and Planetary Science Conference XXII abstract.

Francis, P. W., Wadge, G. (1983) The Olympus Mons aureole - Formation by gravitational spreading. *Journal of Geophysical Research*, **88**, 8,333-8,344.

Geshi, N., Shimano, T., Chiba, T., Nakada, S. (2002) Caldera collapse during the 2000 eruption of Miyakejima Volcano, Japan. *Bulletin of Volcanology*, **64**, 55-68.

Girard, G., van Wyk de Vries, B. (2005) The Managua Graben and Las Sierras-Masaya volcanic complex (Nicaragua); pull-apart localization by an intrusive complex: results from analogue modelling. *Journal of Volcanology and Geothermal Research*, **144**, 37-57.

Gornitz, V. (1972) The origin of sinuous rilles. *The Moon*, **6**, 337-356.

Greeley, R., Carr, M., Guest, J., Blasius, K. (1977) Preliminary assessment of Martian volcanic features from Viking data. *Bulletin of the American Astronomical Society*, **9**, 440.

Greeley, R. (1971) Lunar Hadley Rille: Considerations of Its Origin. *Science*, **172**, 722-725.

Gregg, T., Williams, S. (1993) Explosive mafic volcanism on Earth and Mars. Lunar and Planetary Science Conference XXIV abstract.

Gunn, R. (1943) A quantitative study of isobaric equilibrium and gravity anomalies in the Hawaiian islands. *J. Franklin Institute*, **236**, 373-396.

Hall, L., Solomon, C., Head, J., Mouginis-Mark, P. (1983) Elysium Region, Mars: Characterization of tectonic features. Lunar And Planetary Science Conference XIV abstract.

Harris, S. A. (1977) The aureole of Olympus Mons, Mars. *Journal of Geophysical Research*, **82**, 3,099-3,107.

Harrison, K. P., Grimm, R. E. (2005) Groundwater-controlled valley networks and the decline of surface runoff on early Mars. *Journal of Geophysical Research*, **110**, doi:10.1029/2005JE002455.

Hauber, E., van Gasselt, S., Ivanov, B., Werner, S., Head, J. W., Neukum, G., Jaumann, R., Greeley, R., Mitchell, K. L., Muller, P. & The HRSC Co-Investigator Team. (2005) Discovery of a flank caldera and very young glacial activity at Hecates Tholus, Mars. *Nature*, **434**, 356-361.

Head, J. W. (1996) Volcano instability development: a planetary perspective. In: McGuire, W. J., Jones, A. P., Neuberg, J. (eds) 1996, *Volcano Instability on the Earth and Other Planets*, Geological Society Special Publication, **110**.

Head, J. W. (1976) Lunar volcanism in space and time. *Reviews of Geophysics and Space Physics*, **14**, 265-300.

Head, J. W., Solomon, S. C. (1981) Tectonic Evolution of the Terrestrial Planets. *Science*, **213**, 62-76.

Head, J. W., Wilson, L. (1991) Absence of large shield volcanoes and calderas on the moon - Consequence of magma transport phenomena? *Geophysical Research Letters*, **18**, 2,121-2,124.

Head, J. W., Murchie, S. L., Prockter, L. M., Solomon, S. C., Chapman, C. R., Strom, R. G., Watters, T. R., Blewett, D. T., Gillis-Davies, J. J., Fassett, C. I., Dickson, J. L., Morgan, G. A., Kerber, L. (2009) Volcanism on Mercury: Evidence from the first MESSENGER flyby for extrusive and explosive activity and the volcanic origin of plains. *Earth and Planetary Science Letters*, **285**, 227-242.

Helbert, J., Reiss, D., Hauber, E., Benkhoff, J. (2005) Limits on the burial depth of glacial ice deposits on the flanks of Hecates Tholus, Mars. *Geophysical Research Letters*, **32**, doi:10.1029/2005GL023712.

Hiesinger, H., Head, J. W. III, Neukum, G. (2007) Young lava flows on the eastern flank of Ascraeus Mons: Rheological properties derived from High Resolution Stereo Camera (HRSC) images and Mars Orbiter Laser Altimeter (MOLA) data. *Journal Of Geophysical Research*, **112**, doi:10.1029/2006JE002717.

Hodges, C., Moore, H. (1994) Atlas of Volcanic Landforms on Mars (U.S. Geological Survey Professional Paper, 1534). United States Government Printing Office, Washington, pp. 194.

Hodges, C. A., Moore, H. J. (1979) The subglacial birth of Olympus Mons and its aureoles. *Journal of Geophysical Research*, **84**, 8,061-8,074.

Holohan, E. P., Troll, V. R., Walter, T. R., Münn, S., McDonnell, S., Shipton, Z. K. (2005) Elliptical calderas in active tectonic settings: an experimental approach. *Journal of Volcanology and Geothermal Research*, **144**, 119-136.

Hubbert, M.K. (1951) Mechanical basis for certain familiar geologic structures. *Geological Society of America Bulletin*, **62**, 355- 372.

Hughes, S. S., Sakimoto, S. E. H., Gregg, T. K. (2008) A petrogenetic model of plains-style low shield volcanoes on Mars – implications for magma production in the Tharsis region. Lunar and Planetary Science Conference, Abstract 1619.

Hulme, G. (1973) Turbulent lava flow and the formation of lunar sinuous rilles. *Modern Geology*, **4**, 107-117.

Irwin, R. P. III, Howard, A. D., Craddock, R. A. (2006) Theater-headed valleys: the roles of overland flow and groundwater sapping. Lunar and Planetary Science Conference XXXVII, Abstract 1912.

Jaumann, R., Neukum, G., Behnke, T., Duxbury, T. C., Eichentopf, K., Flohrer, J., Gasselt, S. V., Giese, B., Gwinner, K., Hauber, E., Hoffmann, H., Hoffmeister, A., Köhler, U., Matz, K.-D., McCord, T. B., Mertens, V., Oberst, J., Pischel, R., Reiss, D., Ress, E., Roatsch, T., Saiger, P., Scholten, F., Schwarz, G., Stephan, K., Wählisch, M., the HRSC Co-Investigator Team. (2007) The high-resolution stereo camera (HRSC) experiment on Mars Express: Instrument aspects and experiment conduct from interplanetary cruise through the nominal mission. *Planetary and Space Science*, **55**, 928-952.

Kadish, S. J., Head, J. W., Parsons, R. L., Marchant, D. R. (2008) The Ascraeus Mons fan-shaped deposit: Volcano–ice interactions and the climatic implications of cold-based tropical mountain glaciation. *Icarus*, **197**, 84-109.

Kargel, J. S., Wessels, R., Begét, J. E., Eddy, T., Lloyd, S., Macaulay, D., Proch, M., Skinner, J., Tanaka, K. L. (2004) Alaskan permafrost analogs of Martian small valley networks, thermokarst, terrain softening, terraces, and volcanic craters. Lunar and Planetary Science Conference XXXV abstract.

King, J. S., Riehle, J. R. (1974) A proposed origin of the Olympus Mons escarpment. *Icarus*, **23**, 300-317.

Krall, E. R., van Dijk, M., Postmal, G., Kleinhaus, M. G. (2008) Martian stepped-delta formation by rapid water release. *Nature*, **451**, 973-976.

Laity, J. E., Malin, M. C. (1985) Sapping processes and the development of theater-headed valley networks in the Colorado Plateau. *Geological Society of America Bulletin*, **96**, 203-217.

Lambeck, K., Nakiboglu, S. M. (1980) Seamount loading and stress in the ocean lithosphere. Journal of Geophysical Research, 85, 6,403-6,418.

Leighton, R. B., Murray, B. C., Sharp, R. P., Allen, J. D., Sloan, R. K. (1965) Mariner IV photography of Mars: initial results. *Science*, **149**, 627-630.

Li, H., Robinson, M. S., Jurdy, D. M. (2005) Origin of Martian northern hemisphere mid-latitude lobate debris aprons. *Icarus*, **176**, 382-394.

Li, R., di, K., Hwangbo, J., Chen, Y. (2007) Rigorous Photogrammetric Processing of HiRISE Stereo Images for Topographic and Geomorphologic Analysis at MER landing sites. American Geophysical Union, Fall Meeting 2007, abstract #P31B-0432.

Lopes, R., Guest, J., Wilson, C. (1980) Origin of the Olympus Mons Aureole and Perimeter Scarp. *Moon and the Planets*, **22**, 221-234.

Lowry, A., Zhone, S. (2003) Surface versus internal loading of the Tharsis rise, Mars. *Journal of Geophysical Research*, **108**, doi:10.1029/2003JE002111.

Malin, M. C., Bell, J. F. III, Cantor, B. A., Caplinger, M. A., Calvin, W. M., Clancy, R. T., Edgett, K. S., Edwards, L., Haberle, R. M., James, P. B., Lee, S. W., Ravine, M. A., Thomas, P. C., Wolff, M. J. (2007) Context Camera investigation on board the Mars Reconnaissance Orbiter. *Journal Of Geophysical Research*, **112**, doi:10.1029/2006JE002808.

Marti, J., Ablay, G., Redshaw, L., Sparks, R. (1994) Experimental studies of collapse calderas. *Journal of Geophysical Research*, **151**, 919-929.

Masson, P. (1977) Structure pattern analysis of the Noctis Labyrinthus-Valles Marineris regions of Mars. *Icarus*, **30**, 49-62.

Masursky, H., Batson, R. M., McCauley, J. F., Soderblom, L. A., Wildey, R. L., Carr, M. H., Milton, D. J., Wilhelms, D. E., Smith, B. A., Kirby, T. B., Robinson, J. C., Leovy, C. B., Briggs, G. A., Duxbury, T. C., Acton, C. H., Jr., Murray, B. C., Cutts, J. A., Sharp, R. P., Smith, S., Leighton, R. B., Sagan, C., Veverka, J., Noland, M., Lederberg, J., Levinthal, E., Pollack, J. B., Moore, J. T.,

Jr., Hartmann, W. K., Shipley, E. N., de Vaucouleurs, G., Davies, M. E. (1972) Mariner 9 Television Reconnaissance of Mars and Its Satellites: Preliminary Results. *Science*, **175**, 294-305.

Masursky, H. (1974) An overview of geological results from Mariner 9. In: NASA Ames Research Center. *A Primer in Lunar Geology*, 467-488.

Mathieu, L., van Wyk de Vries, B. (2009) Edifice and substrata deformation induced by intrusive complexes and gravitational loading in the Mull volcano (Scotland). *Bulletin of Volcanology*, doi: 10.1007/s00445-009-0295-5.

McGovern, P., Morgan, J. (2005) Spreading of the Olympus Mons volcanic edifice, Mars. Lunar and Planetary Science Conference XXXVI abstract.

McGovern, P. J., Morgan, J. K. (2008) Volcanic Spreading at Olympus Mons: New Models, with Implications for Martian Volcanic Edifice Structures and the Distribution of Phyllosian Sediments. Lunar and Planetary Science Conference XXXVIX, Abstract 2304.

McGovern, P. J., Morgan, J. K. (2009) Volcanic spreading and lateral variations in the structure of Olympus Mons, Mars. Geology, 37, 139-142.

McGovern, P.J., Solomon, S.C. (1993) State of stress, faulting, and eruption characteristics of large volcanoes on Mars. *Journal of Geophysical Research*, **98**, 23,553-23,579.

McGovern, P., Solomon,C. (1997a) Some implications of a basal detachment structural model for Olympus Mons. Lunar and Planetary Science Conference XXVIII abstract.

McGovern, P. J., Solomon, S. C. (1997b) Filling of flexural moats around large volcanoes on Venus: Implications for volcano structure and global magmatic flux. Journal of Geophysical Research, 102, 16,303-16,318.

McGovern, P., Solomon, S., Head, J., Smith, D., Zuber, M., Neumann, G. (2001) Extension and uplift at Alba Patera: Insights from MOLA observations and loading models. *Journal of Geophysical Research*, **106**, 23,769-23,809.

McGovern, P., Solomon, S., Smith, D., Zuber, M., Simons, M., Wieczorek, M., Phillips, R., Neumann, G., Aharonson, O., Head, J. (2004) Correction to: Localized gravity/topography

admittance and correlation spectra on Mars: Implications for regional and global evolution. *Journal of Geophysical Research*, **109**, doi:10.1029/2004JE002286.

McGovern, P. J. (2007) Flexural stresses beneath Hawaii: Implications for the October 15, 2006, earthquakes and magma ascent. Geophysical Research Letters, 34, doi:10.1029/2007GL031305.

McKenzie, D., Ford, P. G., Liu, F. and Pettengill, G. H. (1992) Pancakelike domes on Venus. *Journal of Geophysical Research*, **97**, 15,967-15,976.

McSween, H. Y., Grove, T. L., Wyatt, M. B. (2003) Constraints on the composition and petrogenesis of the Martian crust. *Journal of Geophysical Research*, **108**, doi: 10.1029/2003JE002175.

Mege, D., Masson, P. (1996) Stress models for Tharsis formation, Mars. *Planetary and Space Science,* **44**, 1,471-1,497.

Melosh, H. J. (1978) The tectonics of mascon loading. Lunar and Planetary Science Conference IX abstract.

Merle, O., Borgia, A. (1996) Scaled experiments of volcanic spreading. *Journal of Geophysical Research*, **101**, 13,805-13,817.

Middleton, G. V., Wilcock, P. R. (1994) Mechanics in the Earth and Environmental Sciences. Cambridge University Press, London, pp. 459.

Montesi, L. (1999) Concentric Dike Swarm and Internal Structure of Pavonis Mons (Mars). Lunar and Planetary Science Conference XXX abstract.

Montési, L. (2000) Concentric dike swarms on the flanks of Pavonis Mons: Implications for the evolution of Martian shield volcanoes and mantle plumes. In: Ernst, R. E., Buchan, K. L. (eds) 2000, *Locating Pre-Mesozoic Mantle Plumes*, Geological Society Special Publication.

Morgan, J., McGovern, P. (2005) Discrete element simulations of gravitational volcanic deformation: 1. Deformation structures and geometries. *Journal of Geophysical Research*, **110**, doi10.1029/2004JB003252.

Morris, E. (1981) Structure of Olympus Mons and its Basal Scarp. In International Colloquium on Mars, 3d, Pasadena, Calif., 1981, Papers: Houston, Tex., Lunar and Planetary Science Contribution 441.

Morris, E. C. (1982) Aureole deposits of the Martian volcano Olympus Mons. *Journal of Geophysical Research*, **87**, 1,164-1,178.

Morris, E. C., Dwornik, S. E. (1978) U.S. Geological Survey Map 1-1049.

Morris, A., Mouginis-Mark, P, Baloga, S. (2003) Did Glaciers Exist Recently on the Tharsis Montes? American Geophysical Union, Fall Meeting, Abstract P32C-08.

Mouginis-Mark, P. (1981) Late-stage summit activity of martian shield volcanoes. In: Proceedings of the 12th Lunar and Planetary Science Conference. *Geochimica et Cosmochimica Acta* Supplement **16**, 1,431-1,447.

Mouginis-Mark, P. J., Zisk, S. H., Downs, G. S. (1982) Ancient and modern slopes in the Tharsis region of Mars. *Nature*, **297**, 546-550.

Mouginis-Mark, P., Wilson, L., Head, J., Brown, S., Hall, J., Sullivan, K. (1984) Elysium Plantitia, Mars: Regional Geology, Volcanology, and Evidence for Volcano-Ground Ice Interactions. *Earth, Moon, and Planets*, **30**, 149-173.

Mouginis-Mark, P. J., Christensen, P. R. (2005) *Journal of Geophysical Research*, **110**, doi:10.1029/2005JE002421.

Mouginis-Mark, P. J., Rowland, S. K. (2008) Lava flows at Arsia Mons, Mars: Insights from a graben imaged by HiRISE. *Icarus*, **198**, 27-36.

Murray, J. B., van Wyk de Vries, B., Marquez, A., Williams, D., Byrne, P. K., Muller, J.-P., Kim, J.-R. (2010) Late-stage water eruptions from Ascraeus Mons volcano, Mars: implications for its structure and history. *Earth and Planetary Science Letters*, **294**, 479–491.

Neukum, G., Jaumann, R., Hoffmann, H., Hauber, E., Head, J. W., Basilevsky, A. T., Ivanov, B. A., Werner, S. C., van Gasselt, S., Murray, J. B., McCord, T., and The HRSC Co-Investigator

Team. (2004) Recent and episodic volcanic and glacial activity on Mars revealed by the High Resolution Stereo Camera. *Nature*, **432**, 971-979.

Oberbeck, V. R., Morrison, R. H. (1974) Laboratory simulation of the herringbone pattern associated with Lunar secondary crater chains. *The Moon*, **9**, 415-455.

Oehler, J.-F., van Wyk de Vries, B., Labazuy, P. (2005) Landslides and spreading of oceanic hot-spot and arc shield volcanoes on Low Strength Layers (LSLs): an analogue modeling approach. *Journal of Volcanology and Geothermal Research*, **144**, 169-189.

Parsons, R. L., Head, J. W. III. (2005) Ascraeus Mons fan-shaped deposit, Mars: geological history and volcano-ice interactions of a cold-based glacier. Lunar and Planetary Science Conference XXXVI, Abstract 1139.

Peale, S. J., Schubert, G., Lingenfelter, R. E. (1968) Distribution of Sinuous Rilles and Water on the Moon. *Nature*, **220**, 1222-1225.

Plescia, J., Saunders, R. (1979) The chronology of the martian volcanoes. *Proc. Lunar Planet. Sci. Conf.* **10th**, 2,841-2,859.

Plescia, J. B. (2004) Morphometric properties of Martian volcanoes. *Journal of Geophysical Research*, **109**. E03003, doi:10.1029/2002JE002031.

Plescia, J. (2007) Volcanology of the Elysium Volcanoes. Lunar and Planetary Science Conference XXXVIII abstract.

Ramberg, H. (1981) Gravity, deformation and the Earth's crust, 2nd ed. Academic Press, London. 452 pp.

Roche, O., Druitt, T. H., Merle, O. (2000) Experimental study of caldera formation. *Journal of Geophysical Research*, **105**, 395-416.

Roche, O., van Wyk de Vries, B., Druitt, T. (2001) Sub-surface structures and collapse mechanisms of summit pit craters. *Journal of Volcanology and Geothermal Research*, **105**, 1-18.

Rymer, H., van Wyk de Vries, B., Stix, J., Williams-Jones, G. (1998) Pit crater structure and processes governing persistent activity at Masaya Volcano, Nicaragua. *Bulletin of Volcanology*, **59**, 345-355.

Saunders, R. S., Pettengill, G. H. (1991) Magellan – Mission summary. *Science*, **252**, 247-249.

Scott, D. H., Carr, M. H. (1978) Geologic map of Mars. Geological Survey Miscellaneous Geological Investigation Series, U.S. Map I-1083.

Scott, E. D., Wilson, L. (1999) Evidence for a sill emplacement event on the upper flanks of the Ascraeus Mons shield volcano, Mars. *Journal of Geophysical Research*, **104**, 27,079-27,089.

Scott, E., Wilson, L. (2000) Cyclical summit collapse events at Ascraeus Mons, Mars. *Journal of the Geological Society*, London, **157**, 1,101-1,106.

Smith, D., Zuber, M., Frey, H., Garvin, J., Head, J., Muhleman, D., Pettengill, G., Phillips, R., Solomon, S., Zwally, H., Banerdt, W., Duxbury, T., Golombek, M., Lemoine, F., Neumann, G., Rowlands, D., Aharonson, O., Ford, P., Ivanov, A., Johnson, C., McGovern, P., Abshire, J., Afzal, R., Sun, Xiaoli. (2001) Mars Orbiter Laser Altimeter: Experiment summary after the first year of global mapping of Mars. *Journal of Geophysical Research*, **106**, E10, 23,689-23,722.

Solomon, S. C., Head, J. W. (1982) Evolution of the Tharsis province, Mars: The importance of heterogeneous lithospheric thicknesses on volcanic construction. *Journal of Geophysical Research*, **87**, 9,755-9,774.

Spencer, J., Fanale, F. (1990) New models for the origin of valles marineris closed depressions. *Journal of Geophysical Research*, **95**, 14,301-14,343.

Squyres, S. W., Carr, M. H. (1986) Geomorphic evidence for the distribution of ground ice on Mars. *Science*, **231**, 249-252.

Tanaka, K. L., Golombek, M. P. (1989) Martian Tension Fractures and the Formation of Grabens and Collapse Features at Valles Marineris. Lunar and Planetary Science Conference, 19th, Houston, TX, Mar. 14-18, 1988, Proceedings (A89-36486 15-91). Cambridge/Houston, TX, Cambridge University Press/Lunar and Planetary Institute, 1989, p. 383-396.

Tanaka, K. (1981) Structure of Olympus Mons Aureoles and Perimeter Escarpment. In: International Colloquium on Mars, 3d, Pasadena, Calif., 1981, Papers: Houston, Tex., Lunar and Planetary Institute, 261-263.

Tanaka, K. (1985) Ice-lubricated gravity spreading of the Olympus Mons aureole deposits. *Icarus*, **62**, 191-206.

Thomas, P. J., Squyres, S. W., Carr, M. H. (1990) Flank tectonics of Martian volcanoes. *Journal of Geophysical Research*, **95**, 14,345-14,355.

Thurber, C. H., Gripp, A. E. (1988) Flexure and seismicity beneath the south flank of Kilaeuea volcano and tectonic implications. *Journal of Geophysical Research*, **93**, 4,271-4,278.

Thurber, C. H, Toksöz, M. N. (1978) Martian lithospheric thickness from elastic flexure theory. Geophysical Research Letters, 5, 977-980.

Troll, V. R., Walter, T. R, Schmincke, H.-U. (2002) Cyclic caldera collapse: Piston or piecemeal subsidence? Field and experimental evidence. *Geology*, **30**, 135.

Twiss, R. J., Moores, E. M. (1992) Structural Geology. W. H. Freeman & Co., New York, pp. 532.

van Bemmelen, R. W. (1949) The Geology of Indonesia. General Geology of Indonesia and Adjacent Archipelagos. 1A, Government Printing Office, The Hague.

van Wyk de Vries, B., Borgia, A. (1996) The role of basement in volcano deformation. In: McGuire, W. J., Jones, A. P., Neuberg, J. (eds) 1996, *Volcano Instability on the Earth and Other Planets*, Geological Society Special Publication, **110**, pp. 95-110.

van Wyk de Vries, B., Francis, P. (1997) Catastrophic collapse at stratovolcanoes induced by gradual volcano spreading. *Nature*, **387**, 387-390.

van Wyk de Vries, B., Matela, R. (1998) Styles of volcano-induced deformation: numerical models of substratum flexure, spreading and extrusion. *Journal of Volcanology and Geothermal Research*, **81**, 1-18.

Walcott, R. (1970) Flexure of the lithosphere at Hawaii. *Tectonophysics*, **9**, 435-446.

Walcott, R. (1972) Late Quaternary Vertical Movements in Eastern North America: Quantitative Evidence of Glacio-Isostatic Rebound. *Reviews of Geophysics*, **10**, 849-884.

Walker, G. P. (1992) "Coherent intrusion complexes" in large basaltic volcanoes — a new structural model. *Journal of Volcanology and Geothermal Research*, **50**, 41-54.

Walsh, J. J., Watterson, J. (1991) Geometric and kinematic coherence and scale effects in normal fault systems. *Geological Society of London Special Publication*, **56**, 193-203.

Walter, T., Troll, V. (2001) Formation of caldera periphery faults: an experimental study. *Bulletin of Volcanology*, **63**, 191-203.

Watters, T. R. (2003) Lithospheric flexure and the origin of the dichotomy boundary on Mars. *Geology*, **31**, 271.

Watts, A. B. (2001) Isostasy and Flexure of the Lithosphere. Cambridge University Press, Cambridge. 458 pp.

Williams, K. K., Zuber, M. T. (1995) An experimental study of incremental surface loading of an elastic plate: Application to volcano tectonics. *Geophysical Research Letters*, **22**, 1,981-1,984.

Williams, D. A., Greeley, R., Fergason, R., Kuzmin, R., McCord, T. B., Combe, J.-P., Head, J. W., Xiao, L., Manfredi, L., Poulet, F., Pinet, P., Baratoux, D., Plaut, J. J., Raitala, J., Neukum, G., the HRSC Co-Investigator Team. (2009) The Circum-Hellas Volcanic Province, Mars: Overview. *Planetary and Space Science*, **57**, 895-916.

Williams, D. A., Greeley, R., Zuschneid, W., Werner, S. C., Neukum, G., Crown, D. A., Gregg, T. K. P., Gwinner, K., Raitala, J. (2007) Hadriaca Patera: Insights into volcanic history from Mars Express High Resolution Stereo Camera. *Journal of Geophysical Research*, **112**, doi:10.1029/2007/JE002924.

Wilson, L., Head, J. (1994) Mars: Review and analysis of volcanic eruptions theory and relationships to observed landforms. *Review of Geophysics*, **32**, 221-263.

Wilson, L., Scott, E., Head, J. (2001) Evidence for episodicity in the magma supply to the large Tharsis volcanoes. *Journal of Geophysical Research,* **106**, 1,423–1,433.

Wilson, L., Head, J. (2002) Tharsis-radial graben systems as the surface manifestation of plume-related dike intrusion complexes: Models and implications. *Journal of Geophysical Research*, **107**, doi: 10.1029/2001JE001593.

Wu, S. S., Garcia, P. A., Jordan, R., Schafer, F. J., Skiff, B. A. (1984) Topography of the shield volcano, Olympus Mons on Mars. *Nature*, **309**, 432-435.

Wyrick, D., Ferrill, D. A., Morris, A.P., Colton, S. L, Sims, D. W. (2004) Distribution, morphology, and origins of Martian pit crater chains. *Journal of Geophysical Research*, **109**, doi:10.1029/2004JE002240.

Zimbelman, J. R. (1985) Estimates of rheological properties for flows on the Martian volcano Ascraeus Mons. *Journal of Geophysical Research*, 90, Supplement D157-162.

Zimbleman, J., Edgett., K. (1992) The Tharsis Montes, Mars: Comparison of Volcanic and Modified Landforms. *Proc. Lunar Planet. Sci.*, **22**, 31-44.

Zuber, M. T., Mouginis-Mark, P. J. (1992) Caldera subsidence and magma chamber depth of the Olympus Mons volcano, Mars. *Journal of Geophysical Research*, **97**, 18,295-18,307.

Zuber, M. T., Bills, B. G., Frey, H. V., Kiefer, W. S., Nerem, R. S., Roark, J. H. (1993) Possible flexural signatures around Olympus and Ascraeus Montes, Mars. 24th Lunar and Planetary Science Conference, Abstract 1591.

Zuber, M., Solomon, S., Phillips, R., Smith, D., Tyler, G., Aharonson, O., Balmino, G., Banerdt, W., Head, J., Johnson, C., Lemoine, F., McGovern, P., Neumann, G., Rowlands, D., Zhong, S. (2000) Internal Structure and Early Thermal Evolution of Mars from Mars Global Surveyor Topography and Gravity. *Science*, **287**, 1,788-1,793.

That's it man, game over man, game over!

Pfc. W. Hudson, USMC